Efficient and Reliable Wide-Area Protection and Control Schemes for Electric Power Systems Based on Time-Synchronized Phasor Measurements

A Dissertation

Presented in Partial Fulfillment of the Requirements for the

Degree of Doctorate of Philosophy

with a

Major in Electrical Engineering

In the

College of Graduate Studies

University of Idaho

by

Armando Guzman

Major Professor: Brian K. Johnson, Ph.D.

Committee Members: Joseph D. Law, Ph.D., Herbert L. Hess, Ph.D., Virgilio A. Centeno, Ph.D.

Department Administrator: Mohsen Guizani, Ph.D.

November 2015

Authorization to Submit Dissertation

This dissertation of Armando Guzman, submitted for the degree of Doctor of Philosophy with a Major in Electrical Engineering and titled "Efficient and Reliable Wide-Area Protection and Control Schemes for Electric Power Systems Based on Time-Synchronized Phasor Measurements," has been reviewed in final form. Permission, as indicated by the signatures and dates below, is now granted to submit final copies to the College of Graduate Studies for approval.

Major Professor: _____ Date: _____
                   Brian K. Johnson, Ph.D., P.E.

Committee Members: _____ Date: _____
                   Joseph D. Law, Ph.D., P.E.

                   _____ Date: _____
                   Herbert L. Hess, Ph.D., P.E.

                   _____ Date: _____
                   Virgilio A. Centeno, Ph.D.

Department
Administrator: _____ Date: _____
                   Mohsen Guizani, Ph.D.

Abstract

Voltage and current time-synchronized measurements, better known as synchrophasors, use an absolute time reference and can provide information of the state of the power system in real time. So far, typical synchrophasor applications have been limited to visualization and post-mortem analysis. This dissertation proposes four efficient and reliable synchrophasor-based protection and control applications for detecting ground faults in power lines and preventing power system disruptions. The work begins by recommending the quadrature demodulation method for estimating synchrophasors suitable for detecting power oscillations.

The first proposed application is a system integrity protection scheme (SIPS) for automatic generation shedding based on estimation of the voltage angle difference between two areas of the power system. The proposed scheme combines phasor measurements, phasor data concentration, and control functionality in a single device to minimize components within a system and increase its reliability.

The second application is a synchrophasor-based line differential protection scheme that complements primary distance protection schemes, provides backup protection, and does not require voltage information. A negative-sequence current differential element, together with total current faulted phase identification, detects high-resistance faults without compromising phase selectivity. An additional important benefit of this proposed approach is that communication-channel delay asymmetry does not affect differential element operation resulting from use of time-stamped measurements.

The third application proposes a power system dynamics monitor that includes out-of-step detection, power swing detection, and predictive out-of-step tripping algorithms. These synchrophasor-based algorithms allow the implementation of a SIPS that requires minimum network topology information and automatically adapts to changing operating conditions of the power system.

The fourth application proposes a SIPS that performs modal analysis in real time, identifies inter-area power oscillations within the frequency band of interest, and takes remedial action if the signal amplitude exceeds a predefined threshold and the damping ratio is less than a predefined threshold

for a predefined time. The proposed SIPS has proven effective in a field application and has prevented power system collapse on multiple occasions when inter-area power oscillations occurred.

Throughout all four SIPSs this work proposes components have been kept to a minimum. This reduction in complexity makes these schemes more reliable.

Acknowledgements

I want to express my sincere gratitude to Professor Brian K. Johnson for his encouragement that motivated me to continue my education in electrical and computer engineering and for the help that he gave me in finishing my advanced studies in electrical engineering.

My recognition and appreciation to all the people who co-wrote with me the papers to which this dissertation refers. My thankfulness for the help I received on the development and deployment of this synchrophasor-based protection and control technology.

Dedication

My genuine appreciation to Claudia my wife, Elizabeth Andrea my daughter, and Armando Daniel my son for their patience while I worked on my classes, homework, exams, research, and writing. I also appreciate their encouragement and help that allowed me to obtain my advanced degree.

Table of Contents

xii

List of Tables

xiii

List of Figures

1.1 Roadmap for deploying synchrophasor application. 2

1.2 BPA's multi-task wide-area voltage stability and voltage control system (WACS). 4

2.1 Phasor representation with a 1 PPS UTC reference. 12

2.2 Voltages at different network locations. 13

2.3 Voltages at different network locations with a common reference. 14

2.4 The phase delay, β, increases according to the frequency deviation, Δf. 16

2.5 Phase measurement at off-nominal frequency for $\Delta f > 0$; $\beta (t) = 2\pi \cdot \Delta f \cdot t + \phi$. The phase delay, β, increases according to the frequency deviation, Δf. 16

2.6 Off-nominal frequency phase measurements obtained at two locations. The angle difference between the two measurements, $\Delta \beta$, remains constant. 17

2.7 Sampling at fixed time intervals with an absolute time reference for synchronized phasor measurement, oscillography, and harmonic analysis. 18

2.8 Phasor estimation at 30, 45, 60, 75, and 90 Hz. 19

2.9 Quadrature demodulation signal processing for synchrophasor estimation. 21

2.10 Total filtering magnitude frequency response when using the DFT method with an observation window of 16 taps and a sampling frequency of 960 Hz. 22

2.11 Total filtering magnitude response when using the quadrature demodulation method with a fourth order Chebysheb Type II filter, a 10 tap Kaiser window, and a sampling frequency of 1 kHz.   23

2.12 Total filtering magnitude frequency response when using the quadrature demodulation method for 60 and 30 messages per second. 24

2.13 Step responses of the quadrature demodulation filtering process for 30 and 60 messages per second.   25

2.14 Time alignment is performed in the phasor data concentrator. 26

3.1 Fink and Carlsen diagram showing all possible power system operating states with normal/emergency state transitions added. 29

3.2 Voltage at an EHV node while the power system operates in the extreme state. This event shows how a voltage instability problem evolves into a rotor angle instability problem for lack of proper action to return the system to the normal or alert state. 31

Abbreviations

ADC	Analog-to-digital converter
ADOR	Angle difference operating region
ADOP	Angle difference operating point
AGC	Automatic generation control
AGGS	Automatic generator-shedding scheme
BPLP	Backup power line protection
BPA	Bonneville Power Administration
CCF	Cross-country fault
CFE	Comisión Federal de Electricidad
CODESYS	Controller development system
DFT	Discrete Fourier transform
EHV	Extra-high voltage
FPI	Faulted phase identification
GLONASS	Global navigation satellite system
GNSS	Global navigation satellite system
GOES	Geostationary operational environmental satellites
GPS	Global positioning system
IEEE	Institute of electrical and electronic engineers
IRIG	Inter-range instrumentation group
LORAN	Long range navigation
LPF	Low-pass filter
LPM	Linear predictor model
MA	Modal analysis
MICL	Mode identification and control logic
OOS	Out of step
OOSD	Out-of-step detection
OOST	Out-of-step tripping
PDC	Phasor data concentrator
PLC	Programmable logic controller
PMA	Prony method for modal analysis
PMCU	Phasor measurement and control unit
PMU	Phasor measurement unit
POTT	Permissive overreaching transfer trip
PPS	Pulse per second
PSD	Power swing detector
RTDS	Real-time digital simulator
RTOS	Real-time operating system
RTS	Runtime system
SIPS	System integrity protection scheme
SNR	Signal-to-noise ratio
SPU	Synchrophasor processing unit
SPT	Single pole tripping
SVC	Static VAR compensation
TCP	Transmission control protocol

TCSC	Thyristor controlled series compensation
UDP	User datagram protocol
UTC	Coordinated universal time
VAR	Volt-ampere reactive
WACS	Wide-area voltage stability and voltage control system
WAN	Wide-area network
WAPS	Wide-area protection scheme

Chapter 1 Introduction

1.1 Overview

The advent of satellite-based time-keeping systems, increased availability of communications networks, and advances in computer technology have made possible efficient and reliable wide-area time-synchronized measurement-based schemes for electrical power system real-time protection and control that many researchers envisioned but found difficult to implement [1, 2, 3, 4, 5, 6, 7, 8]. Key technologies that have helped to develop these applications include the following:

- Time clocks that provide absolute time accurate to 500 ns at every power substation.
- Time-synchronized phasor measurement units (PMUs) that transmit phasors at 30 messages per second (msg/s) or faster in real time.
- Phasor measurement and control units (PMCU) that sample synchronously across the power system within 1 μs and include PMU and control capabilities.
- Communication networks that can reliably exchange large amounts of data at 100 Mbps or faster.
- Generic computing platforms that can process time-synchronized messages within 4 ms or faster.

Traditional PMUs provide time-synchronized voltage and current measurements and do not execute control actions. Present protective relays can provide time-synchronized phasor measurements and execute control actions that eliminate the need for different devices providing time-synchronized measurements and control in wide-area protection and control applications. The applications this document proposes use devices that combine the aforementioned functionality with signal processing adequate for the corresponding application. The addition of time-synchronized measurement capability in a protective relay results in increased reliability of wide-area protection and control schemes.

The previous technological advances have led to synchrophasor applications progressing from simple visualization, data archiving, and postmortem analysis tools to real-time protection and control systems. These new systems can produce, consume, time align, and process synchrophasor data. A significant improvement has been that synchrophasor processing results translate into alarm, trip, or

control actions issued in real time. With this technology, formerly complex synchrophasor applications such as system integrity protection schemes (SIPSs) and assessment of power system stability over large geographical areas are easier to implement, have fewer components, and are more reliable than traditional solutions.

This document proposes the following applications that benefit from time-synchronized measurements and advances in synchrophasor technology:

- Automatic generator shedding.
- Power line differential protection.
- Out-of-step (OOS) and power swing detection.
- Inter-area power oscillation detection.

The rest of this chapter provides information about the motivation for this work, a literature review of relevant publications, the main contributions of this work, and a summary of remaining chapters.

1.2   Motivation

Technical publications related to synchrophasor technology suggest that synchrophasor-based real-time control, adaptive protection, and wide-area stabilization applications are years from actual implementation in power systems. Figure 1.1 shows a roadmap, proposed by Novosel et al. [9], for deploying synchrophasor technology and applications for addressing specific power system problems.
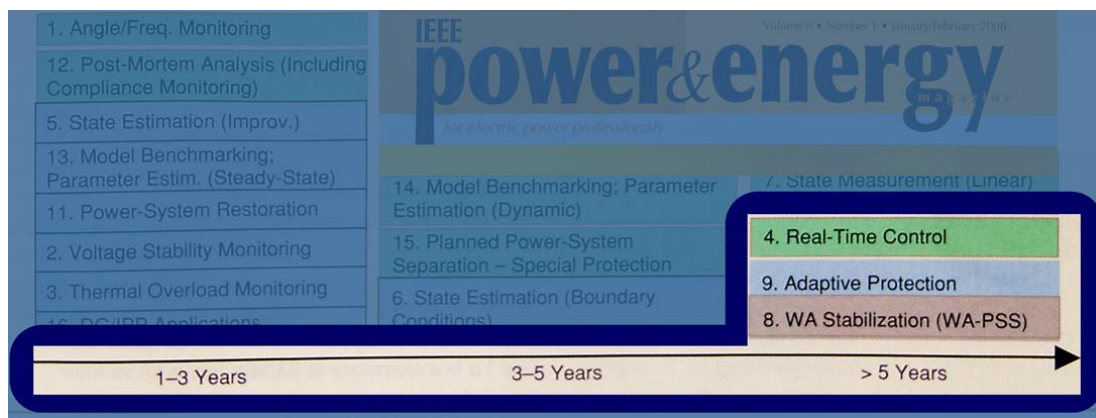
Figure 1.1   Roadmap for deploying synchrophasor applications.

The Bonneville Power Administration (BPA) has done pioneering work on a wide-area voltage stability and voltage control system (WACS) for implementing generator tripping and reactive power compensation switching for transient stability control and voltage support as a demonstration project [10]; Taylor et al. mention in this paper that moving applications from measurement to control is a challenge for the 21st century. BPA's original WACS included PMUs, a phasor data concentrator (PDC), and a fault-tolerant control computer running several tasks (see Figure 1.2). Taylor et al. proposed two methods: the first only uses voltage magnitude measurements, and the second uses voltage magnitude and reactive power measurements.

The algorithm of the voltage magnitude method uses 12 time-synchronized voltage measurements from BPA's 500 kV network. The algorithm sends capacitor/reactor bank switching or generator tripping commands when the volt-second accumulated value of the weighted voltage average reaches a setpoint and the weighted voltage average is less than a predefined threshold. The scheme was intended to maintain system stability by taking control actions within one second.

The algorithm of the voltage magnitude and reactive power method uses the same weighted voltage magnitude average — as in the previous method — and the reactive power measurements from 15 transmission lines connected to six large generation power plants. The algorithm computes the weighted reactive power averages from these 15 time-synchronized measurements. Then, the algorithm uses fuzzy logic to combine the weighted voltage magnitude average and the weighted reactive power average. The output of this logic controls capacitor/reactor switching or issues generator tripping commands.
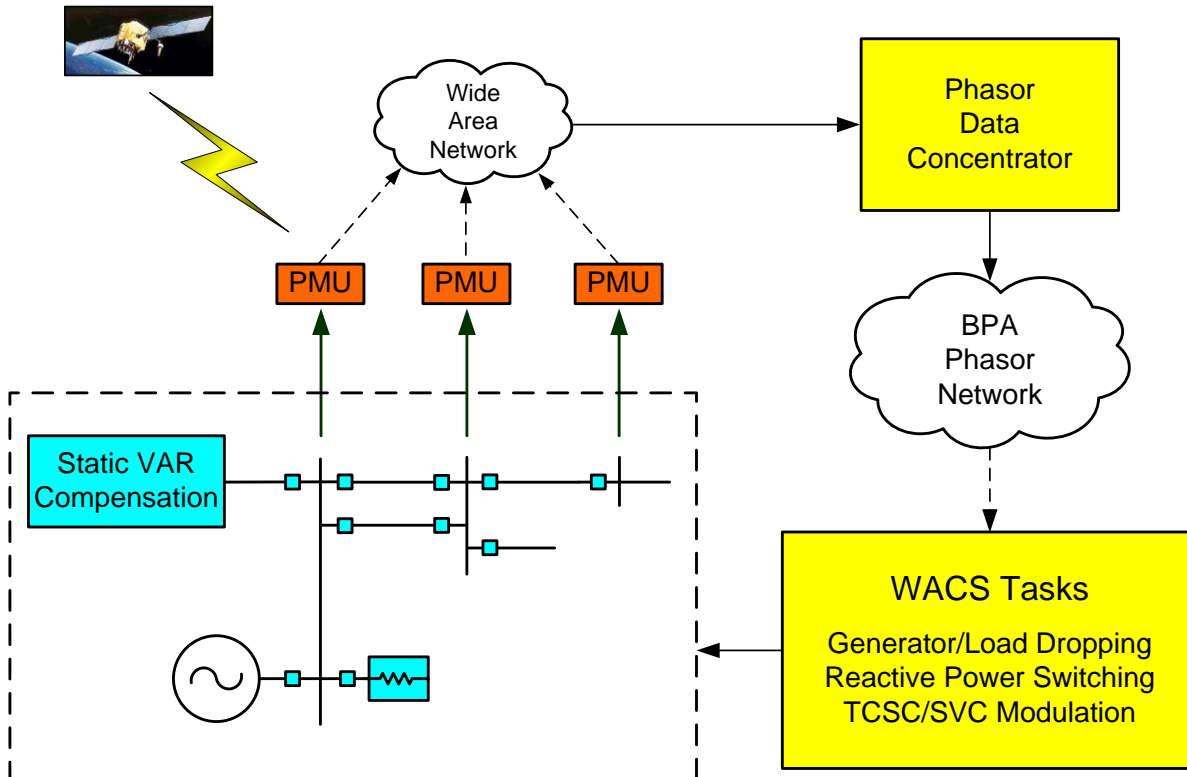
Figure 1.2   BPA's multi-task wide-area voltage stability and voltage control system (WACS).

In another SIPS application that does not use time-synchronized measurements, Comisión Federal de Electricidad (CFE) implemented a two-contingency remedial action scheme to prevent voltage collapse [11]. The scheme is highly dependent on the monitoring of the open/close statuses of three transmission links, complicating the scheme and negatively affecting its reliability — *Chapter 3* provides more details of this scheme. *Chapter 3* also explains how synchrophasors simplify this scheme.

Hauer et al. [12] presented initial results from using Prony analysis in the determination of frequency, damping, strength, and relative phase of the modal components of power system response signals. Analyses were performed on signals obtained from transient stability simulations and large-scale power system tests.

Trudnowski et al. [13] proposed a mode meter for near real-time security assessment implemented in the Real Time Dynamic Monitoring System [14] to alert power system operators to undesired damping of a particular mode. In this application, the monitoring displays update in near real time every 2 to 3 seconds. *Chapter 6* discusses a SIPS that estimates amplitude and damping of an

inter-area mode in real time through use of Prony analysis and takes control actions to maintain power system stability.

The previous challenges and status of synchrophasor technology motivated the author to pursue solutions for wide-area protection and control with improved efficiency and reliability that take actions to control and protect the system within hundreds of milliseconds.

1.3   Literature Review

The solutions presented in this work focus on the estimation and implementation of synchrophasors and the application of synchrophasors in wide-area protection and control. Following is a review of some of the most relevant publications on these topics in the last 35 years.

1.3.1   Synchrophasor Estimation and Angle Difference Measurements

Hydro-Québec Institute of Research pioneered the concept of wide-area voltage angle measurements using time-synchronized clocks with the LORAN C system. The proposed angle measurement technique, which achieved a precision of $\pm 1^\circ$, was based on measurement of the zero-crossings of the voltage signal with respect to the leading edge of the 1 PPS signal with an absolute time reference [1]. This system was later updated to receive a time-synchronization signal from a GOES satellite signal, improving the angle measurement error of the system to $\pm 0.5^\circ$ [2].

Bonanomi proposed a technique that samples voltage angles across an AC network simultaneously [3]. This technique also estimates the voltage angle by using the zero-crossings of the voltage signal. The proposed system uses accurate time sources synchronized to a radio time signal for controlling the acquisition of voltage signal samples.

Thorp et al. [5] presented the concept of real-time positive-sequence voltage measurements using time-synchronized sampling clocks at different locations for estimating the state of the power system. This approach uses the discrete Fourier transform (DFT) to estimate the fundamental frequency phasor. This seminal work has been the basis of many synchrophasor applications.

As part of Electricité de France's defense plan against loss of synchronism, involving system islanding to prevent disturbance propagation, Denys et al. [15] worked on the research and development of a

time-synchronized phase meter. This meter estimated the phasor by using quadrature demodulation, a fixed filter to remove harmonics, and an adaptive filter to remove the double frequency component.

1.3.2 Generator Shedding and Out-of-Step Detection and Prediction

Ohura et al. [16] proposed a generator-tripping algorithm to maintain power system stability based on an energy function method. The algorithm compares kinetic energy changes of generators to a predefined threshold; when the energy exceeds this threshold, the scheme trips selected generators. The system was installed in the Tokyo Electric Company network from June 1983 to May 1984 to demonstrate its suitability for commercial applications.

Schweitzer et al. described a power swing relay that determines the recoverability of the swing in its early stages [17]. To make this determination, the relay uses the acceleration in the power angle which is function of the second derivative of the angle difference in a two machine model. Reference [17] introduces the concept of a plane that compares the first and second derivatives of the angle difference against a line to determine if the swing is stable. This relay measures local voltages and currents and estimates the voltage at the remote source location by using the impedances between the two sources. This approach makes the algorithm to estimate the remote voltage dependent on the system topology and limits its application.

Thorp et al. [5] proposed an approach to detect and predict power system instability in real time by using the equal-area criterion and assuming that the machine rotor angles and speeds can be measured. The proposed two machine system approach can be applied to two groups of coherent generators.

Ohura et al. [18] described the development of a predictive out-of-step protection system based on angle difference measurements between substations; the system uses microwave-based communications for sampling synchronization. The algorithm predicts the future phase difference and separates the power system based on power supply and demand to prevent total system collapse. The system has been in service in the Tokyo Electric Company network since February, 1989.

Centeno et al. [19, 20] described the concept and field experiences of an adaptive OOS protection system that was installed in the Florida Power – Georgia Power 500 kV transmission corridor that connects the Florida peninsula to the eastern interconnected power system from October 1993 to January 1995. Two OOS relays were part of the system that uses remote time-synchronized measurements as transducers. In this system, the relays require power system impedances and machine inertia constants of a two-area system equivalent to compute power system dynamics based on its actual state through use of the equal area criterion. The OOS relay algorithm uses phasor information to compute the rotor angles of the equivalent system and calculates the angle difference between the two equivalent systems. Then, the relays use the angle difference and breaker information to determine the swing condition. The relays output a blocking signal for stable swings, a tripping signal for unstable swings, or a blocking signal upon successful reclosing. Field results proved the feasibility of using equal area concepts for OOS protection in power systems that behave as a two machine system.

1.3.3   Detection of Inter-Area Oscillation Using Modal Analysis

The IEEE Task Force Report on Identification of Electromechanical Modes in Power Systems [21] describes the mathematical background for identifying inter-area electromechanical oscillations through use of modal analysis. The report mentions that large power transfer across large geographical areas decreases the damping of inter-area modes and may cause inter-area oscillations. The presence of inter-area oscillations reduces the transmission network transfer capacity and has undesirable operational and economic consequences.

A system identification method that processes time domain measurements and performs Prony analysis for obtaining power system modal information was pioneered by Hauer [12]. The modal analysis-based SIPS proposed in this dissertation demonstrates the practicality of this approach.

1.4   Contributions

This work focuses on the conception and implementation of efficient and reliable synchrophasor-based wide-area protection and control systems. The work analyzes the performance of these comprehensive schemes by using computer simulations and field data from actual applications of the schemes in different power systems.

One objective of this work is to point out that the DFT method for estimating synchrophasors, described in *Chapter 2*, is not suitable for SIPSs that detect inter-area oscillations. This application requires filtering with a flat passband gain within a predetermined frequency range and heavy attenuation outside this frequency range. The quadrature demodulation method presented in *Chapter 2* and in the paper *Protective relay synchrophasor measurements under fault conditions* [22] uses a filtering process that meets these frequency response requirements. Estimation of synchrophasors through use of the quadrature demodulation method, with adequate digital filtering for applications such as detection of inter-area oscillations, has become the preferred method and is used as the basic synchrophasor estimation method included in the IEEE Std C37.118.1 [23]. The synchrophasor estimation method, proposed in *Chapter 2*, provides the flexibility to tailor the signal filtering requirements according to the application and communication bandwidth. *Chapter 2* provides details of this synchrophasor estimation method.

One of the main challenges of synchrophasor-based protection schemes is their lack of reliability resulting from their traditional use of multiple components. The automatic generation-shedding scheme (AGSS) presented in *Chapter 3* and in the paper *Using synchronized phasor angle difference for wide-area protection and control* [24] uses an angle difference algorithm implemented in a device that includes synchrophasor measurements, synchrophasor time alignment, deterministic real-time processing, and real-time control capabilities. This angle difference-based SIPS has been implemented with minimum system components, making it efficient and reliable.

Chapter 4 introduces synchrophasor-based power line protection for ground faults that uses local and remote negative- and zero-sequence currents with the following benefits:

- Uses only local and remote currents in its protection element characteristics.
- Provides backup line protection during loss-of-potential conditions.
- Detects high-resistance faults without compromising faulted phase selectivity.
- Is immune to communication-channel delay asymmetry.

US Patent 8655608 [25] and the paper *Backup transmission line protection for ground faults and power swing detection using synchrophasors* [26] also provide information about this synchrophasor-based protection application.

BPA's SIPS, described previously in this chapter, can be simplified by using PMUs with control capabilities and the synchrophasor processing unit (SPU) introduced in *Chapter 5* and proposed in the paper *Advanced real-time synchrophasor applications* [27]. The SPU performs PDC and WACS tasks by using a hard real-time operating system with deterministic processing interval and allows for the implementation of elaborated schemes such as the detection of power system oscillations.

Chapter 5 presents a scheme that uses synchrophasor angle difference calculations to reliably detect and predict out-of-step conditions in a two-area power system. The SIPS requires minimum network topology information and automatically adapts to changes in power system operating conditions. US Patent 7930117 [28] and the paper *Synchrophasor processor detects out-of-step conditions* [29] also describe the proposed approach. The two-area power swing detection scheme has become a fundamental building block for implementing reliable islanding detection schemes.

The SPU also has the ability to perform modal analysis in real time and issue remedial action commands. *Chapter 6* describes a SIPS that identifies inter-area oscillations and separates the transmission network to maintain its stability. US Patent 7987059 [30] provides information on this real-time modal analysis method and the paper *Wide-area protection and control scheme mantains Central America's power system stability* [31] provides an example of the implementation of this scheme; this scheme has detected multiple inter-area oscillations in the field and has prevented power system collapse in multiple occasions.

1.5   Summary of Efficient and Reliable Wide-Area Protection and Control Synchrophasor Applications

This dissertation presents the following wide-area protection and control applications for improving power system reliability through the use of synchrophasor technology:

- *Chapter 2* defines synchrophasors and describes such basic synchrophasor concepts as phasor angle reference for wide-area applications and phasor angle measurements at off-nominal frequencies. The chapter also describes two of the most popular phasor estimation methods and recommends the method best suited for detecting power system oscillations.

- *Chapter 3* describes an automatic generation-shedding scheme (AGSS) based on the voltage angle difference between two buses that identifies power system operating conditions that jeopardize the stability of the system and overload the subtransmission network. The AGSS sheds generation to balance generation and load, preventing voltage instability and network overload problems.

- *Chapter 4* describes a backup power line protection scheme that uses current differential protection concepts and takes advantage of time synchronization for eliminating channel delay asymmetry problems. The current differential element uses negative- and zero-sequence currents to detect high-resistance faults.

- *Chapter 5* describes an out-of-step detection scheme for preventing system collapse by detecting power oscillations in their early stages. This scheme uses the first and second derivatives of the voltage angle difference between power system locations to predict unstable oscillation operating conditions and takes remedial actions to prevent power system collapse.

- *Chapter 6* describes a SIPS based on modal analysis that detects inter-area oscillations in real time and splits the transmission network into two networks to maintain system stability. This SIPS allows increased power transfer limits, resulting in more efficient use of power generation resources.

- *Chapter 7* provides conclusions on the recommendations and applications this work presents and provides an update on the latest developments regarding use of the proposed applications. Chapter 7 also describes some of the challenges synchrophasor technology must overcome for wide-area protection and control applications and power system fault protection.

Chapter 2 Synchrophasor Principles and Technology for Wide-Area Protection and Control Applications

2.1 Time-Synchronized Phasor Measurement Principles

Voltage and current time-synchronized phasor measurements provide information about dynamic performance of a power system. The phasor definition assumes that the power system is in steady state. Understanding phasor estimation and adequate interpretation of time-synchronized measurements during transients are key factors for implementing wide-area protection and control schemes in power systems.

2.1.1 Definition of Synchrophasors

The definition of a time-synchronized phasor, or synchrophasor, provided in the IEEE Std C37.118.1-2011 [23] corresponds to the conventional definition of a phasor [32, 33] where the instantaneous phase angle ϕ of the synchrophasor is measured with respect to a cosine function at nominal system frequency that is synchronized to Coordinated Universal Time (UTC).

According to the previous definition, ϕ is the offset from a UTC synchronized reference cosine function. Figure 2.1 illustrates the phase angle of a sinusoidal signal with respect to the 1 Pulse Per Second (PPS) time reference, using a UTC reference, that is decoded from the IRIG-B [34] signal of a local satellite clock.
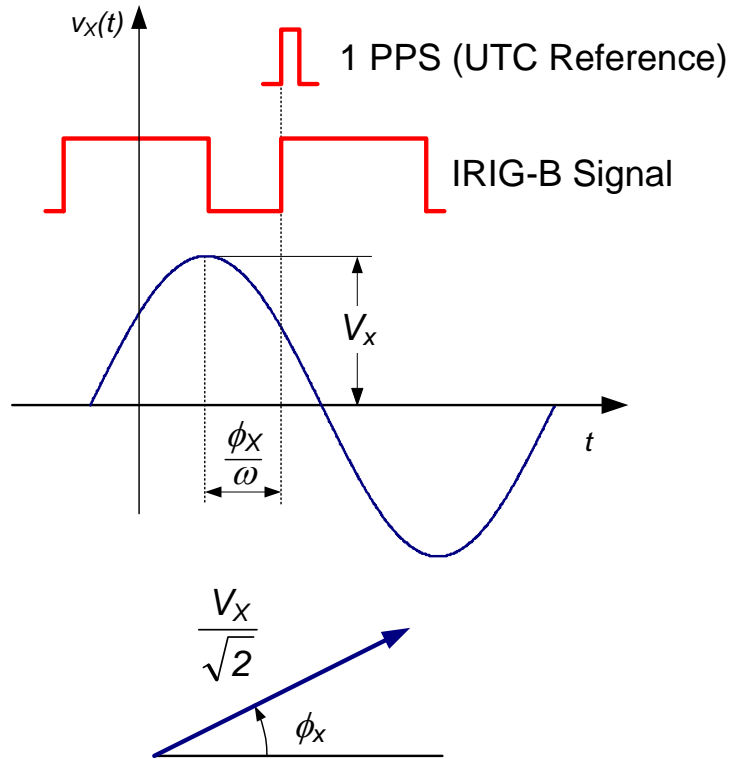
Figure 2.1   Phasor representation with a 1 PPS UTC reference.

The instantaneous phase angle measurement remains constant at rated frequency during use of the start of the second phase reference (1 PPS). If the signal is at an off-nominal frequency, the instantaneous phase varies with time. The choice of the nominal frequency signal as reference has an impact on phasor phase angle measurements at off-nominal frequencies.

2.1.2 Phasor Angle Reference for Wide-Area Power System Applications

The relative phase angles among voltage signals measured at different locations of the power system provide meaningful information for power system analysis and wide-area protection applications. These angles can be obtained by using time-synchronized voltage measurements. For example, a sinusoidal voltage wave can be represented as in (2.1).

$$v_x(t) = V_x \cdot \cos(2\pi \cdot f \cdot t + \phi_x) = V_x \cdot \cos(\omega \cdot t + \phi_x) \tag{2.1}$$

where:

V_x is the signal amplitude in volts,

ϕ_x is the phase angle in radians,

f is the frequency in Hz,

ω is the angular frequency in radians per second,

t is the time in seconds.

Figure 2.2 shows two voltage signals measured at different network locations (Terminals *A* and *B*). A simple way to obtain the relative phase angle of two signals acquired at two different power system locations is to measure the phase angle of the signals with respect to a common time-synchronized reference. This common reference can be a cosine wave at nominal system frequency [23].
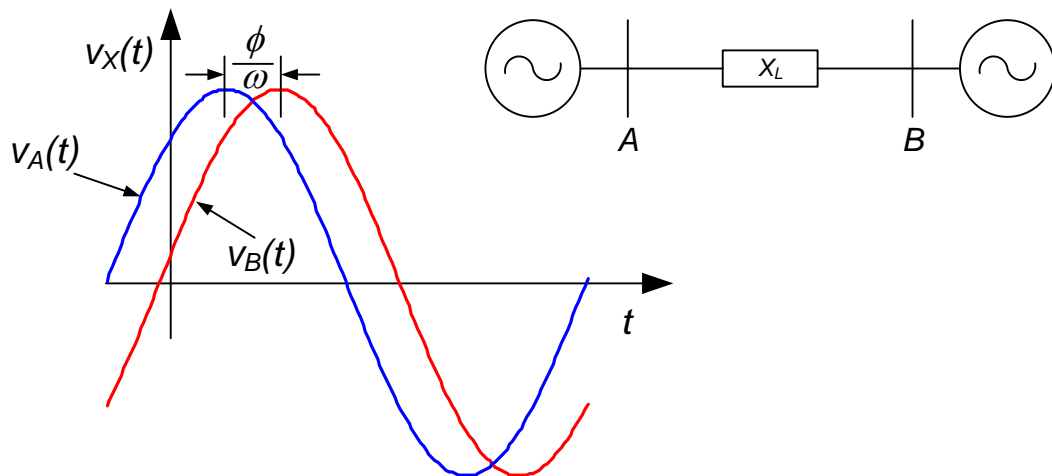
Figure 2.2 Voltages at different network locations.

Figure 2.3 illustrates voltage signals at Terminals *A* and *B* with respect to a common reference. PMUs at these terminals measure the phase angles, ϕ_A and ϕ_B, at the two locations with respect to a common reference. Then, (2.2) can be used to calculate the phase angle difference ϕ between the two signals.

$$\phi = \phi_A - \phi_B \qquad\qquad (2.2)$$
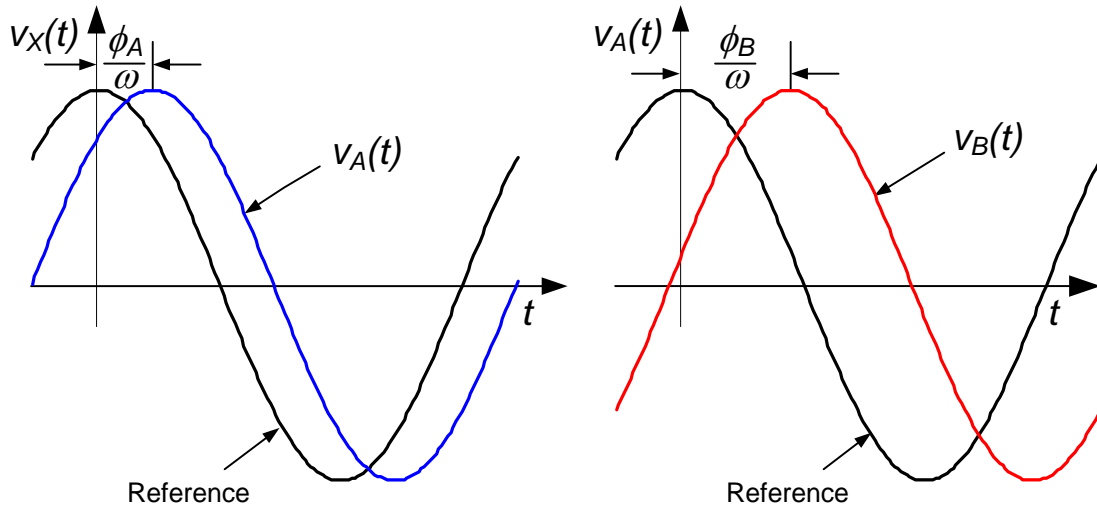
Figure 2.3   Voltages at different network locations with a common reference.

2.1.3 Phasor Angle Measurement at Off-Nominal Frequencies

Reference [35] mentions that most of the literature about synchrophasor measurements does not discuss the performance of these measurements at off-nominal frequencies; [35] shows why synchrophasor measurements can be used under these conditions. A sinusoidal voltage signal for off-nominal frequency operating conditions can be expressed according to (2.3).

$$v(t) = A \bullet \text{Re}\{e^{j(2 \cdot \pi \cdot f \cdot t + \phi)}\} = A \bullet \text{Re}\{e^{j\theta(t)}\} = A \bullet \text{Re}\{e^{j(2 \cdot \pi \cdot f_0 \cdot t)} \bullet e^{j(2 \cdot \pi \cdot \Delta f \cdot t)} \bullet e^{j\phi}\} \qquad (2.3)$$

where:
   f_0 is the nominal frequency in Hz,

   Δf is the frequency deviation from nominal frequency, $f - f_0$, in Hz.

Equation (2.4) represents the argument $\theta(t)$ of a cosine function at off-nominal frequency. This argument has three components:

- The angle that is a function of nominal frequency, $2 \bullet \pi \bullet f_0 \bullet t$.
- The angle that is a function of the frequency deviation from nominal, $2 \bullet \pi \bullet \Delta f \bullet t$.
- The phase angle at $t = 0$, ϕ .

$$\theta(t) = 2 \bullet \pi \bullet f_0 \bullet t + 2 \bullet \pi \bullet \Delta f \bullet t + \phi \qquad (2.4)$$

The subtraction of $2 \bullet \pi \bullet f_0 \bullet t$ from $\theta(t)$ results in an angle $\beta(t)$ that includes the angle that is a function of the frequency deviation from nominal and the phase angle, ϕ. Equation (2.5) represents this resulting angle, which provides information about power system dynamic behavior.

$$\beta(t) = 2 \bullet \pi \bullet \Delta f \bullet t + \phi \qquad (2.5)$$

At nominal frequency, $\Delta f = 0$ and $\beta(t) = \phi$. At off-nominal frequency, $\beta(t)$ changes with time. Figure 2.4 shows two voltage signals: one with $\Delta f = 0$ Hz and $\phi = 30°$ at $t = 0$, and the other with $\Delta f = 5$ Hz and $\phi = 30°$ at $t = 0$. The dotted trace shows the signal at nominal frequency, while the solid trace corresponds to the off-nominal frequency signal. The two signals depart from each other as β increases; Figure 2.5 shows how β increases as time increases for a constant and positive Δf.
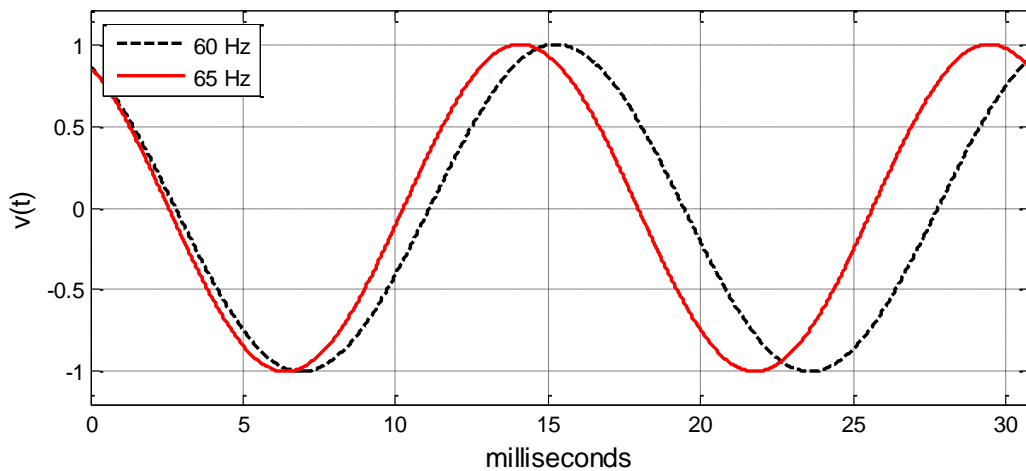
Figure 2.4   The phase delay, β, increases according to the frequency deviation, Δf.
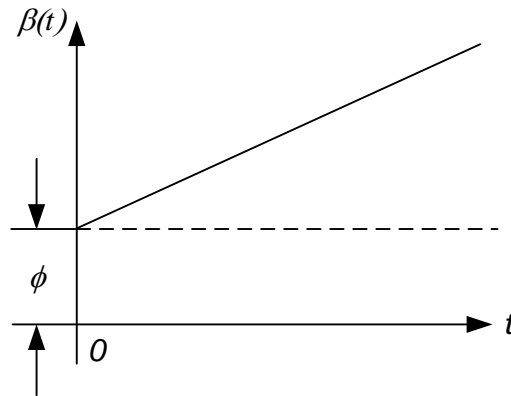
Figure 2.5   Phase measurement at off-nominal frequency for $\Delta f > 0$; $\beta (t) = 2\pi \cdot \Delta f \cdot t + \phi$. The phase delay, β, increases according to the frequency deviation, Δf.

If we compare the angle measurement, β, at two locations in the same power system and same off-nominal frequency and with constant ϕ_x at particular instants in time, the angle difference, $\Delta\beta$, is constant and equal to ϕ, as shown in Figure 2.6. Equation (2.6) expresses the angle difference of two signals with constant Δf. Therefore, $\Delta\beta$ provides power system information of interest for wide-area protection and control applications.

$$\Delta\beta = \beta_A(t) - \beta_B(t) = (2\cdot\pi\cdot\Delta f\cdot t + \phi_A) - (2\cdot\pi\cdot\Delta f\cdot t + \phi_B) = \phi \qquad (2.6)$$
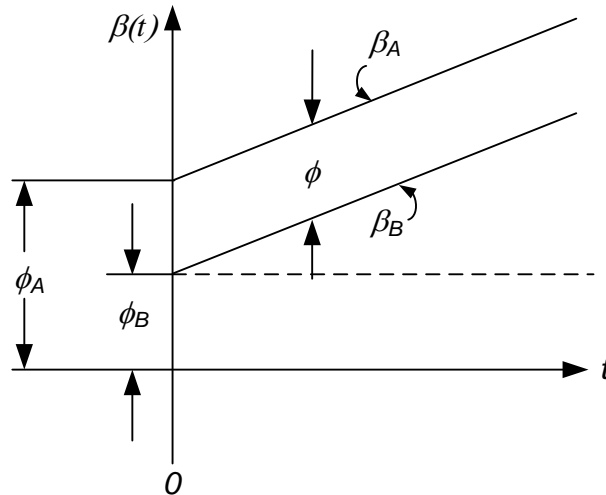
Figure 2.6   Off-nominal frequency phase measurements obtained at two locations. The angle difference between the two measurements, $\varDelta\beta$, remains constant.

2.2   PMU Sampling and Signal Processing Practices

This section describes the two most popular sampling and signal processing methods for estimating synchrophasors [36]. These popular methods sample voltages and currents at fixed time intervals (constant number of samples per second) with respect to an absolute time reference. The first method uses the Fourier transform technique [7], while the second method uses the demodulation (correlation) technique [15].

2.2.1   Fourier Transform Based Method

Traditionally, PMUs acquire data at fixed time intervals to provide voltage and current oscillography and synchrophasor measurements. For example, PMUs use sampling rates of 16 times the nominal system frequency or faster. The samples are synchronized to an external time source. In synchrophasor applications, the external time source is an absolute time reference from a global positioning system (GPS) receiver [37].

Figure 2.7 shows a typical PMU data acquisition block diagram; the figure includes a hardware low-pass filter (LPF) for antialiasing, an analog-to-digital converter (ADC) for analog-to-digital conversion, an external time source with absolute time reference that determines the sampling interval, and the DFT-based synchrophasor estimation [36, 38].
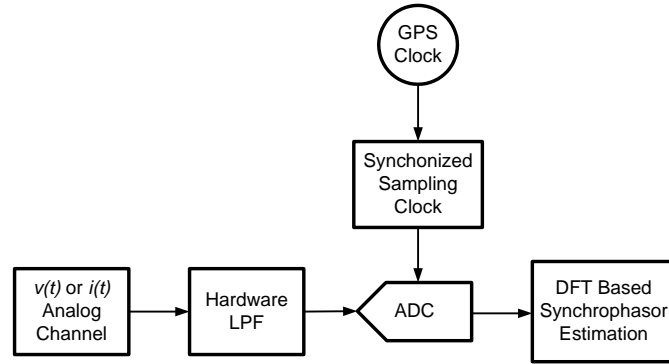
Figure 2.7   Sampling at fixed time intervals with an absolute time reference for synchronized phasor measurement, oscillography, and harmonic analysis.

It is well documented in the literature that DFT based phasor calculations are in error when the power system operates at off-nominal frequencies [39]. Equation (2.7) represents a sinusoidal signal *x(t)* in discrete form x_k with a processing interval Δt. The sampling rate f_s is the multiplicative inverse of the processing interval Δt where *X* is the phasor that represents *x(t)* in steady state (see *Appendix A*).

$$x_k = \frac{1}{\sqrt{2}}\left(X e^{ik\omega\Delta t} + \overline{X} e^{-ik\omega\Delta t} \right)$$

(2.7)

The discrete Fourier transform (2.8) with an observation window of *N* samples is used to obtain the nominal frequency ($\omega_0 = 2\cdot\pi\cdot f_0$) phasor χ_r. In (2.8), *r* corresponds to the initial sample of the observation window [40]. The ½ factor creates coefficients with central symmetry.

$$\chi_r = \frac{\sqrt{2}}{N} \sum_{k=r}^{r+N-1} x_k e^{-i(k+1/2)\omega_0\Delta t}$$

(2.8)

By substitution of (2.7) in (2.8), χ_r is obtained in terms of *X* as expressed in (2.9).

$$\chi_r = \frac{1}{N} \sum_{k=r}^{r+N-1} \left(X e^{ik\omega\Delta t} + \overline{X} e^{-ik\omega\Delta t} \right) e^{-i(k+1/2)\omega_0\Delta t}$$

(2.9)

The estimated χ_r consists of the frequency difference ($\omega - \omega_0$) and the frequency sum ($\omega + \omega_0$) components. The first term in (2.10) corresponds to the frequency difference χ_{r_DIF} component, and the second term χ_{r_SUM} corresponds to the frequency sum component.

$$\chi_r = \frac{1}{N}\sum_{k=r}^{r+N-1} X e^{i(k+1/2)(\omega-\omega_0)\Delta t} + \frac{1}{N}\sum_{k=r}^{r+N-1} \overline{X} e^{-i(k+1/2)(\omega+\omega_0)\Delta t} = \chi_{r\_DIF} + \chi_{r\_SUM} \qquad (2.10)$$

The simplified expression (2.11) defines the phasor as a function of the initial sample r, the operating frequency f, and the phase angle ϕ.

$$\chi_r(r,f,\phi) = \chi_{r\_DIF}(r,f,\phi) + \chi_{r\_SUM}(r,f,\phi) \qquad (2.11)$$

Figure 2.8 shows the phasor estimations produced by using (2.11) for 30, 45, 60, 75, and 90 Hz with $N = 32$, $r = 0$, and $0 \le \phi \le 360°$ (*Appendices C* and *D* include Mathcad® and MATLAB® script files that generate this figure). The phasors that correspond to $f = 60$ Hz plot a circle with constant magnitude, while the phasors for the off-nominal frequencies plot ellipses with variable magnitude. The error at off-nominal frequency needs to be compensated according to the deviation from nominal frequency for obtaining accurate single phase phasor estimation (e.g. A-phase voltage).
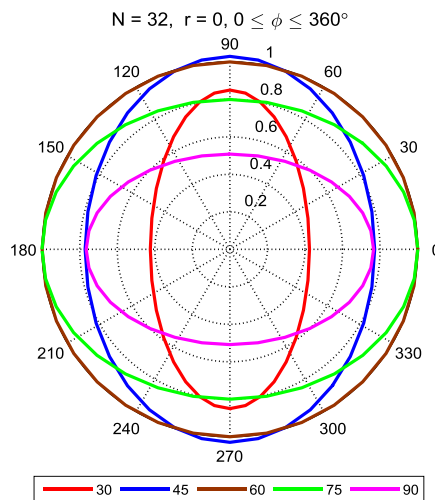
Figure 2.8   Phasor estimation at 30, 45, 60, 75, and 90 Hz.

2.2.2   Quadrature Demodulation Method

The quadrature demodulation (or correlation) method consists of multiplying the voltage or current input signal by a complex exponential with nominal frequency ω_0. For example, in (2.12), a voltage signal *v(t)* is multiplied by a time-synchronized unit phasor $e^{-j\omega_0 t}$ to obtain the correlated signal $v_{corr}(t)$.

$$v_{corr}(t) = v(t) \bullet e^{-j\omega_0 t} = V \bullet \cos\left(\omega \bullet t + \phi\right) \bullet e^{-j\omega_0 t}$$
(2.12)

Equation (2.13) expresses $v_{corr}(t)$ in terms of exponential functions.

$$v_{corr}(t) = V\left[\frac{e^{j(\omega t + \phi)} + e^{-j(\omega t + \phi)}}{2}\right] e^{-j\omega_0 t}$$
(2.13)

$v_{corr}(t)$ can also be represented according to (2.14).

$$v_{corr}(t) = \frac{V}{2}\left[e^{j\left[(\omega - \omega_0)t + \phi\right]} + e^{-j\left[(\omega + \omega_0)t + \phi\right]}\right]$$
(2.14)

Equation (2.14) has two terms: the low-frequency term that corresponds to the frequency difference $(\omega - \omega_0)$ (2.15),

$$v_{corr\_dif}(t) = \frac{V}{2} \bullet e^{j\left[(\omega - \omega_0)t + \phi\right]}$$
(2.15)

and the near double frequency term that corresponds to the frequency sum $(\omega + \omega_0)$ (2.16),

$$v_{corr\_sum}(t) = \frac{V}{2} \bullet e^{-j\left[(\omega + \omega_0)t + \phi\right]}$$
(2.16)

The frequency difference component $v_{corr\_dif}(t)$ is the quantity that provides the information of interest for power system analysis; $v_{corr\_dif}(t)$ can be obtained by filtering out the frequency sum component $v_{corr\_sum}(t)$. The resulting signal has the input signal amplitude divided by two. After proper scaling, $v_{corr\_dif}(t)$ can be represented in phasor form according to (2.17).

$$\vec{V} = \frac{V}{\sqrt{2}} \angle \beta(t) \tag{2.17}$$

where:

$$\beta(t) = (\omega - \omega_0) \cdot t + \phi.$$

Figure 2.9 illustrates the signal processing required to estimate synchrophasors through use of the quadrature demodulation method. The input signal (voltage or current) passes through a traditional anti-aliasing hardware low-pass filter (LPF). The synchronized sampling clock that uses a GPS for absolute time reference controls the sampling interval of the analog-to-digital converter (ADC) to obtain samples at fixed time intervals. The synchronized sampling clock is also used to generate the reference signal. The digital signal output of the ADC is multiplied by the reference signal to obtain the quadrature components. Digital LPFs provide harmonic and interharmonic attenuation. The resulting quadrature signals — the real and imaginary parts of the synchrophasor — are used to calculate the magnitude and angle of the synchrophasor.
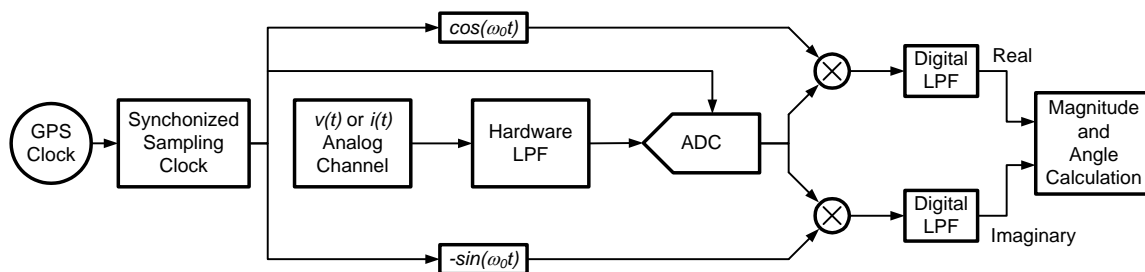
Figure 2.9   Quadrature demodulation signal processing for synchrophasor estimation.

2.3   Total Filtering Magnitude Frequency Response

The total filtering magnitude frequency response indicates if a particular filtering process is suitable for a specific application. Figure 2.10 shows the total filtering magnitude frequency response when using the DFT method with $N = 16$ and $f_s = 960$ Hz. This filtering process has the low-frequency - 3 dB cut-off frequency at 31.80 Hz and the high-frequency - 3 dB cut-off frequency at 87.09 Hz that define the filter pass-band frequencies. This filtering process heavily attenuates all the harmonics but poorly attenuates interharmonics. For example, the attenuation at 146.25 Hz is only 12.57 dB.
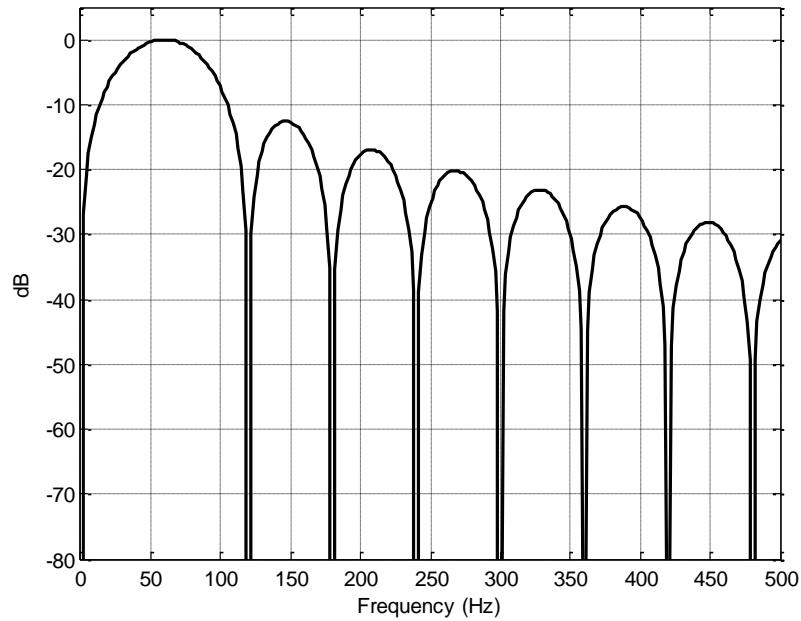
Figure 2.10   Total filtering magnitude frequency response when using the DFT method with an observation window of 16 taps and a sampling frequency of 960 Hz.

The DFT method lacks adequate filter response for SIPSs that detect inter-area oscillations. For this application, it is desirable to have a flat passband within a predetermined frequency range and heavy attenuation outside this frequency range. Figure 2.11 shows the total filtering magnitude frequency response of a PMU that uses the quadrature demodulation method for 60 msg/s applications. The filtering provides less than 3 dB attenuation from 45.53 Hz to 74.42 Hz and attenuation exceeding 30 dB for frequencies less than 36.88 Hz and greater than 83.01 Hz, making this filtering process suitable for detecting inter-area oscillations. This is the method used in the applications this dissertation proposes.
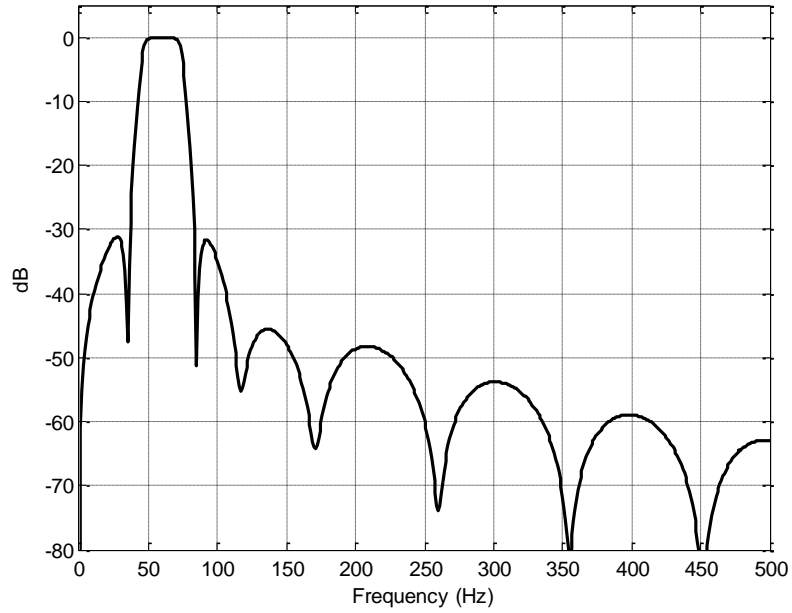
Figure 2.11   Total filtering magnitude response when using the quadrature demodulation method with a fourth order Chebysheb Type II filter, a 10 tap Kaiser window, and a sampling frequency of 1 kHz.

To examine the influence of message rates in the desirable filtering bandwidth requirements, Figure 2.12 shows the magnitude frequency response of the 60 and 30 msg/s filtering processes used in the applications this work proposes. Notice that for 30 msg/s the frequency bandwidth is narrower (from 52.29 to 67.71 Hz) and exceeds 30 dB attenuation for frequencies less than 43.82 Hz and greater than 76.18 Hz to avoid signal aliasing problems.

Because of communication network bandwidth limitations, a rate of 30 msg/s is frequently used in wide-area protection system applications.
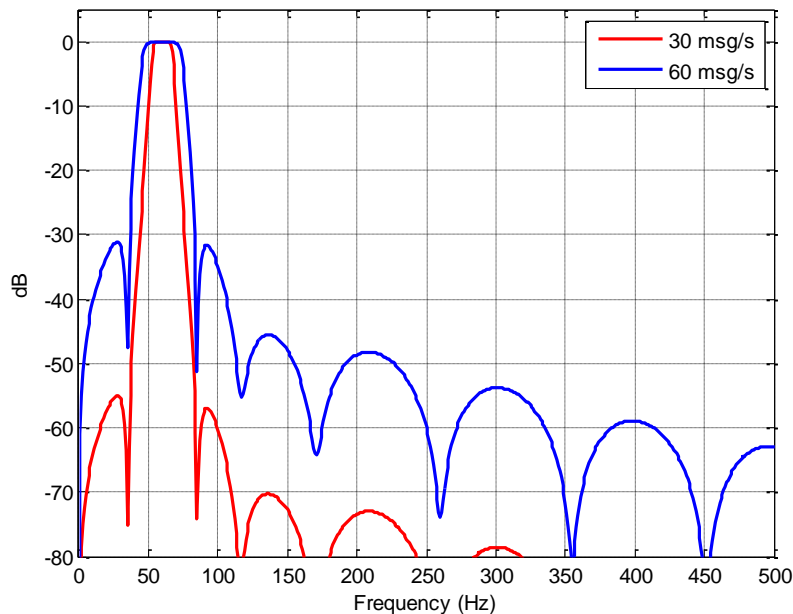
Figure 2.12   Total filtering magnitude frequency response when using the quadrature demodulation method for 60 and 30 messages per second.

2.4   Total Filtering Step Response

Figure 2.13 shows the step responses for the 30 and 60 msg/s quadrature demodulation filtering processes. For 30 and 60 msg/s, the signals reach 90 percent of their values in 84 and 44 ms, respectively. The overshoot values of the 30 and 60 msg/s filters are 11.6 and 13.8 percent, respectively. Table 2.1 summarizes the characteristics of these filters. These operating times and overshoot values are acceptable for the applications following chapters propose.
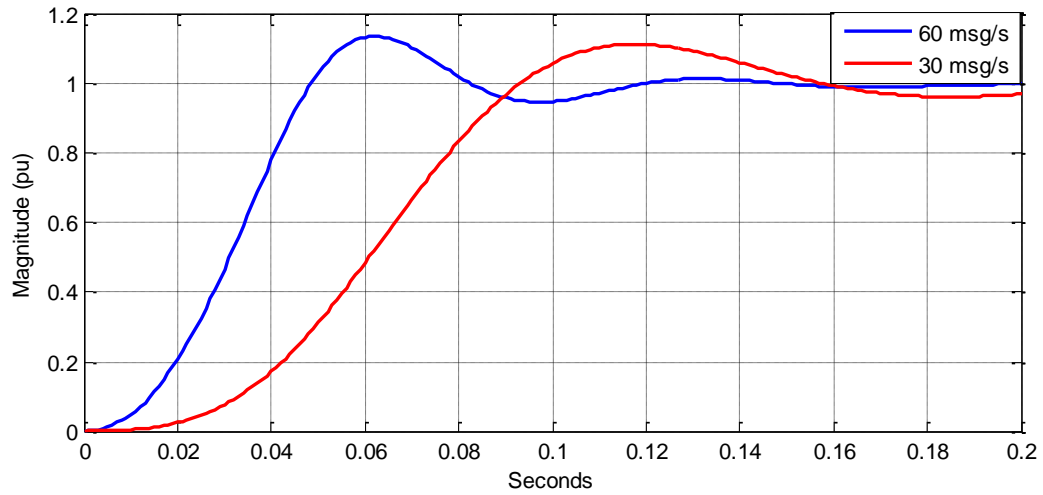
Figure 2.13   Step responses of the quadrature demodulation filtering process for 30 and 60 messages per second.

Table 2.1   Characteristics of the 30 and 60 msg/s filters used in the quadrature demodulation method.

Characteristic	30 msg/s	60 msg/s
- 3 dB Pass Band (Hz)	52.29 to 67.71	45.53 to 74.42
- 30 dB Stop Band (Hz)	f < 43.82 and f > 76.18	f < 36.88 and f > 83.01
Overshoot (Percentage)	11.6	13.8
Rise Time to 90 Percent (ms)	84	44

2.5   Phasor Data Concentration and Real-Time Processing

In wide-area protection and control applications, PMUs send synchrophasor measurements from different geographical locations to a central location. This central location can be at a regional level or at the control center. Figure 2.14 shows a wide-area network with PMUs that measure bus voltages at the same instant t_1 at different power plant locations of the power system. These measurements are sent to a PDC through a wide-area network (WAN) where data are concentrated and time aligned. Synchrophasor data concentration and time alignment can be performed in PDCs, PMCUs, and synchrophasor processing units (SPUs).
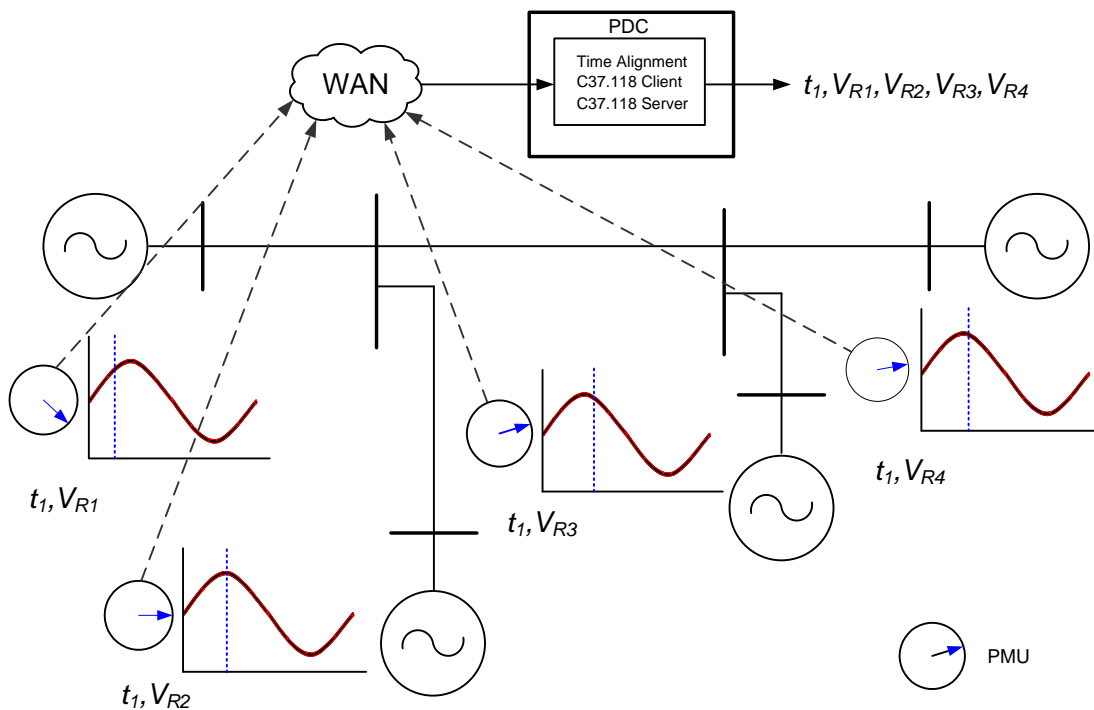
Figure 2.14   Time alignment is performed in the phasor data concentrator.

Typically, PDCs collect synchrophasors and align them based on their time stamps. The time-alignment process introduces a delay that must be considered in time critical applications such as SIPSs. In these applications, synchrophasors need to be aligned within a predetermined time interval. PDCs require an operating system with hard real-time capability — such as provided by a hard real-time operating system (RTOS) — to meet this requirement [41]. PDCs make the time-aligned synchrophasors available to applications such as visualization and disturbance

recording. PDCs with hard RTOS capability act as synchrophasor processors that run algorithms and logic for SIPSs.

2.6   Summary

This chapter describes the tools necessary for the research presented in the remainder of this dissertation. These tools include a synchrophasor estimation method, synchrophasor data concentration, and real-time synchrophasor data processing for wide-area power system disturbance detection and monitoring. Adequate signal processing that extracts the information of interest from voltage and current measurements and heavily attenuates signal components outside the frequency band of interest, fast step input response, and hard real-time processing are fundamental for detecting power system oscillations, taking prompt remedial actions, and preventing wide-area system disturbances.

The DFT method for estimating synchrophasors does not have adequate filter response for SIPSs that detect inter-area oscillations. This filtering process heavily attenuates all harmonics but poorly attenuates interharmonics. For example, the attenuation at 146.25 Hz of the DFT-based filter described in this chapter is 12.57 dB, while the attenuation at the same frequency with the quadrature demodulation filtering process for 30 messages/s is greater than 70 dB.

The quadrature demodulation or correlation method provides the required flexibility for tailoring the total filtering frequency and step responses to the requirements of a particular application.

SIPSs that use the synchrophasor processing units –presented in this chapter– for time aligning data, processing algorithms and logic within a fixed amount of time, and activating remedial action commands have fewer components and increased reliability when compared to traditional SIPSs.

Chapter 3 Automatic Generator-Shedding Scheme Using Synchrophasors

3.1   Introduction

Geographically speaking, power systems are probably the largest interconnected networks in service today and offer interesting engineering challenges. Generating sites are far from large load demand regions. In some cases, power plants are close to natural resources, while in other cases plants are in remote areas with less environmental restrictions. Because of this generation/load separation, a reliable power transmission network is necessary. Unfortunately, transmission networks are not easy to build. Right-of-way restrictions limit transmission line construction. In general, almost nobody wants to live close to a power plant or a transmission line. This limited network growth requires optimization of available resources. Engineers achieve this optimization by adding technologies such as series compensation, static VAR compensation (SVC), and phase shifters that increase network power transmission capability. As a result of this optimization, the power system operates closer to its stability limits. Additionally, the power industry is splitting generation, transmission, and distribution into separate operating entities, which complicates implementation of network-wide policies. A reliable power system maintains frequency and voltage excursions within acceptable limits under normal and abnormal operating conditions. In addition, thermal values must not exceed power system component operation limits. Finally, typical frequency limits are $f_{NOM} \pm 0.1$ Hz, while typical voltage limits are $V_{NOM} \pm 5$ percent.

Fink and Carlsen [42] identified five system-operating states (normal, alert, emergency, extreme, and restoration), as illustrated in Figure 3.1. The power system operates in a normal state when system frequency and voltages are close to nominal values and there is sufficient generation and transmission reserve.
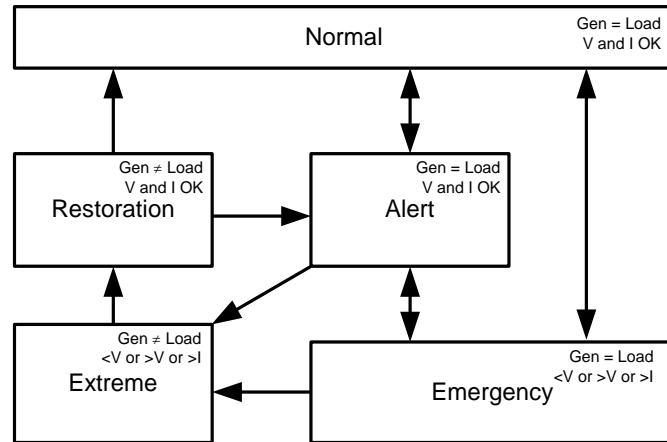
Figure 3.1   Fink and Carlsen diagram showing all possible power system operating states with normal/emergency state transitions added.

The system enters an alert state because of reduction or elimination of reserve margins, or for a problem with one or several system components (as, for example, when one or several lines are overloaded). In the alert state, automated and manual system controls operate to restore the system to the normal state within several seconds. Adequate power system monitoring and metering are necessary to promptly detect power system problems and accelerate system recovery [43].

The power system enters an emergency state for operating conditions that cause voltage or thermal limits to be exceeded or when a fault occurs. In the case of a fault, fault detection, clearance, and system restoration should cause minimum system disturbance. High-speed protective relays and breakers are necessary; speed and proper execution of corrective actions are critical in preventing the system from entering the extreme state. For example, high-speed transmission line protection with single-pole tripping – in less than one cycle – and adaptive reclosing – in less than one second – minimizes system disturbance [44]. When the system enters the emergency state without a system fault, automated control (fast valving, static VAR compensation, etc.) is necessary to reestablish the normal or alert operating state and prevent the system from entering the extreme state.

If the system cannot maintain the generation-load balance or maintain voltage within desirable limits, the system enters the extreme state. In the extreme state, load shedding, generation shedding, or system islanding occurs to balance generation and load or to restore voltage to acceptable levels. Underfrequency load-shedding schemes operate within a few cycles to restore load-generation balance across the system; undervoltage load-shedding schemes operate within a

few cycles to avoid system voltage collapse. System integrity protection schemes (SIPSs) that monitor such system characteristics as power flows, network topology, and voltage levels actuate to separate the system into islands or shed generation within one second for maintaining the load-generation balance and preventing total system collapse [11, 45]. After load and/or generation shedding, the system enters a system recovery state. In this state, manual or automated reinsertion of generation and load occurs.

Ideally, the power system should avoid reaching the extreme state. Unfortunately, there are many occasions in which power systems operate in this state. This chapter discusses traditional local- and wide-area protection systems focusing on synchrophasor-based SIPSs that minimize the risk of wide-area disruptions. The proposed synchrophasor-based schemes simplify complex wide-area schemes with multiple components. This chapter presents a synchrophasor-based automatic generator-shedding scheme (AGSS) with a minimum number of components and increased reliability.

3.2   Wide-Area System Disruptions

There are two main causes of wide-area disruptions:

- Voltage collapse.
- Rotor angle instability.

These events can occur independently or jointly. In some cases, system disruptions begin as voltage instability problems – where the voltage magnitude drops without control as time progresses – that evolve into rotor angle instability problems because of a failure to take proper actions to return the system from the emergency state to the alert or normal state.

3.2.1   Voltage Collapse

Taylor [46] refers to voltage collapse as follows:

"A power system at a given operating state and subject to a given disturbance undergoes voltage collapse if post-disturbance equilibrium voltages are below acceptable limits."

Voltage collapse can extend across the whole power system or be limited to a certain system area.

3.2.2   Rotor Angle Instability

When there is a reduction in transmission capacity because of transmission line disconnections or low-voltage operating conditions, power system generators cannot deliver predisturbance power to the system. Generator loss of synchronism can result from these abnormal system operating conditions if there are no actions taken to maintain proper generation/load balance.

The oscillogram in Figure 3.2 shows voltage at an extra high voltage (EHV) node while the system operates in the extreme state. In this case, the disturbance began as a voltage instability problem in which the voltage decayed below normal operating limits and no system actions were taken. Actions such as undervoltage load shedding could have restored the system to normal operation. At approximately 0.33 seconds (in this oscillogram), transmission lines tripped, reducing the network transmission capacity. After the transmission lines tripped, generators were unable to deliver predisturbance power to the system, and a rotor angle instability condition developed. This event is a clear example of how a voltage instability problem can evolve into a rotor angle instability problem.
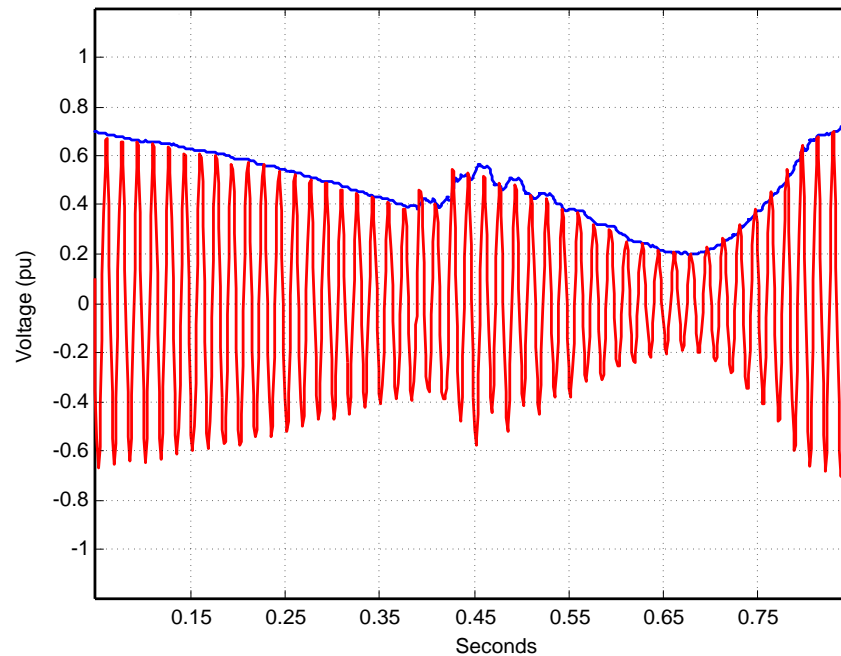
Figure 3.2   Voltage at an EHV node while the power system operates in the extreme state. This event shows how a voltage instability problem evolves into a rotor angle instability problem for lack of proper action to return the system to the normal or alert state.

3.3 Traditional Local- and Wide-Area Protection Systems

3.3.1 Local-Area Protection Systems

3.3.1.1 Underfrequency Load Shedding

When available generation is unable to supply load demand, the system experiences a frequency decline. Rapid action is necessary to maintain the generation-load balance. If there is no rapid response, additional generation could be lost because of underfrequency relay operation to trip steam turbine generating units. Traditionally, load shedding restores the generation-load balance. The traditional load-shedding scheme consists of underfrequency relays located at critical feeder locations. When the frequency drops below a preset value, the critical feeders are disconnected from the system. If the frequency continues to drop, other load-shedding stages are activated. Some underfrequency load-shedding schemes have as many as five underfrequency stages set at, for example, 59.2, 59, 58.8, 58.6, and 58.4 Hz in 60 Hz systems. Ideally, all underfrequency load-shedding schemes should have the same operating characteristic so that the schemes act simultaneously across the power system when the frequency drops below the predefined levels.

3.3.1.2 Undervoltage Load Shedding

The Protection Aids to Voltage Stability Power System Relaying Committee Working Group describes the undervoltage load-shedding scheme shown in Figure 3.3 [47, 48]. The scheme sheds the breaker load when the voltage in the three phases drops below 87 percent of nominal (27-2 undervoltage element). The scheme requires system-balanced operating conditions to operate; the undervoltage (U/V) scheme operates only when there is no zero-sequence voltage present. The 27-1 undervoltage element is connected in the open-delta potential transformer connection to detect zero-sequence voltage. Instantaneous overcurrent elements at the feeder location provide additional supervision to prevent U/V scheme operation during feeder fault conditions. If a three-phase undervoltage condition exists, there is no zero-sequence voltage, and there is no feeder fault, the timer starts and, after a certain time (one second, for example), the scheme sheds the feeder load. Schemes with different delays provide staggered load shedding to minimize voltage overshoot conditions after the load is shed.
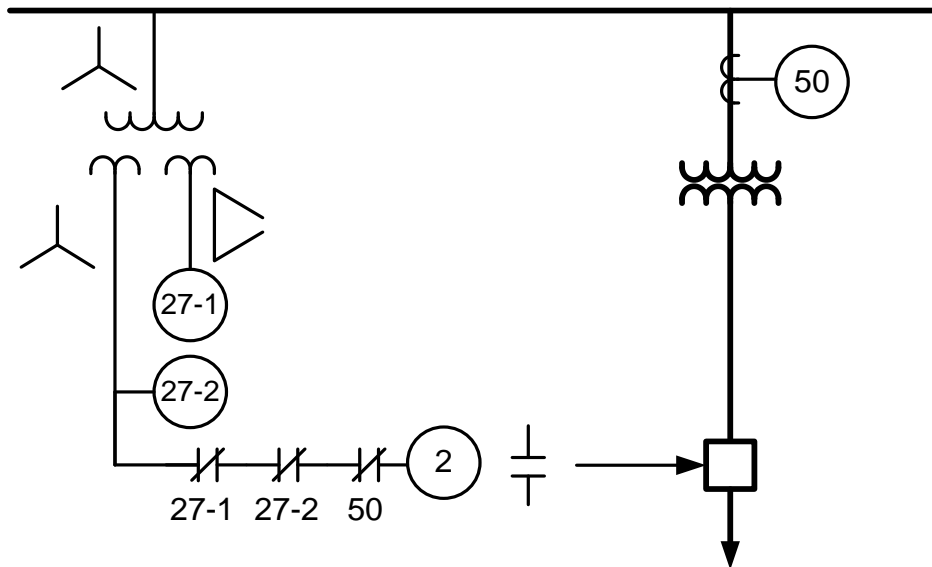
Figure 3.3   Undervoltage load-shedding scheme that operates only during balanced system conditions and during no feeder fault conditions.

3.3.2   Wide-Area System Integrity Protection Schemes

The local-area protection systems discussed in the previous subsection operate as a last resort after frequency or voltage is outside desired operating limits. SIPSs are designed to detect abnormal system conditions and take pre-planned, corrective actions intended to *minimize the risk of wide-area disruptions and to increase system power transfer capability*. Most typical SIPS actions include automatic tripping of generators and interruptible loads. To improve system reliability, SIPSs can be implemented through the use of new monitoring, protection, and communication technologies as will be described in the following text. Next, a two-contingency wide-area SIPS is described.

As was mentioned in Section 1.2, León et al. [11] describe a two-contingency remedial action scheme that prevents the system from near voltage collapse operation. In this description, the power system consists of three areas (see Figure 3.4):

- Area 1: Heavy load concentration.
- Area 2: Heavy generation concentration.
- Area 3: Light load concentration.

Areas 1 and 2 are interconnected with three transmission links; Areas 2 and 3 are interconnected with two transmission links. The remedial action scheme to avoid voltage collapse is enabled when the transmitted power from Area 2 to Area 1 exceeds 1100 MW, as Figure 3.5 illustrates. If two of the links open under these conditions, the scheme sheds excess generation in Area 2 in a timely manner (less than one second). Section 3.4.3 describes the functionality of a PMCU that allows programming of angle difference calculations across the power system through use of time-synchronized voltage measurements to improve reliability. Section 3.5 describes how an angle difference-based SIPS uses synchrophasors to prevent the system from collapsing; this scheme has been implemented in the field with minimum system components, making the scheme efficient and reliable.
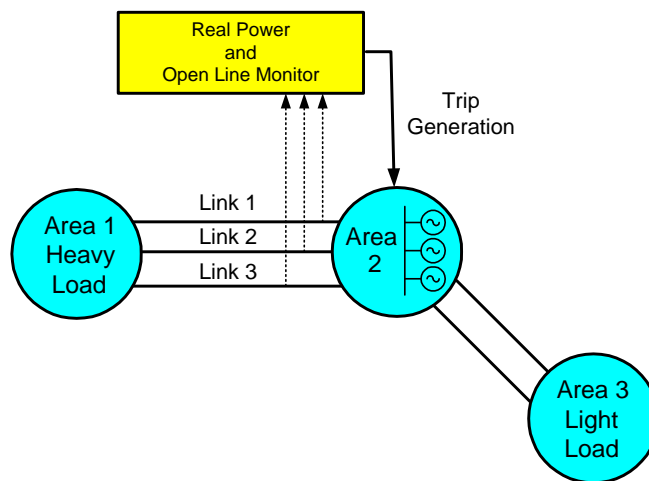
Figure 3.4   Area 2 generation depends on the system real-time power transmission capability.
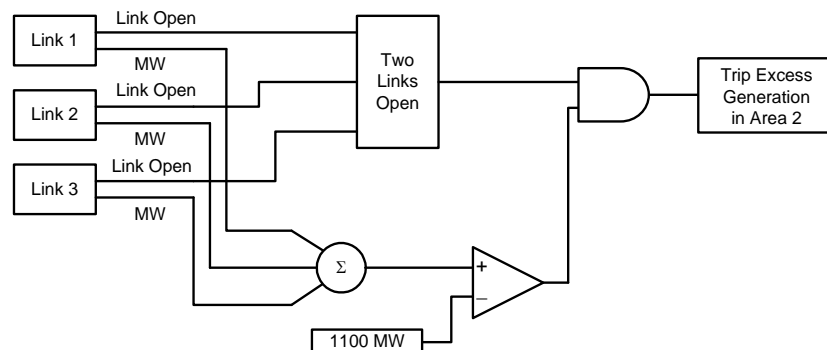
Figure 3.5   SIPS to shed Area 2 excess generation when two of the transmission links between Area 1 and Area 2 are open and the transmitted power from Area 2 to Area 1 exceeds 1100 MW.

3.4   Synchrophasor-Based SIPS

The absolute time reference of synchrophasor measurements aids in better assessment of the state of the power system over large geographical areas in real time than traditional state estimators. These measurements are therefore ideal for wide-area SIPS applications. As was mentioned in Section 1.2, BPA has been working on a SIPS that would act on actual power system responses rather than preset conditions and would potentially take only the necessary actions to maintain system stability. Such a SIPS would minimize outages, increase system reliability, and increase power transfer limits [49, 50].

BPA's response-based SIPS uses synchrophasors as basic input information (see Figure 3.6). PMUs at substations transmit synchrophasors in real time to a phasor data concentrator (PDC) at the control center. The PDC sends the combined data to a wide-area control system (WACS) controller that analyzes power system stability limits based on these data. If the power system operates close to its stability limits, the WACS controller takes the proper action through a wide-area protection system (WAPS) —usually a programmable logic controller— to avoid system collapse.
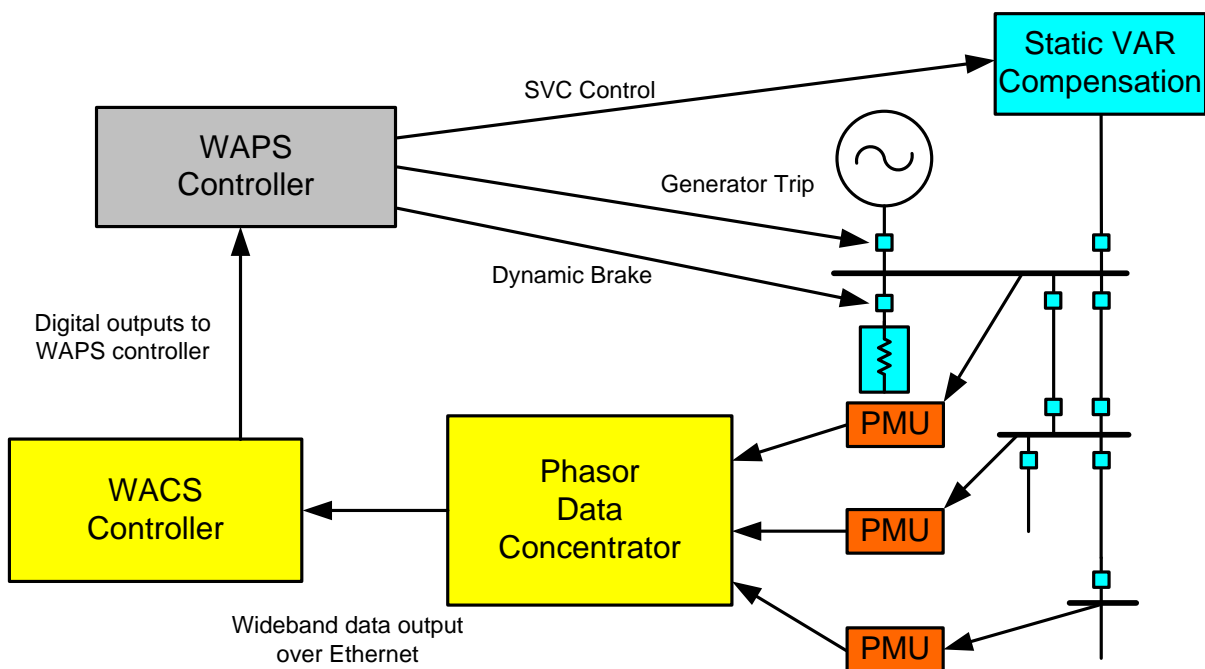
Figure 3.6   BPA's SIPS is based on synchrophasors.

3.4.1   Synchrophasor Processing Unit

The BPA SIPS can be simplified using phasor measurement and control units (PMCUs) and the

synchrophasor processing unit (SPU) shown in Figure 3.7. The SPU performs the PDC and WACS

functions of the system shown in Figure 3.6. It receives synchrophasors, analog quantities, and

binary inputs from remote PMCUs; correlates the received data according to their time stamps; and

processes protection and control algorithms through use of a hard real-time operating system.

Additionally, the SPU activates commands based on the processed data by using Fast Operate

commands embedded in C37.118.2 command messages [51]. The modified system together with

PMCUs is shown in Figure 3.8. The PMCUs receive fast message commands from the SPU and take

remedial actions to control and protect the power system. The overall system has fewer

components than BPA's SIPS, making it a more reliable system. *Chapters 5* and *6* describe

applications that use this technology to implement efficient and reliable SIPSs.
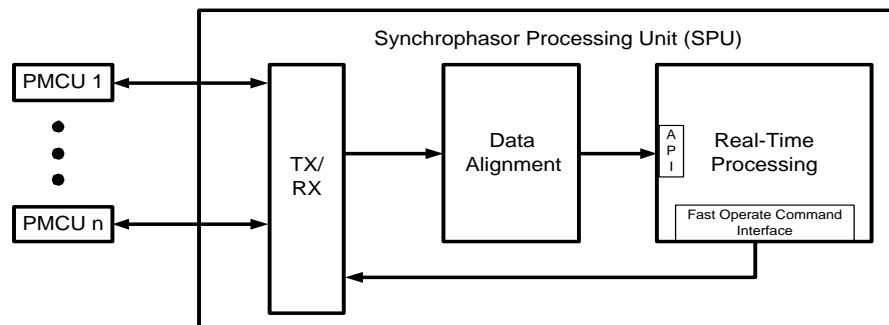
Figure 3.7   Synchrophasor processing unit for SIPS applications.
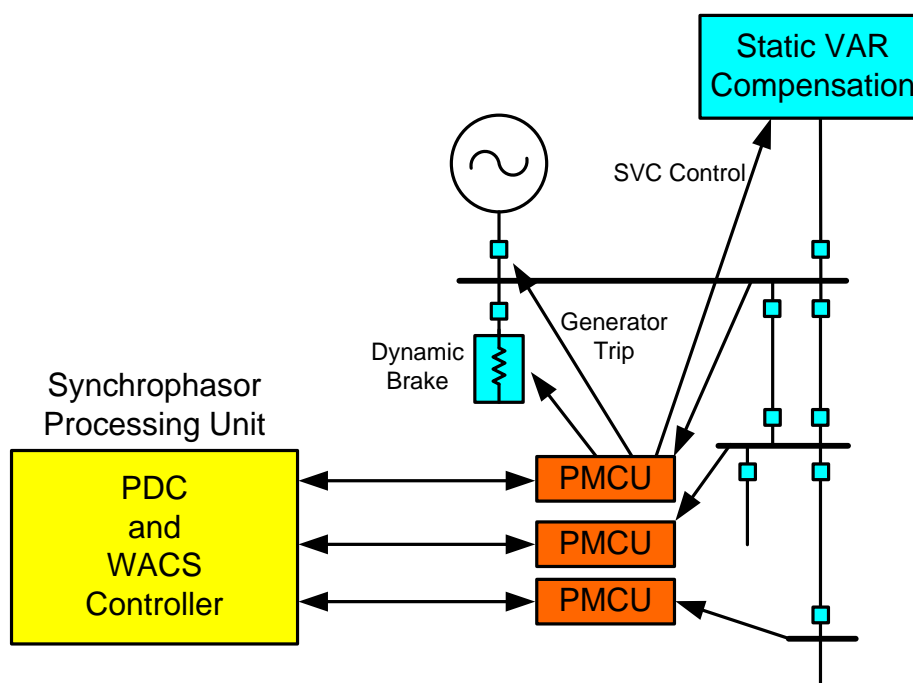
Figure 3.8   Integrated SIPS that uses SPU and PMCUs simplifies wide-area protection and control applications.

3.4.2   Phasor Measurement and Control Units

BPA's SIPS uses a WAPS controller to send commands back to the substations and power plants because of limitations with traditional PMUs that only send synchrophasor messages from the substation or power plant to the PDC but cannot receive commands and execute remedial actions. The PMCUs, shown in Figure 3.8, use bi-directional interleaved communications. They output 12 synchronized phasor measurements including phase and positive-sequence voltages (V_A, V_B, V_C, and V_1) and phase and positive-sequence currents from two sets of current transformers (IW_A, IW_B, IW_C, IW_1, IX_A, IX_B, IX_C, and IX_1). The PMCUs also output frequency, change of frequency with respect to time, 8 analog quantities, and 32 digital status values with their corresponding time stamps. The PMCUs also send PMCU configuration files upon request. The configuration files include such data as identification, number of phasors, number of analogs, number of digital status values, and data transmission rate. Refer to [51] for additional information.

The PMCUs also receive commands from the SPU. They can activate outputs for control and protection purposes. The PMCUs run programmable logic in a deterministic fashion. The PMCUs output data according to the IEEE Std C37.118.2 [51]. The connections from the PMCUs to the SPU

can be established through use of EIA-232 serial port communications or an Ethernet network. PMCUs are fundamental components of the schemes this work presents.

3.4.3 Phasor Measurement, Phasor Data Concentrator, and Real-Time Control Unit

A more advanced device includes synchrophasor measurement, synchrophasor time alignment, synchrophasor data concentration, real-time processing, and real-time control capabilities [24, 52, 53]. Simple SIPSs such as the scheme based on the angle difference between synchrophasors (presented later in this chapter) can be implemented by using this advanced PDC/PMCU device to further minimize the number of system components. See Figure 3.9.
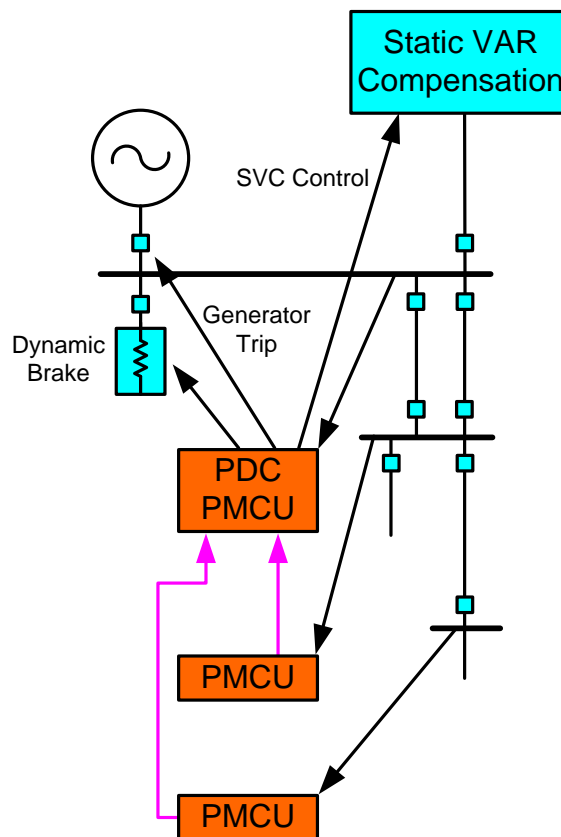
Figure 3.9   SIPS that uses one PDC/PMCU and two PCMUs.

The synchrophasor real-time control network, shown in Figure 3.10, includes one local PDC/PMCU and two remote PMCUs that exchange synchronized measurements and commands through a communication network for real-time control. The PMCUs correspond to the ones described in [35,

54]. The PDC/PMCUs transmit and receive synchronized measurement messages and command messages according to IEEE Std C37.118.2 [51] and Fast Message protocols. The PMCUs have EIA-232 and Ethernet communication ports. The local PDC/PMCU receives and decodes these messages according to the type of communications and protocols among devices. After the PDC/PMCU decodes the messages, the local data are resampled to match the rate of the received data. Then the PDC/PMCU aligns the remote (e.g., t_{STAMP}, V_{RPMR}, V_{RPMI}) and local (e.g., t_{STAMP}, V_{LPMR}, V_{LPMI}) messages according to their common time stamp, t_{STAMP}, to create delayed local quantities (e.g., t_{STAMP}, V_{DPMR}, V_{DPMI}). The remote and local quantities correspond to the values on the power system at a time equal to the acquisition time delay plus the channel latency. Table 3.1 illustrates an example of delayed local and remote quantities available in the local PDC/PMCU after decoding and time alignment. These quantities are available to the real-time math processor. The real-time math processor performs logic and arithmetic operations to implement protection and control schemes through use of synchrophasors.
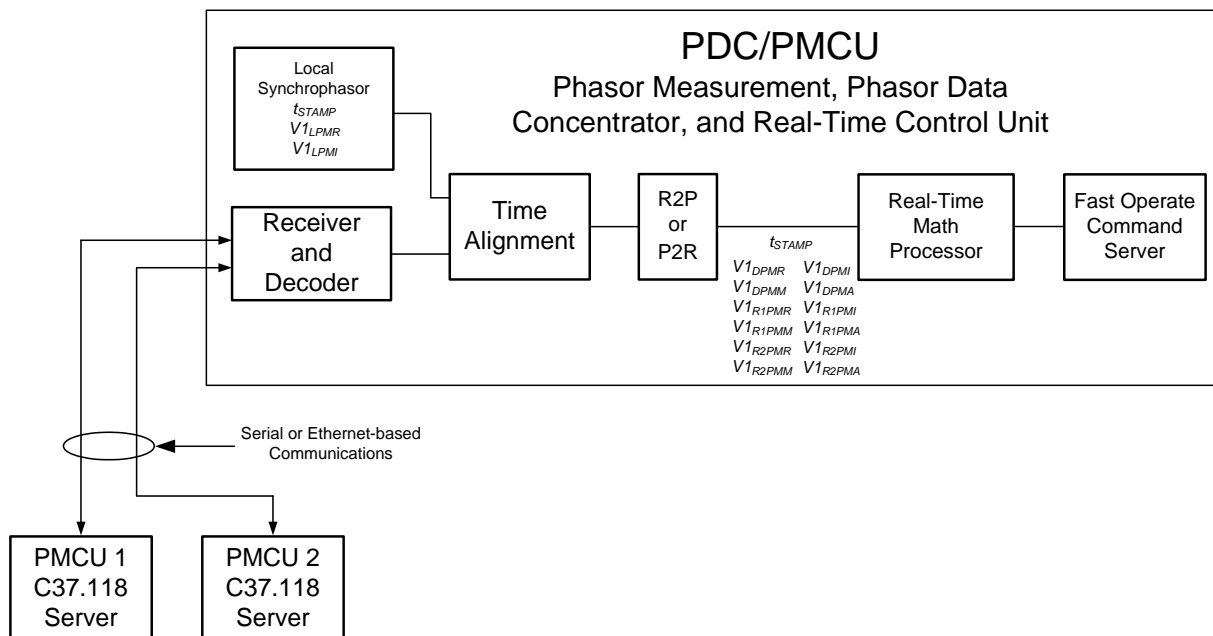
Figure 3.10   Synchrophasor real-time control with one local PDC/PMCU device and two remote
PMCUs.

Table 3.1 Synchrophasor data after time alignment.

Real Quantity	Description
$V1_{DPMR}$	Real part of the delayed local positive-sequence voltage.
$V1_{DPMI}$	Imaginary part of the delayed local positive-sequence voltage.
$V1_{DPMM}$	Magnitude of the delayed local positive-sequence voltage.
$V1_{DPMA}$	Angle of the local delayed positive-sequence voltage.
$V1_{RPMR}$	Real part of the remote positive-sequence voltage.
$V1_{RPMI}$	Imaginary part of the remote positive-sequence voltage.
$V1_{RPMM}$	Magnitude of the remote positive-sequence voltage.
$V1_{RPMA}$	Angle of the remote positive-sequence voltage.

The automatic generator-shedding scheme introduced in Section 3.5.3 uses the system shown in Figure 3.10 to measure the positive-sequence voltages at both ends of the transmission line, calculate the positive-sequence voltage angle difference between the two line terminals, and detect when this angle difference exceeds a predefined threshold. Figure 3.11 shows the programming required to produce the logic to detect angle differences greater than $10°$. The last line FOP01 activates a Fast Operate command when the PMCU detects this condition. The PMDOKT bit indicates that the synchrophasor data are valid and supervises the command to avoid misoperations when synchronized measurements are not reliable.

```
 1:   PMV53 := V1DPMA
 2:   PMV54 := V1RPMA
 3:   PMV58 := V1DPMA - V1RPMA
 4:   PSV01 := PMV58 >= 180.000000
 5:   PMV01 := -180.000000
 6:   PSV02 := PMV58 <= PMV01
 7:   PMV01 := PMV58 + 360.000000
 8:   PMV02 := PMV58 - 360.000000
 9:   PMV58 := NOT PSV01*PMV58+PSV01*PMV02
10:  PMV58 := NOT PSV02*PMV58+PSV02*PMV01
11:  PMV57 := ABS(PMV58)
12:  FOP01 := (PMV57 > 10.000000) AND PMDOKT
```

Figure 3.11   Logic to detect that the positive-sequence voltage angle difference between the local and the remote stations exceeds $10°$.

3.5 Automatic Generator-Shedding Scheme Using Time-Synchronized Measurements

Loss of generation or load because of power system faults causes changes in power system frequency and/or voltages. These changes depend on the power system robustness and the ability of regulating systems to respond to these changes. Furthermore, each power system has a unique dynamic behavior that depends on factors such as network transmission topology, load location, generation capacity, type of generation, etc. The automatic generation control (AGC) plays an important role in maintaining the load-generation balance in the system. This balance can suddenly be lost because of system contingencies. This lack of balance may result in changes in frequency, voltage magnitudes, and voltage angles according to the amount of generation/load lost. This section describes a proposed SIPS that uses synchrophasor angle difference as a key signal to determine allowable power stability margins. This SIPS uses the PDC/PMCU system shown in Figure 3.10 for improving scheme efficiency and reliability. The scheme is a generation-shedding scheme in a 400 kV transmission network that uses voltage synchrophasor angle difference to improve scheme reliability. Such a scheme is known as an automatic generator-shedding scheme (AGSS) [24].

Generation shedding is used as a last resort to maintain the power load/generation balance while preserving system voltages and frequency within allowable operating limits [42] [43]. Generation shedding also helps to preserve the transmission limits in critical links without exceeding transmission line, transformer thermal limits. Large hydroelectric plants that are typically at remote locations — with scarce local loads — depend heavily on the health of the transmission network. The power system can experience power transfer bottlenecks when part of the transmission network is lost, a condition that can cause system collapse.

Successful remote generation shedding relies mainly on communication-channel reliability. These schemes monitor the system topology to "arm" themselves and to select the generators to trip. A SIPS with minimum components and reliable communications is highly desirable.

3.5.1   Synchrophasor-Based Angle Difference Calculation

The total real power transfer, P_T, between two network buses, A and B, connected by a system transfer impedance, Z_T, is determined by the phase angle difference between the bus voltages, $\delta = \delta_A - \delta_B$, the voltage magnitudes at the buses, E_A and E_B, and Z_T. Figure 3.12 shows a transmission network with two buses connected by two transmission lines with a transfer impedance equal to half the line reactance X_L. The two buses exchange real power according to (3.1).
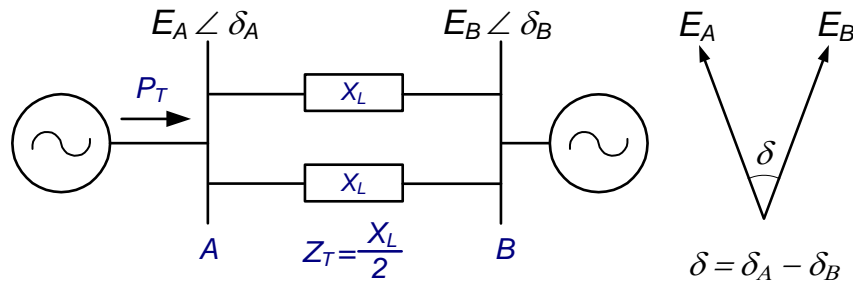
Figure 3.12 δ, E_A, E_B, and Z_T determine the total real power transfer, P_T, between Bus A and Bus B.

$$P_T = \frac{E_A \cdot E_B}{Z_T} \cdot \sin \delta \qquad (3.1)$$

During steady-state operating conditions, the voltage magnitudes of the network buses are close to one per unit. That is, the real power transfer capability depends mainly on the phase angle difference, δ, and the transmission transfer impedance, Z_T. Z_T depends on the number of lines and transformers in service between the two buses. When transmission lines are lost in strong systems during a system disturbance, Z_T increases and the angle difference also increases to maintain the same amount of real power exchange between the two buses; Figure 3.13 shows the increase in δ when one of the parallel lines opens.
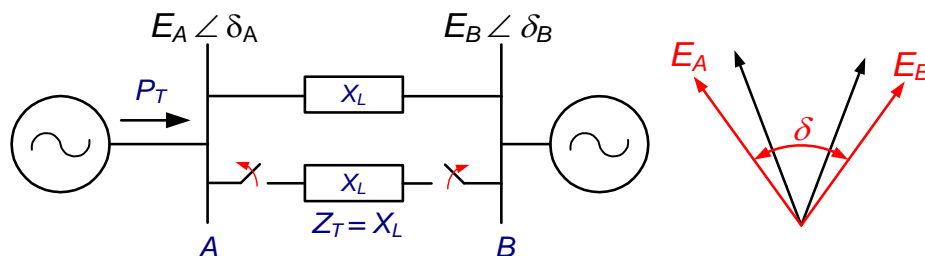
Figure 3.13   In strong systems, the voltage angle difference δ increases when one of the parallel lines opens.

Figure 3.14 illustrates the real power transfer capability and the real power transfer operating point as a function of the angle difference during normal operating conditions and after transmission links are lost because of a system disturbance. Notice that the increase in impedance between the system buses reduces the system maximum power transfer capability.
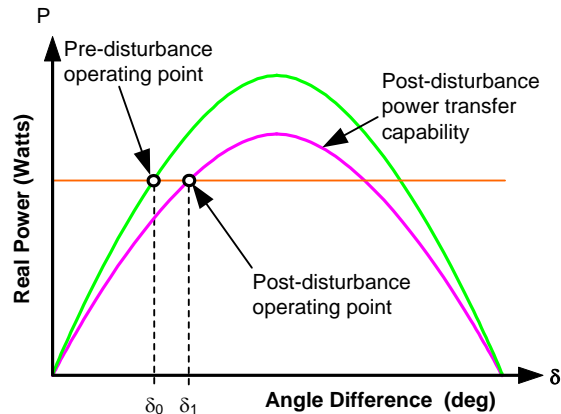
Figure 3.14   Real power transfer capability mainly depends on the angle difference δ and the transmission link impedance, Z_T, when E_A and E_B are close to nominal values.

For transmission links with several lines and intermediate substations, existing AGSSs monitor the network topology and power transfer capability by using open-line detectors for arming themselves, selecting generators to trip, or activating trip commands. The SIPS shown in Figure 3.4 and Figure 3.5 is one of these schemes. Open-line detectors are based on breaker auxiliary contact signals (52A or 52B), undercurrent, and/or under-active-power elements. Usually, these AGSSs use information from both ends of each transmission line to determine if the line is open. The number of open-line detectors that the system requires is twice the number of existing transmission lines in the scheme. For example, the six-transmission line system depicted in Figure 3.15 requires 12 open-line detectors (two per line) and several communication channels to accommodate double contingencies. For most AGSSs, the double contingencies of interest occur when two parallel transmission links are lost simultaneously. Notice that typically, the power system is normally designed and operated to withstand only single contingencies.
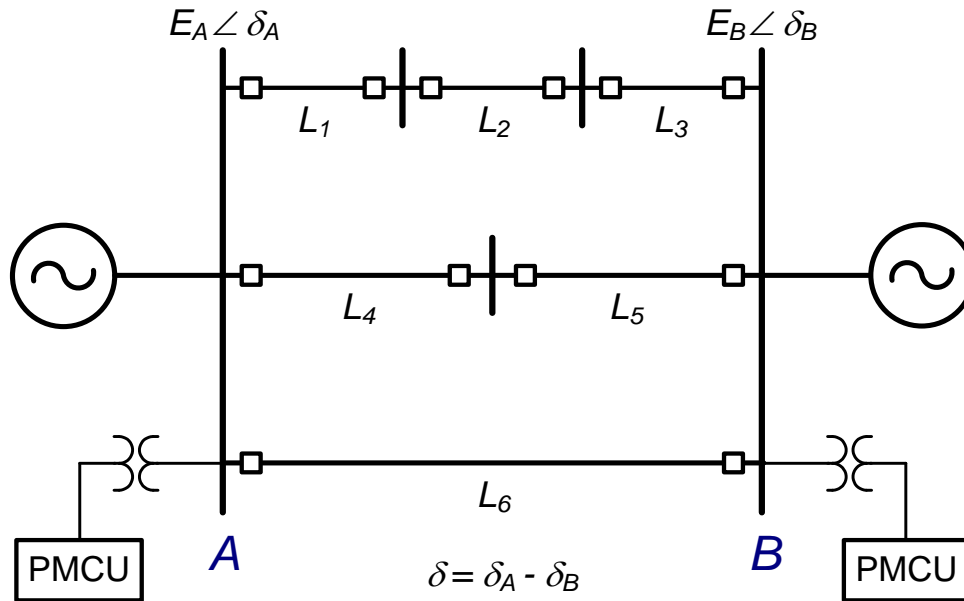
Figure 3.15 Power system network with six transmission lines requires 12 open line detectors and several communication channels to detect topology changes. Using voltage angle information instead of open line detectors simplifies the SIPS.

If the scheme uses the angle difference information, δ, between Bus A and Bus B, instead of the auxiliary contact signals, to detect a double contingency condition, the scheme only requires the two signals that contain the bus voltage angle information and one communication channel. With this information, the SIPS has fewer points of failure and is more reliable.

Figure 3.15 shows the locations of PMCUs to monitor the voltage angle difference between Bus A and Bus B and instantaneously detect changes in the transmission network transfer impedance. With this angle difference information, the SIPS can take action instantaneously.

The angle difference information between two buses can perform the following tasks:

- Arm the AGSS.
- Trip generation.
- Supervise existing AGSSs to increase security.

Because the angle difference measurement requires voltage measurements from only two locations, an AGSS based on the positive-sequence voltage angle difference between two buses at different locations of the power system is proposed in this section.

3.5.2 Power Generation and Transmission Challenges

As stated previously, one of the main reasons for using AGSSs is that large hydroelectric generation resources are often located far away from a heavy load region. Figure 3.16 depicts a hydroelectric generation complex where the distance between the heavy load region in the NS Network and large generation region shown in the figure is approximately 2000 km.
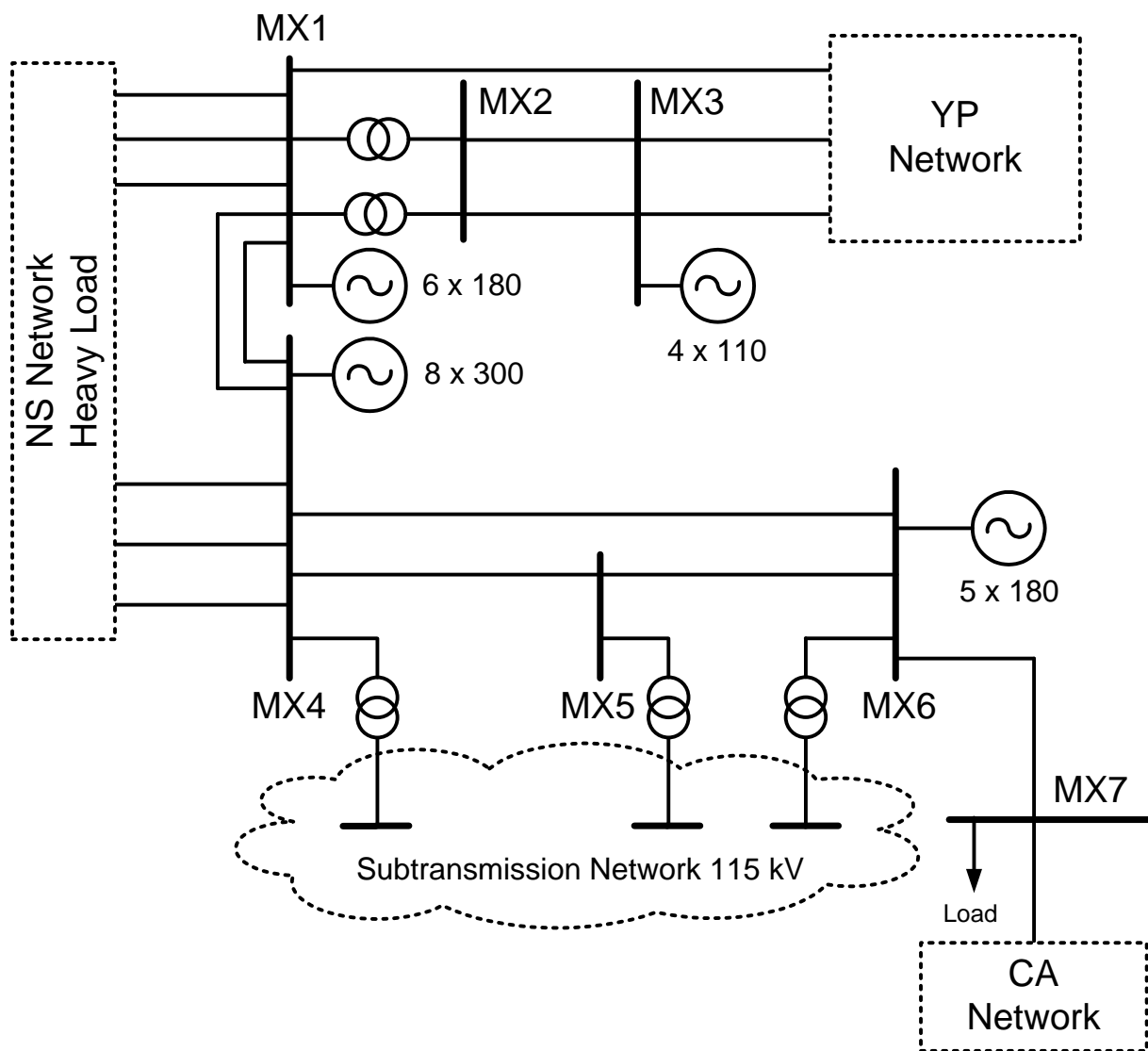
Figure 3.16 Hydroelectric generation and *MX4-MX6* transmission link with parallel 115 kV network.

One of the AGSSs in service at *MX6* monitors the loss of the 400 kV transmission links between *MX4* and *MX6*. During normal conditions, the generators connected to *MX6* can generate as much as 5 • 180 = 900 MW while the total load of the local areas does not exceed 100 MW. The excess power in the region flows from *MX6* to *MX4* and from there to the rest of the system. If the two 400 kV transmission links are lost between *MX6* and *MX4*, the heavy load and the large generation areas remain connected through the 115 kV network with the following consequences:

- The transfer impedance between the *MX4* and *MX6* buses increases, causing the machines connected to *MX6* to accelerate. This machine acceleration may lead to rotor angle instability.
- The 115 kV network is overloaded until the line or transformer overload protection operates. When this happens, the areas that encompass the *MX6* and *MX7* buses form a network isolated from the rest of the power system.

For some operating and fault conditions, this double contingency could lead to a blackout at the isolated network in the absence of AGSS control actions. The following simulation results show angle differences between *MX4* and *MX6* for single (loss of one of the 400 kV transmission links) and double (loss of the two 400 kV transmission links) contingencies with maximum generation at *MX4* and *MX6*.

Table 3.2, Figure 3.17, Figure 3.18, and Figure 3.19 show PSS/E™ simulation results for steady-state and transient conditions for single and double contingencies. From the results shown in Table 3.2, the loss of one 400 kV transmission link (Cases 1, 2, and 3) does not cause stability problems (Figure 3.17 shows the angle difference for Case 1). However, if the two 400 kV transmission links are lost (Cases 4, 5, and 6), simultaneously or sequentially, the system becomes unstable because of power transfer limitations on the 115 kV network (Figure 3.18 shows the angle difference for Case 4).

Table 3.2 Simulation results for steady-state and transient conditions on single and double contingencies.

Case	Prefault Angle Diff. δ	Contingency	δ at Line Trip	Comments
1		Single MX4-MX6	6.10°	Max. δ during oscillation 8.7° (see Figure 3.17)
2		Single MX5-MX6	5.25°	Max. δ during oscillation 6.56°
3		Single MX4-MX5	4.11°	Max. δ during oscillation 4.56°
4	3.38°	Double MX4-MX6 and MX5-MX6	14.69°	No AGSS trip, system becomes unstable (see Figure 3.18)
5		Double MX4-MX6 and MX5-MX6	14.69°	AGSS trip generation after 100 ms, δ at AGSS trip 27.28° (see Figure 3.19)
6		Double MX4-MX6 and MX4-MX5	10.72°	AGSS trip generation after 200 ms, δ at AGSS trip 25.55°
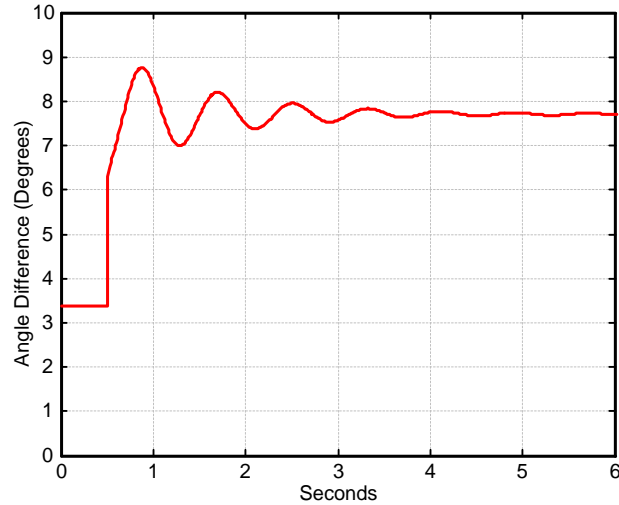
Figure 3.17   Angle difference between *MX6* and *MX4* for a single contingency without AGSS protective action (Case 1).

Figure 3.18 shows the angle difference between *MX6* and *MX4* buses for the simulation of a double contingency and without AGSS remedial action (Case 4). Figure 3.19 shows the angle difference between these buses when the AGSS trips generation 100 ms after the double contingency occurs (Case 5). In this case, the system remains stable with a new steady-state value of δ approximately equal to - 3°. Notice that the power flow reversed a few seconds after the excess generation was disconnected from the network.
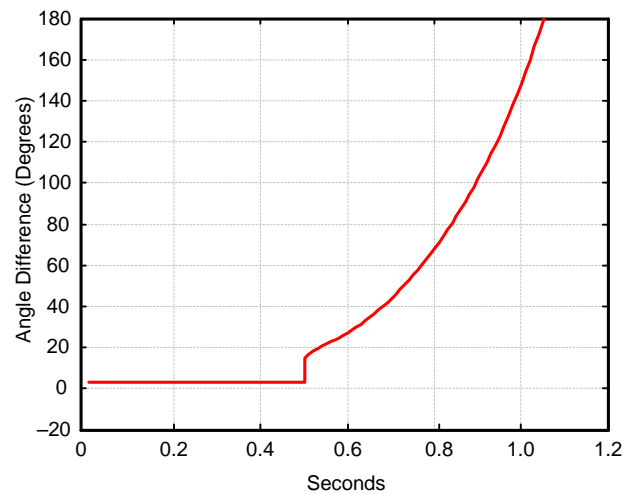
Figure 3.18   Angle difference between *MX6* and *MX4* for a double contingency condition: lines *MX4-MX6* and *MX5-MX6* open without AGSS protective action (Case 4).
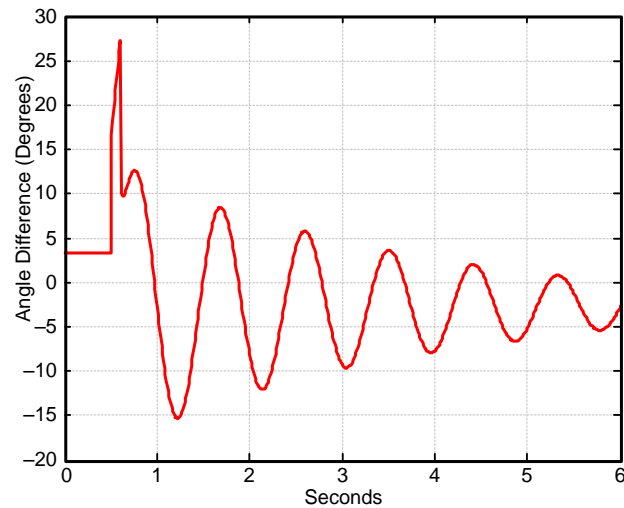
Figure 3.19   Angle difference between *MX6* and *MX4* for a double contingency with AGSS trip after 100 ms (Case 5).

Based on these results and additional field tests, it was determined that an angle difference threshold of 10° can detect double contingencies and will not operate for single contingencies. This threshold could be used in the AGSS to trip part of the generation connected to Bus *MX6*. Two PDC/PMCUs were installed in the field to implement the AGSS and validate the simulation results, as described in the following text.

3.5.3 Performance of the Synchrophasor-Based AGSS

The AGSS under investigation could use the angle-difference information to make trip decisions or be used to supervise existing schemes. In this application, the angle difference changes instantaneously at these buses when one of the 400 kV links is lost. Figure 3.20 shows the logic of the improved angle-difference-based AGSS. With the added angle-difference information, the logic of the scheme is simplified and depends only on one communication channel.
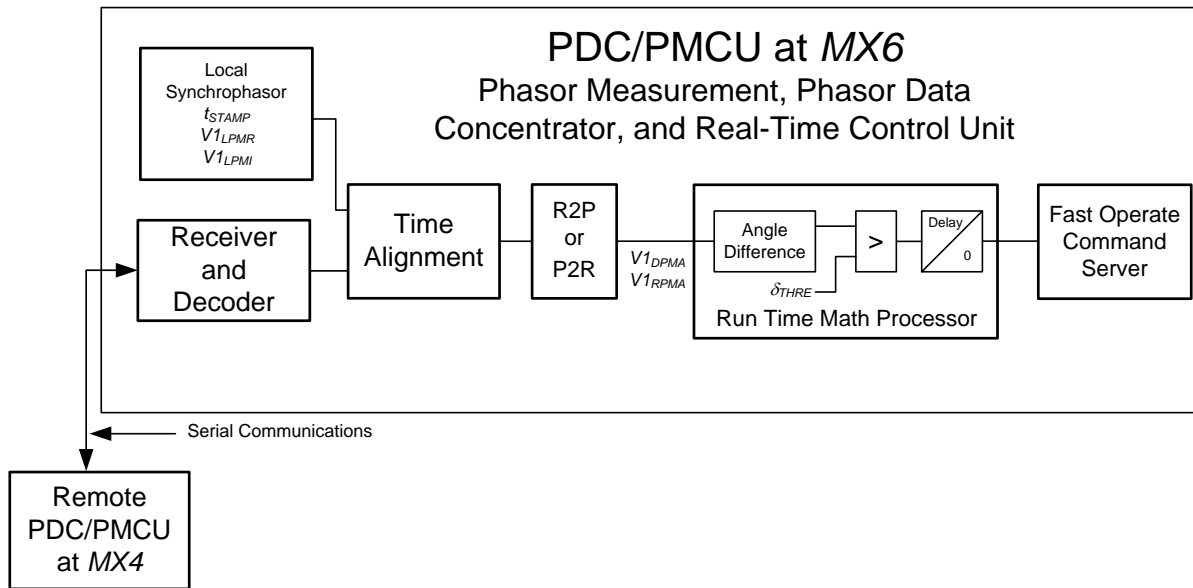
Figure 3.20 AGSS sheds generation at *MX6* based on the positive-sequence voltage angle difference between *MX4* and *MX6*.

The positive-sequence voltage angle difference must be compared against a threshold. If the angle difference indicates that the 400 kV transmission links between buses *MX4* and *MX6* were lost because of a double contingency condition, the scheme sheds generation. An intentional time delay may be included in some applications to avoid tripping generation or arming the AGSS during transient or fault conditions. This application does not require such delay. Subsection 3.4.3 describes implementation details of a synchronized real-time control network that uses the angle difference of positive-sequence voltages at two different locations to detect changes in the topology of the power system.

Based on load flow and stability studies (see Table 3.2), the following was determined:

- Maximum angle difference for conditions where there is no need to shed generation. Contingencies on other links, such as the 115 kV parallel network, should also be considered to ensure that maximum power transfer is achieved.

- Minimum angle difference for conditions where the system requires generation shedding. In this case, *MX4* and *MX6* are connected only through the 115 kV network.

The proposed scheme was installed with continuous remote monitoring to observe the performance of the AGSS and real-time angle difference measurement during different system operating conditions and different contingencies. The measurements were validated with an accurate power system model that includes the following: generator dynamics, power system stabilizers, automatic voltage regulators, governor dynamics, and system loads. The following text describes the results from field testing and modeling.

Two PDC/PMCUs were installed, one at *MX4* and one at *MX6*. Each of the PDC/PMCUs is connected to monitor its corresponding bus voltage and currents from two lines. The PDC/PMCUs were interconnected through a multiplexer with EIA-232 (V.24) asynchronous interface at 19200 bps. Serial Fast Message protocol was used for these tests. Another serial port was connected through a serial-to-Ethernet converter to a remote monitoring system.

The transmission lines *MX4-MX6*, *MX4-MX5*, and *MX5-MX6* were opened and closed under normal system loading conditions. During these open and close operations, synchrophasor measurements were captured at a rate of 20 messages per second. The largest angle difference measurement between *MX4* and *MX6*, for a single contingency, occurred when the line *MX4-MX6* was open at the *MX4* end. Figure 3.21 shows the voltage angle difference between *MX4* and *MX6* for these conditions.
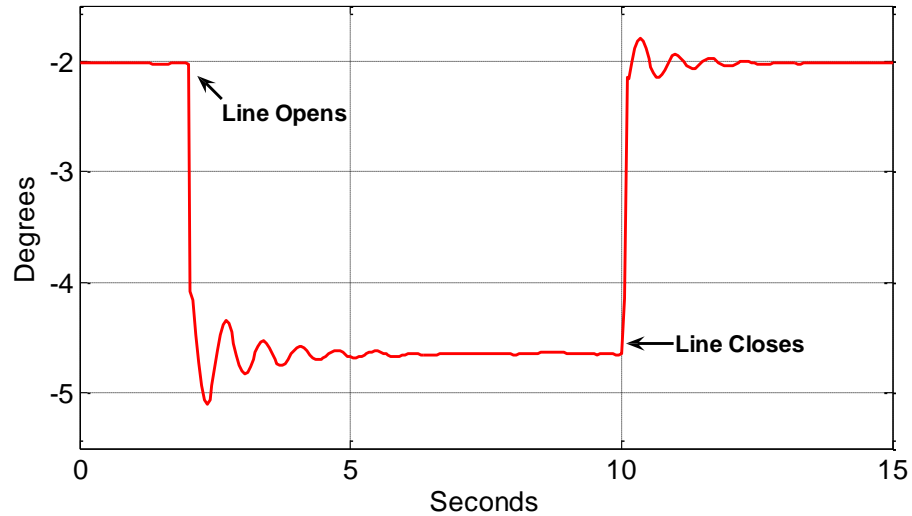
Figure 3.21   Voltage angle difference between the buses *MX4* and *MX6* measured when the line *MX4-MX6* was open and closed at the *MX4* end.

Dynamic system simulations studies were made to emulate the existing system operating conditions during field tests to validate both measurements and system models. Figure 3.22 shows simulation results of the voltage angle difference calculations between buses *MX4* and *MX6* for three cases: *MX4-MX5* open, *MX5-MX6* open, and *MX4-MX6* open. From Table 3.3, we can observe that the *MX4-MX6* open simulation results match the measurements within 0.3°. These results validate the model and the measurements.
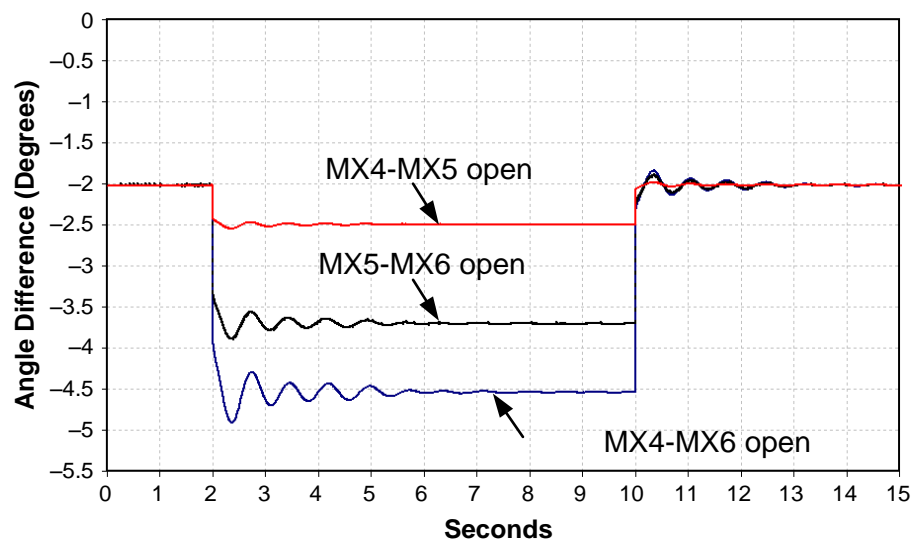
Figure 3.22   Simulation results showing the angle difference between buses *MX4* and *MX6* for three different single contingencies with load and generation conditions similar to the existing conditions during the field tests (see the *MX4-MX6* open case shown in Figure 3.21).

Table 3.3 Simulation results and measurements. Initial conditions and maximum angle difference when line MX4-MX6 opens and closes.

	Steady-State Initial Angle	Maximum Angle During Oscillation
Simulation	- 2.01°	- 4.91°
Measurement	- 2.13°	- 5.20°

Below are additional objectives for performing field tests:

- Test communication-channel performance and communication interfaces.
- Test the logic that calculates angle difference.
- Measure scheme operating times at different angle thresholds.

Four voltage angle-difference elements were programmed to test the angle-difference element logic

and measure scheme operating time. The angle difference thresholds were set to 3°, 4°, 5°, and 10°,

respectively. The oscillographic record, shown in Figure 3.23, was taken directly from the PDC/PMCU

located at *MX6* during the *MX4-MX6* line trip. The oscillogram shows the current flowing through

lines *MX6-MX4* and *MX6-MX5* and bus voltage at *MX6*. Digital channel *FOP01* and *FOP03* are angle

difference elements set to 3° and 4°. They operated within 92 ms. After the initial instantaneous

angle change, the machines at *MX6* accelerate, the angle-difference increases, and the angle

difference element *FOP04* (set to 5°) operates after 292 ms. Notice that for this single contingency

test, the 10° threshold is not exceeded.

IW	*MX6-MX4* Currents
IX	*MX6-MX5* Currents
ROKRPM	Received remote data OK
PMDOKT	Total measurement data OK
FOP01	Angle difference element set to 3°
FOP03	Angle difference element set to 4°
FOP04	Angle difference element set to 5°
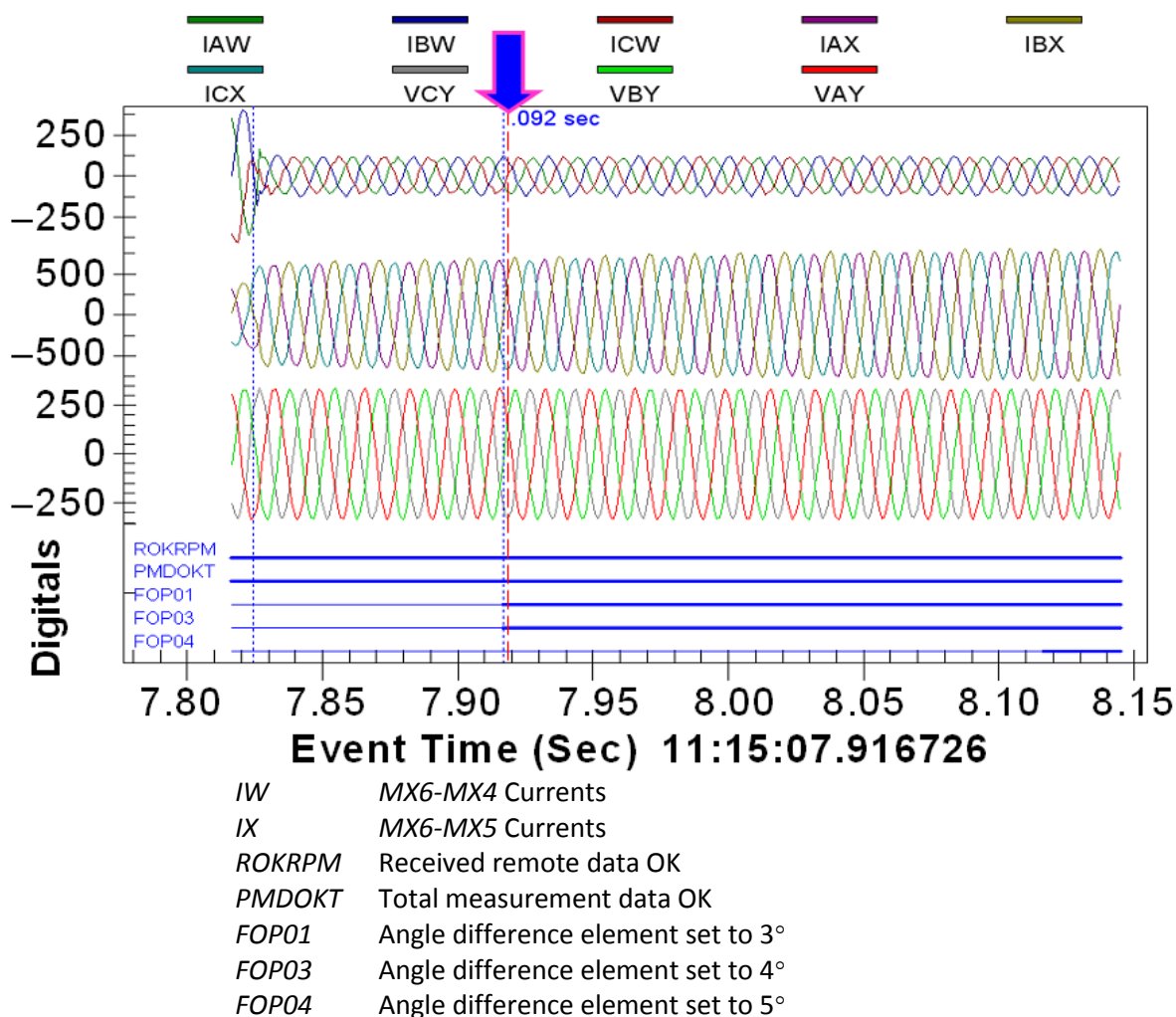
Figure 3.23   Oscillographic record, from the PDC/PMCU located at *MX6*, showing line currents, voltage at *MX6*, and angle difference element operation (currents are in A and voltages in kV).

Table 3.4 summarizes the recorded operating times of the angle difference element set to 3° for the additional trip and close operations.

Table 3.4 Angle difference element operating times for single contingencies.

Line	Operating Condition	Operating Time (ms)
MX4–MX6	Breaker open at MX4	92
MX4-MX6	Breaker open at MX6	82
MX5-MX6	Breaker open at MX6	75

The angle difference element operating time includes the PDC/PMCU measurement delay, communication-channel delay, and the latency because of the message rate. In this case, 20 messages per second introduce a delay of as much as 50 ms. The simulation results described previously (see Table 3.2) showed that a trip time of 200 ms or less is sufficient to avoid stability problems in this area. The angle difference element operating times obtained from the previous field tests are suitable for tripping the excess of generation in less than 200 ms while maintaining system stability.

3.6   Summary

The two main reasons to evaluate the use of positive-sequence voltage angle difference based on synchrophasors from the specific AGSS this chapter presents were its simplicity and the availability of fast communication channels between substations.

The use of PDC/PMCUs reduces operating time and improves the efficiency and reliability of the scheme – the scheme has fewer components – compared to traditional AGSSs based on traditional measurements, separate PLCs, and several remote communication channels.

Synchronized angle-difference calculations provide reliable information to detect network topology changes with minimum communication requirements.

Fast communication channels and available PDC/PMCUs allow the angle-difference-based AGSS to operate in less than 200 ms.

Synchronized measurement message rate affects the AGSS operating time. The message rate of 20 messages per second avoids transient stability problems in the region.

Oscillographic records of angle difference measurements for single line contingencies validate simulation models. The proposed AGSS must operate only when the two transmission links are lost; further studies should consider sequential or simultaneous trips in the transmission and subtransmission networks.

The main challenge of the synchrophasor-based AGSS is its dependence on the timing signal from GPS. Alternative time reference approaches such as redundant terrestrial time distribution signals will improve the dependability of the system.

Chapter 4 Backup Power Line Protection for Ground Faults Using Synchrophasors

4.1   Introduction

Synchrophasors within protective relays have been available since 2002 [35]. Typical applications of this technology are visualization, state measurement, and system integrity protection schemes. This chapter proposes the use of synchrophasors for backup power line protection (BPLP) for ground faults [25]. The proposed protection approach complements protective distance elements and is suitable for single-pole and three-pole tripping applications. This chapter presents the performance of a synchrophasor-based protective element that can be used as a backup protection for challenging fault conditions such as cross-country faults with high fault resistance.

Relays that combine synchrophasor measurements and programmable logic control capabilities could use synchrophasor measurements from both ends of a two-terminal power line to provide BPLP (see Figure 4.1) [26, 53]. The proposed BPLP uses negative- or zero-sequence current elements to detect high fault resistance (R_F) faults. Operating times for these elements depend on the synchrophasor message rate and the synchrophasor filtering process. In the proposed implementation, the sequence component-based BPLP elements detect faults with R_F greater than 300 Ω within 160 ms. The R_F coverage for this current only element compares to that of negative-sequence impedance-based directional elements [55], *67Q*, with the advantage that the proposed elements do not require voltage measurements. The proposed elements include faulted phase identification (*FPI*) logic that makes them suitable for single-pole tripping (*SPT*) applications [56].
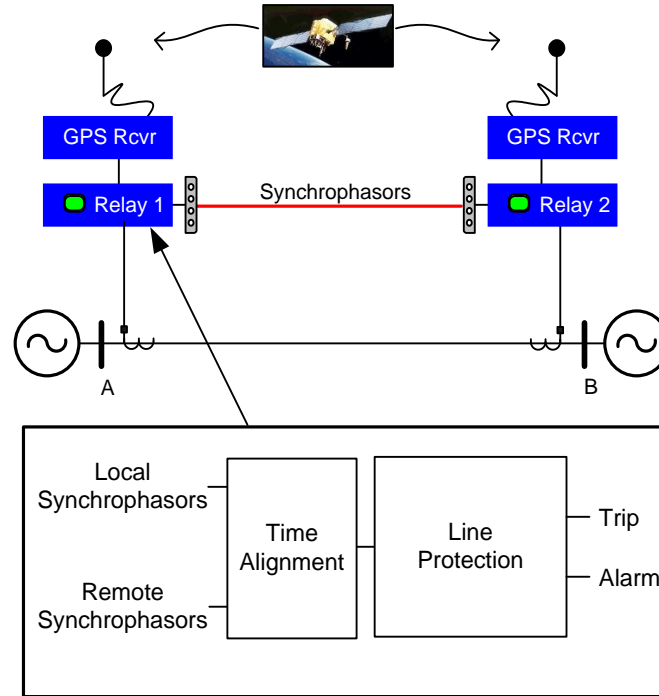
Figure 4.1   Relays exchange synchrophasors for backup power line protection in a two-terminal line application.

4.2   Backup Power Line Protection

Some line protective relays calculate synchrophasors at specific instants (60 times per second, for example) [35]. Communication channels make the local and remote time-stamped currents available to the local and remote relays. These relays time align the local and remote currents on a per phase basis and make them available to protective functions (see Figure 4.2) such as *FPI* logic, negative-sequence current directional element (*32IQ*), zero-sequence current directional element (*32IG*), negative-sequence current differential element (*87LQ*), and zero-sequence current differential element (*87LG*) [25, 57].
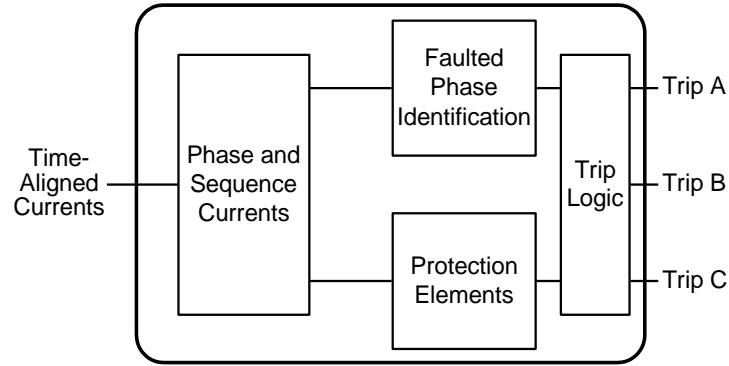
Figure 4.2   Synchrophasor-based protection including phase currents, sequence currents, faulted phase identification logic, protection elements, and trip logic

4.2.1   Faulted Phase Identification (FPI)

The synchrophasor-based protection element includes *FPI* logic that uses the total zero-sequence and total negative-sequence fault currents [56]. The total currents are the sum of the time-aligned local and remote currents. The logic in Figure 4.3 defines sectors *FSA*, *FSB*, and *FSC* (shown in Figure 4.4) that correspond to *A*-phase, *B*-phase, and *C*-phase faults respectively. The logic calculates the angle difference between the sequence fault currents and the relative magnitudes of the total phase-to-phase currents to identify the faulted phase:

A-Phase Fault. The logic asserts the *FSA* bit

$$if \quad -60° < \left(\angle I_0^T - \angle I_2^T \right) \leq 60° \quad and \quad \left| I_{BC}^T \right| \neq \max\left(\left| I_{AB}^T \right| , \left| I_{BC}^T \right| , \left| I_{CA}^T \right| \right) \tag{4.1}$$

B-Phase Fault. The logic asserts the *FSB* bit

$$if \quad 60° < \left(\angle I_0^T - \angle I_2^T \right) \leq 180° \quad and \quad \left| I_{CA}^T \right| \neq \max\left(\left| I_{AB}^T \right| , \left| I_{BC}^T \right| , \left| I_{CA}^T \right| \right) \tag{4.2}$$

C-Phase Fault. The logic asserts the *FSC* bit

$$if \quad -180° < \left(\angle I_0^T - \angle I_2^T \right) \leq -60° \quad and \quad \left| I_{AB}^T \right| \neq \max\left(\left| I_{AB}^T \right| , \left| I_{BC}^T \right| , \left| I_{CA}^T \right| \right) \tag{4.3}$$

where:

I_0^T is the total zero-sequence current phasor,

I_2^T is the total negative-sequence current phasor,

I_{AB}^T is the total *A*-phase minus *B*-phase current phasor,

I_{BC}^T is the total *B*-phase minus *C*-phase current phasor,

I_{CA}^T is the total *C*-phase minus *A*-phase current phasor.

The relay uses the *FPI* logic for tripping the faulted phase in *SPT* applications.
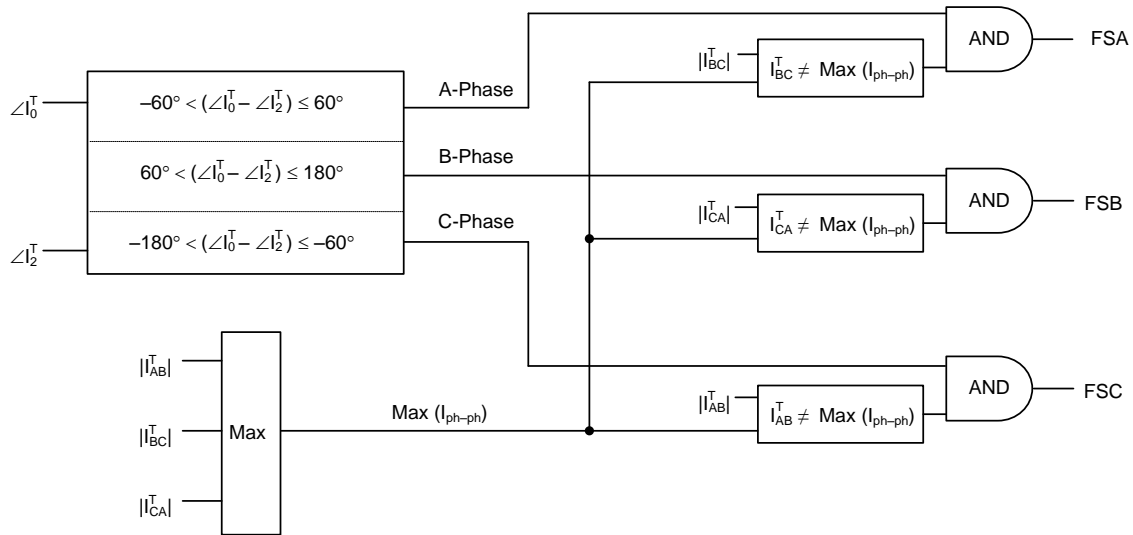
Figure 4.3   Faulted phase identification logic uses total negative-sequence and zero-sequence fault current.
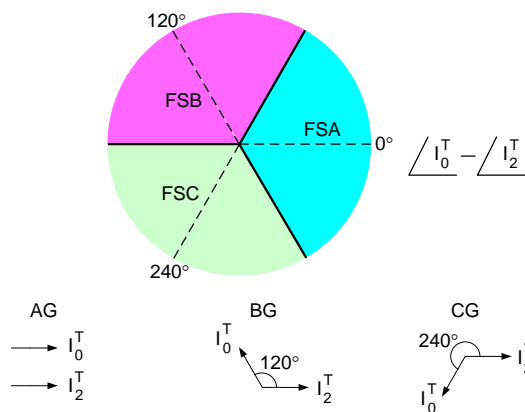
Figure 4.4   The angle difference between I_0^T and I_2^T defines the *FSA*, *FSB*, and *FSC* sectors.

4.2.2   Negative-Sequence Current Directional Element (*32IQ*)

The *32IQ* element compares the angle of the local negative-sequence current I_2^L with the angle of the remote negative-sequence current I_2^R and makes the trip decision according to (4.4). This element detects high-impedance faults when the negative-sequence currents enter the power line at both line ends.

$$\mathrm{Re}\left[I_2^L \bullet \left(I_2^R \right)^* \right] > 0 \qquad (4.4)$$

where:

I_2^L is the local negative-sequence current phasor,

I_2^R is the remote negative-sequence current phasor.

Figure 4.5 shows the basic logic for *32IQ*. The protection enable bit, *PREN*, asserts when $\left| I_2^L \right|$ and $\left| I_2^R \right|$ exceed the element sensitivity threshold, e.g., $0.1 \bullet I_{NOM}$, and when $\left| I_2^L \right|$ is greater than $0.05 \bullet \left| I_1^L \right|$, where I_1^L is the local positive-sequence current phasor. Communication-channel health, data integrity, and time synchronization also supervise this logic. The *32IQ* output asserts when all the previous conditions are valid for two consecutive processing intervals.
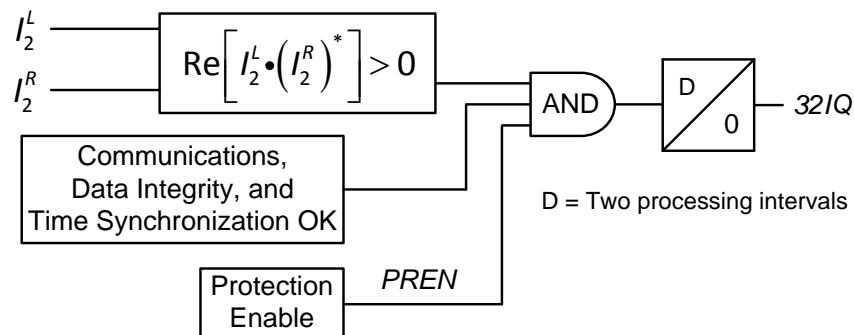
Figure 4.5   Negative-sequence current directional element, *32IQ*, with current magnitude, channel health, data integrity, and time-synchronization supervision.

4.2.3 Negative-Sequence Current Differential Element (*87LQ*)

The *87LQ* element characteristic shown in Figure 4.6 uses operating I_2^{OP} and restraining I_2^{RT} quantities obtained from the local I_2^L and remote I_2^R phasors according to (4.5) and (4.6) [58].

$$I_2^{OP} = \left| I_2^L + I_2^R \right| \tag{4.5}$$

$$I_2^{RT} = \left| I_2^L - I_2^R \right| \tag{4.6}$$

The element operates when the following conditions are met:

$$I_2^{OP} > 87\_Slope \bullet I_2^{RT} \tag{4.7}$$

$$I_2^{OP} > 87PU \tag{4.8}$$

where *87_Slope* is the slope of the *87LQ* element characteristic and *87PU* is the threshold that defines the minimum differential current that the differential element requires to operate. The threshold *87PU* defines the differential element sensitivity.
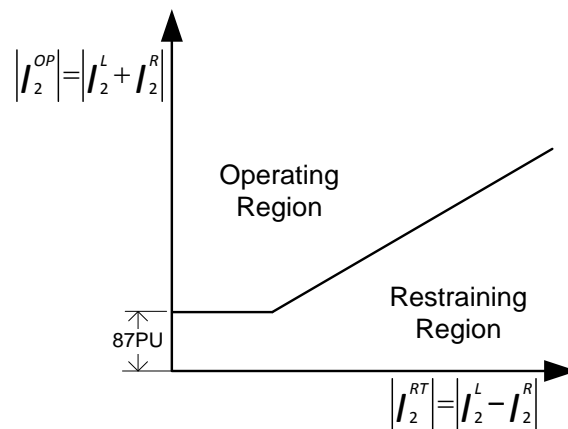
Figure 4.6   Operating characteristic of the 87LQ element.

The relay aligns the local and remote phasors according to their time stamps. Therefore, one advantage of using time-stamped phasors is that channel delay asymmetry does not affect the

element operating and restraining quantities. The *87LG* element operates similarly to *87LQ* but uses zero-sequence quantities instead.

4.3   Protection Element Performance

4.3.1   Fault Resistance Coverage

The *32IQ* and *87LQ* elements overcome the R_F coverage limitations of traditional phase comparison line protection schemes described in [59]. The system in Figure 4.7 is used to determine the R_F coverage of the *67Q* [55], *32IQ* (Figure 4.5), and *87LQ* (Figure 4.6) elements for phase-to-ground faults at different fault locations along the transmission line of the system. The Real-Time Digital Simulator (RTDS®) was used to model this system and simulate faults.

Figure 4.8 illustrates the R_F coverage of the *67Q*, *32IQ*, and *87LQ* elements. For this case, element sensitivities were set to 0.1 • I_{NOM}. The *32IQ* and *87LQ* R_F coverage matches the intersection of the local and remote *67Q* coverage. In a permissive overreaching transfer trip (*POTT*) scheme with forward and reverse elements, the scheme must coordinate forward and reverse *67Q* element sensitivities. The *32IQ* and *87LQ* elements do not have this requirement, so they can be more sensitive than *67Q* elements. Figure 4.9 shows the additional R_F coverage of the *32IQ* and *87LQ* elements with 0.05 • I_{NOM} sensitivity. For example, the proposed element with 0.05 • I_{NOM} sensitivity can detect faults with R_F = 700 Ω for close-in faults, compared to the 350 Ω seen by the *67Q* element.

500∠11° kV   500∠0° kV

$Z_{L1} = 44.98\angle86°$ Ω

$Z_{S1} = 35.97\angle88°$ Ω $Z_{L0} = 165.75\angle81°$ Ω $Z_{R1} = 17.98\angle88°$ Ω

$Z_{S0} = 71.94\angle88°$ Ω $Z_{R0} = 35.97\angle88°$ Ω
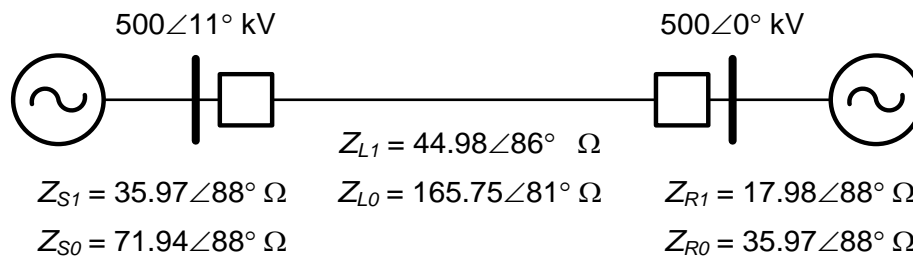
All impedances are in primary ohms

Figure 4.7   Power system parameters and operating conditions to analyze R_F coverage capabilities of the *32IQ*, *87LQ*, and *67Q* elements.
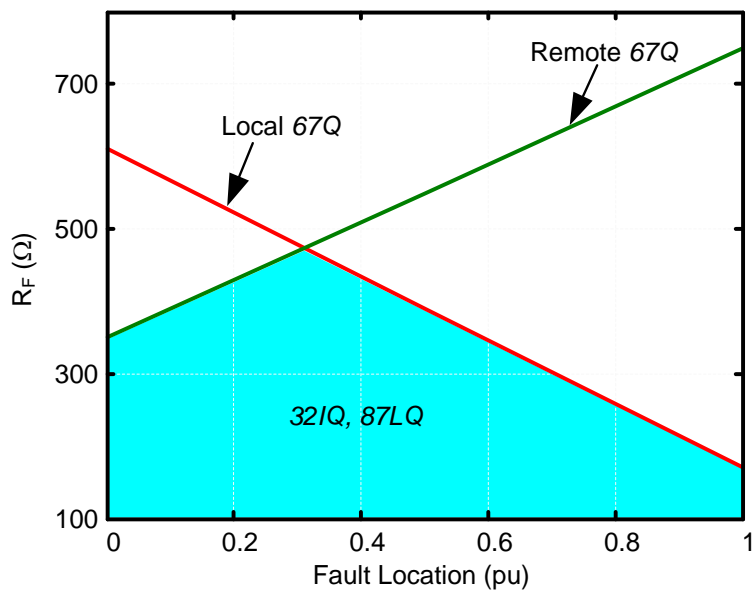
Figure 4.8 R_F coverage of the *32IQ*, *87LQ,* and *67Q* elements for phase-to-ground faults at different line locations. The shaded region illustrates the R_F coverage of the *32IQ* (Figure 4.5) and *87LQ* (Figure 4.6) elements. This region also corresponds to the R_F coverage of the *67Q* elements in a POTT scheme.
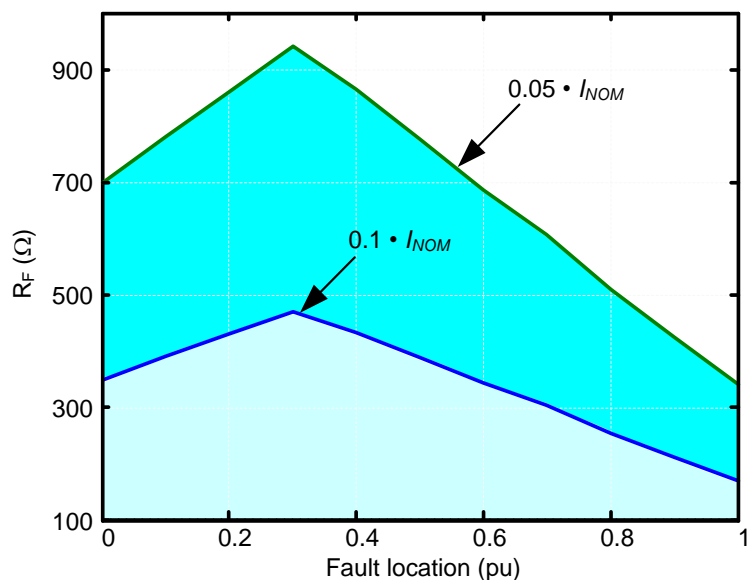
Figure 4.9 R_F coverage of the *32IQ* and *87LQ* elements with 0.05 • I_{NOM} and 0.1 • I_{NOM} sensitivity. The area between the 0.1 • I_{NOM} and the 0.5 • I_{NOM} lines corresponds to the additional R_F coverage of the *32IQ* (Figure 4.5) and *87LQ* (Figure 4.6) elements with 0.05 • I_{NOM} sensitivity.

4.3.2   Operating Time of the *32IQ* Element

The operating time of the synchrophasors-based directional elements described previously depends on the synchrophasor message rate, the synchrophasor filtering process, and element sensitivity. Figure 4.10 shows the *32IQ* element operating time for an *A*-phase-to-ground-fault with R_F = 450 Ω located 30 percent from the local end (left) for the system in Figure 4.7. The local and remote relays operate in 165 ms and 158 ms, respectively. These operating times are slower than the operating times of traditional directional and differential elements, which operate within one power system cycle. The advantage of the proposed elements is their improved R_F coverage – as the aqua blue area in Figure 4.9 illustrates. In this application, the relays exchange synchrophasors at 20 messages per second, and the filtering system attenuates harmonics according to IEEE Std C37.118.1 [23]. The element sensitivities were set to 0.1 • I_{NOM}. The relays exchange *IA*, *IB*, and *IC* synchrophasors along with their corresponding synchronized time stamps through the use of peer-to-peer relay communications [60] at 38400 bps. A faster message rate reduces the operating time linearly and the filtering process reduces element operating time according to the filter step response as depicted in Figure 2.13.
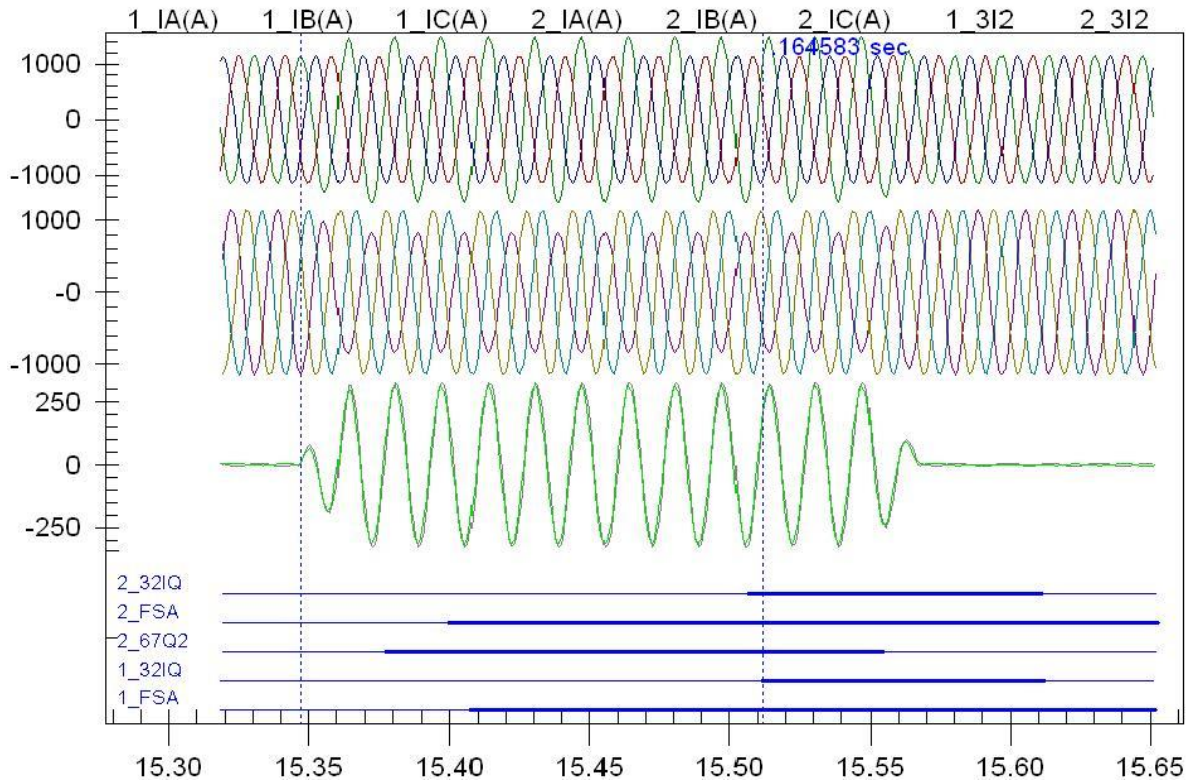
Figure 4.10 Operating times of the *FPI*, *32IQ*, and *67Q* elements for an *A*-phase-to-ground fault
located 30 percent from the local end. The prefixes 1 and 2 of the digital elements
correspond to the local and remote relays, respectively.

4.3.3   Effect of Standing Unbalance and Line Loading

Standing negative-sequence current reduces *32IQ* R_F coverage [61]. First, consider an

A-phase-to-ground fault with R_F = 350 Ω located 80 percent from the local end (left) on one of the

parallel lines of the system in Figure 4.11 during balanced prefault system operating conditions. The

prefault negative-sequence current unbalance is zero (see Table 4.1). Figure 4.12 shows the local

and remote negative-sequence current phasors for this fault. The angle difference between these

phasors is 5°. The *32IQ* element operates correctly for this fault.

Table 4.1   Local and remote negative-sequence currents for an *A*-phase-to-ground fault with balanced prefault conditions.

Current	I_2^L (Primary Amps)	I_2^R (Primary Amps)
Prefault	0	0
Fault	$57\angle 0°$	$92\angle -5°$

$500\angle 0° \text{ kV}$ $Z_{L1} = 38.40\angle 86° \Omega$ $515\angle 4° \text{ kV}$
$Z_{L0} = 146.90\angle 81° \Omega$

$Z_{S1} = 35.97\angle 88° \Omega$ $Z_{L1} = 38.40\angle 86° \Omega$ $Z_{R1} = 17.98\angle 88° \Omega$
$Z_{S0} = 71.94\angle 88° \Omega$ $Z_{L0} = 146.90\angle 81° \Omega$ $Z_{R0} = 35.97\angle 88° \Omega$

All impedances are in primary ohms
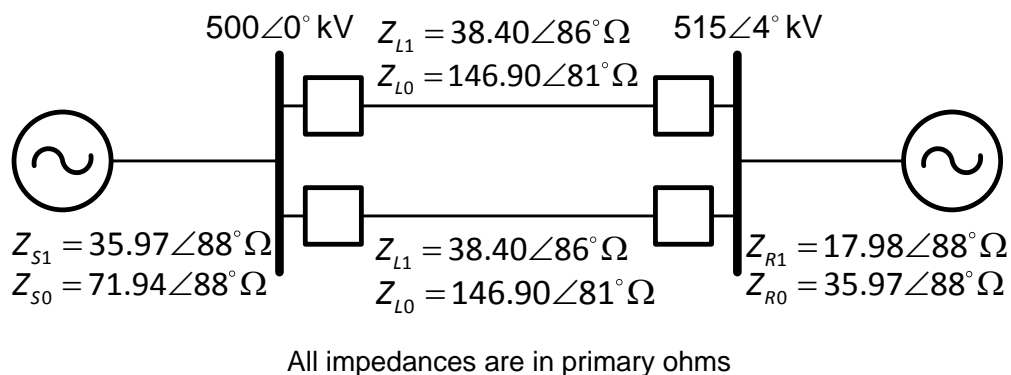
Figure 4.11   Power system parameters and operating conditions to analyze *32IQ* and *87LQ* element performance for balanced and unbalanced prefault operating conditions.
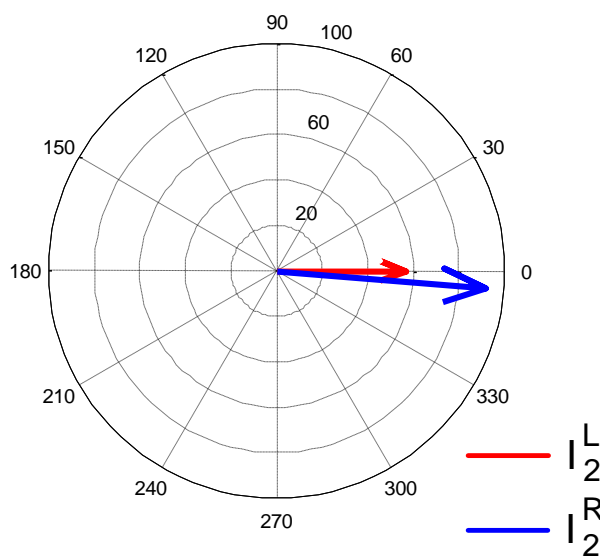
Figure 4.12   Local and remote negative-sequence currents for an *A*-phase-to-ground fault located 80 percent from the local end on one of the parallel lines with balanced prefault conditions.

Next, the same fault is applied while the *A*-phase of the parallel line is open. Table 4.2 shows the prefault and fault local and remote negative-sequence currents. The phasor diagram in Figure 4.13 illustrates the load component and the fault without load component together with the fault current at the local and remote terminals for this network configuration. Note that the angle difference between the local and remote fault currents is 108°. This angle difference increases as the load current increases. The *32IQ* element does not detect this fault. This element has decreased sensitivity because of the increase in load current for this unbalanced operating condition. This unbalanced network poses a challenge to the *32IQ* element. The next subsection shows that *87LQ* and *67Q* have greater sensitivity than *32IQ* for cross-country faults.

Table 4.2   Local and remote negative-sequence currents for an *A*-phase-to-ground fault with unbalanced prefault conditions.

Current	I_2^L (Primary Amps)	I_2^R (Primary Amps)
Prefault	$79 \angle 61°$	$78 \angle -119°$
Fault	$37 \angle 0°$	$154 \angle -108°$
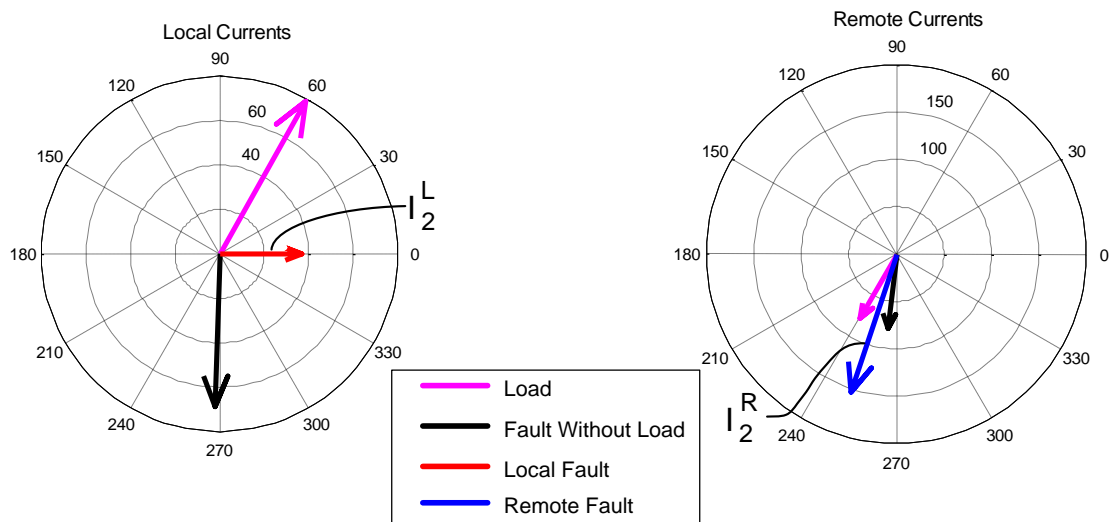
Figure 4.13   Local and remote negative-sequence currents for an *A*-phase-to-ground fault located 80 percent from the local end on one of the parallel lines with unbalanced prefault conditions.

4.3.4   Cross-Country Faults (CCFs)

Cross-country faults occur when there are two simultaneous single-phase-to-ground faults at two different locations of the power system. Cross-country faults and high R_F present another challenge to line protection. Figure 4.14 shows the operating times of the local and remote relays for a CCF. The fault starts as an *A*-phase-to-ground fault located 80 percent from the local terminal of the parallel line of the system in Figure 4.11. After 8 ms, a *C*-phase-to-ground fault occurs on the protected line located 80 percent from the local relay. In the first case, R_F equals 250 Ω for both faults. The *67Q* elements, *FPI* logic, and *32IQ* elements correctly detect the fault in 18 ms, 75 ms, and 125 ms, respectively, as Figure 4.14 illustrates.
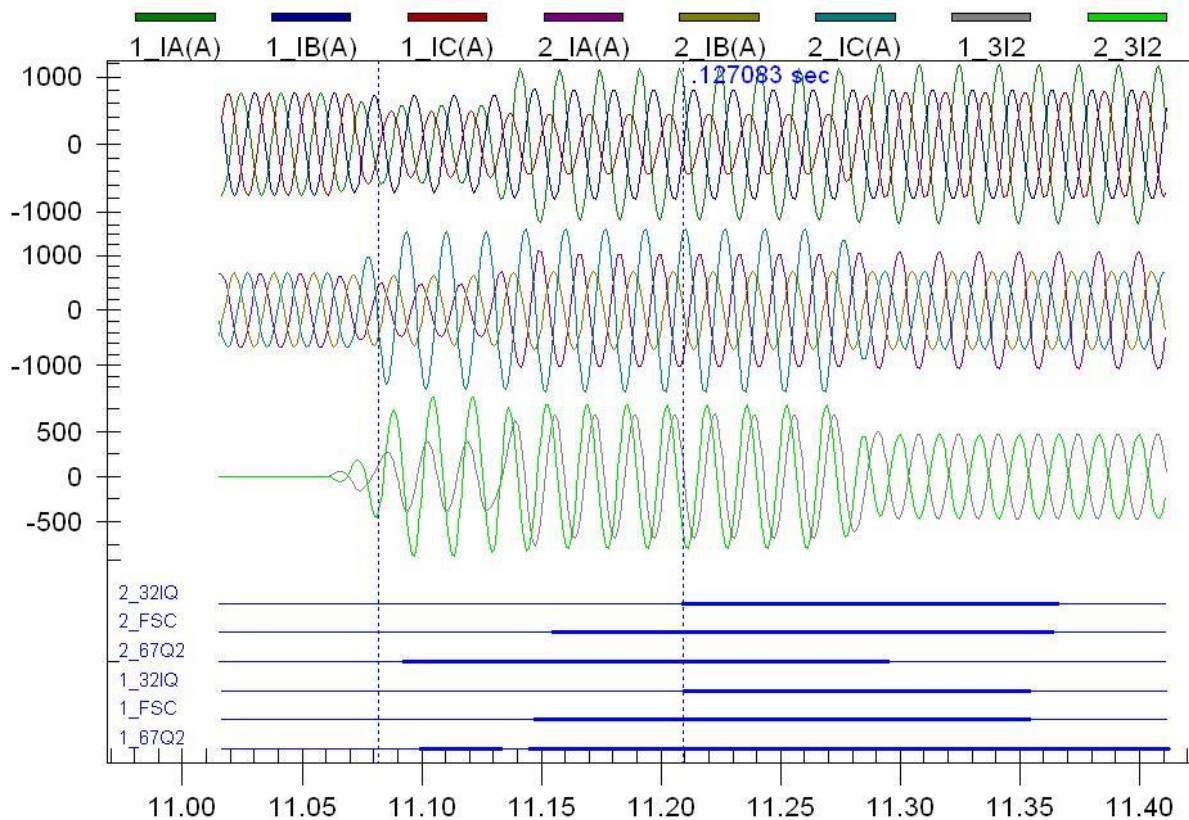
Figure 4.14   Operating times of the *FPI*, *32IQ*, and *67Q* elements for a CCF. First, an *A*-phase-to-ground fault occurs on the parallel line. After 8 ms, a *C*-phase-to-ground fault occurs on the protected line. R_F equals 250 Ω for both faults.

In the second case, R_F is increased to 450 Ω for both faults. The *32IQ* elements do not operate for this fault because of the first unbalanced fault. For this reason, the *32IQ* elements do not appear in

Figure 4.15. Table 4.3 shows the operating times of the *67Q*, *FPI*, and *87LQ* local and remote

elements. For this case *87_Slope* = 0.2.

Table 4.3   Operating times of *67Q*, *FPI*, and *87LQ* elements with R_F equal to 450 Ω.

Current	Local (ms)	Remote (ms)
67Q	83	23
FPI	96	94
87LQ	148	158

Notice that for both CCF*s* the total current *FPI* logic provides reliable phase selection information.

The *67Q* elements combine with the *FPI* logic to trip the correct phase in *SPT* applications. These test

cases demonstrate that the *87LQ* and *67Q* elements provide better R_F coverage than the *32IQ*

element for unbalanced prefault conditions.
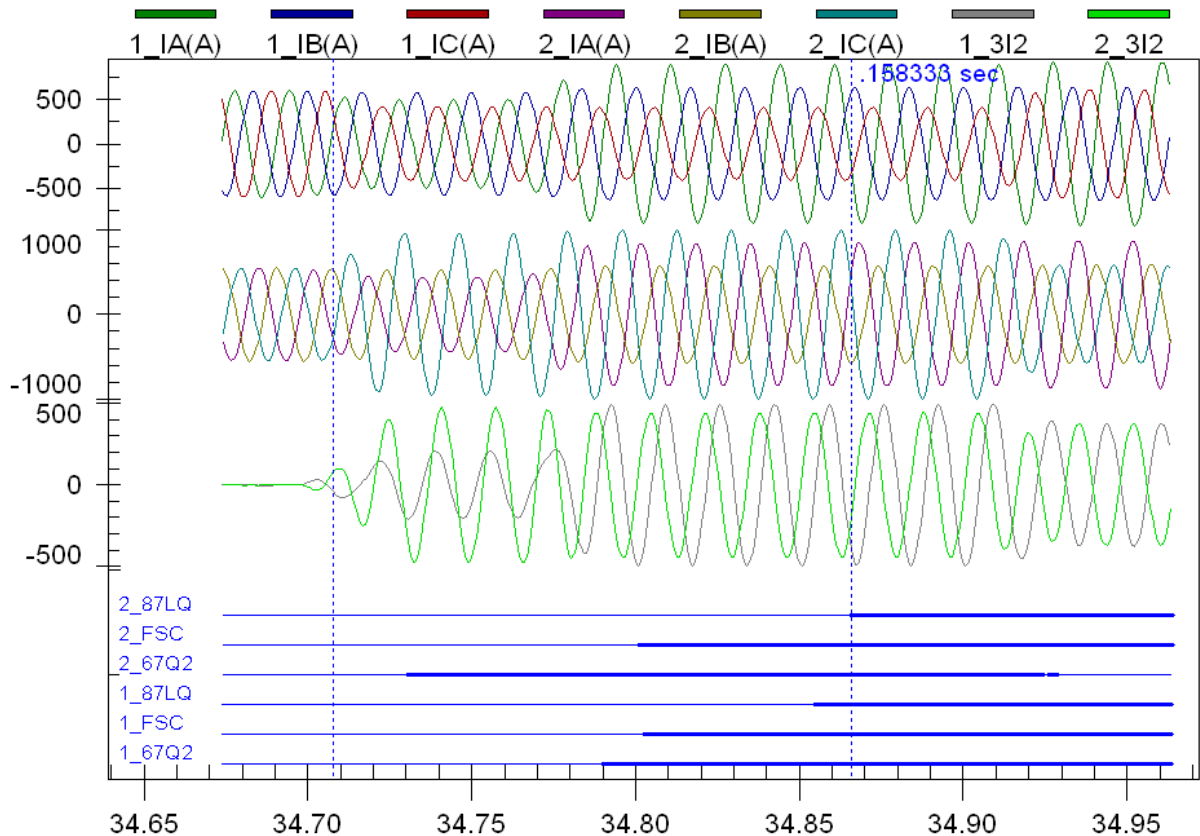
Figure 4.15   Operating times of the *FPI*, *87LQ*, and *67Q* elements for a CCF. First, an
A-phase-to-ground fault occurs on the parallel line. After 8 ms, a *C*-phase-to-ground
fault occurs on the protected line. R_F equals 450 Ω for both faults.

Figure 4.16 shows the operating characteristics of the *87LQ* and *32IQ* elements in the current-ratio complex plane [58]. For these elements, the complex plane variable is the ratio of the remote I_2^R phasor to the local I_2^L phasor. The plots in this figure show that the restraining region of the *32IQ* element is greater than the restraining region of the *87LQ* element. The remaining area of the plane corresponds to the operating region.
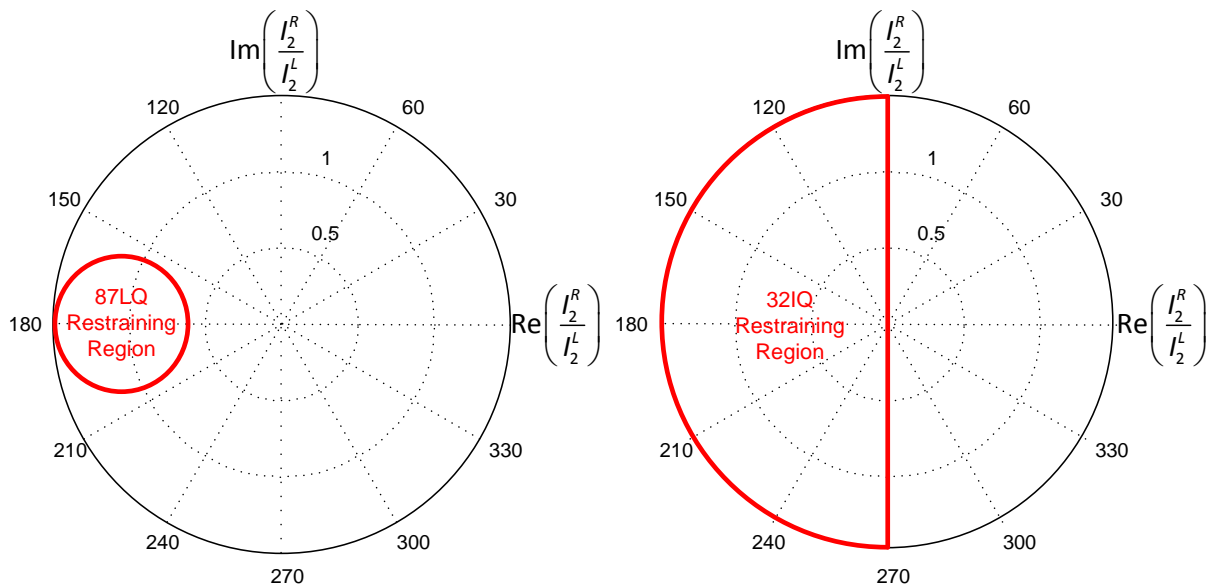
Figure 4.16   The restraining region of the *32IQ* is greater than the restraining region of the *87LQ*; the *87LQ* has better R_F coverage than the *32IQ*.

4.4   Summary

Synchrophasor-based protection complements primary distance protection schemes, provides backup protection, and does not require voltage information. The latter capability allows the relay to protect the line during loss-of-potential conditions, which block the primary distance and directional element based-protection.

Negative-sequence current directional and differential elements together with total current faulted phase identification detect high-resistance faults without compromising phase selectivity. These elements have minimum communication bandwidth requirements.

The proposed negative-sequence current differential element *87LQ* outperforms the proposed negative-sequence directional element *32IQ* and the traditional negative-sequence impedance-based directional element *67Q*. The proposed *87LQ* provides sensitive protection even during unbalanced prefault conditions.

Based on the simulation results this chapter presented, the recommended scheme for backup power line protection for ground faults through the use of synchrophasors consists of the faulted phase identification logic that uses time-synchronized total negative-sequence and total zero-sequence fault currents – shown in Figure 4.3 – and the 87LQ element that uses local and remote time-synchronized currents with the operating characteristic shown in Figure 4.6.

An additional important benefit of the proposed approach is that because of the use of time-stamped, time-synchronized measurements, communication-channel delay asymmetry does not affect the operating and restraint quantities of the synchrophasor-based current differential element.

Chapter 5 Out-of-Step and Power Swing Detection Using Synchrophasors

5.1 Introduction

Traditional out-of-step and power swing detection devices use voltage and current measurements that these devices acquire at a particular power system location by using only local information. The Clarke Diagram [62] in Figure 5.1, shows the positive-sequence apparent impedance, Z_λ, in a two-machine system for $|E_A/E_B|$ = 1.1 and δ = 70°. The diagram also shows the trajectory of Z_λ on the impedance plane for $|E_A/E_B|$ = 1.1 for multiple values of δ. This voltage ratio and the impedance between the A and B sources define the impedance trajectory of the operating point. E_A and E_B are the electromotive forces of the two machines, and δ is the angle between E_A and E_B.
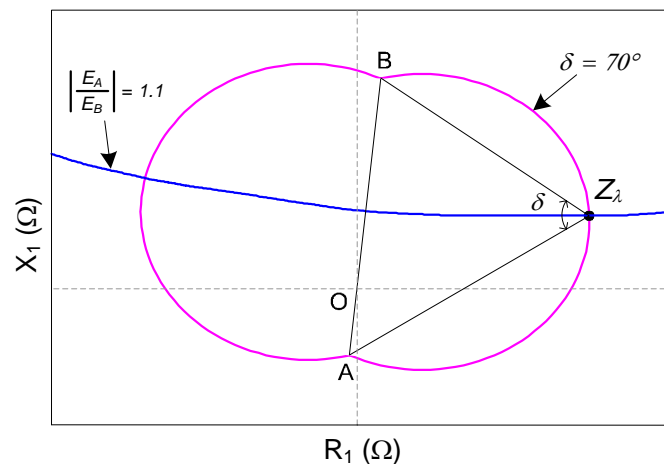
Figure 5.1   Load impedance trajectory on the impedance plane for *$|E_A/E_B|$ = 1.1*.

Out-of-step (OOS) detection is a key function of distance protective relays for blocking their operation during power swings. During power swings it is desirable to detect these oscillation conditions and separate the power system network in a controlled manner to create islands with balanced generation and load. Typically, OOS detection methods are implemented in distance relays by using methods that rely on local voltages and currents. These relays measure the positive-sequence apparent impedance, Z_λ, and compare it against two concentric static impedance-based characteristics [63]. The relays detect an OOS condition if Z_λ stays inside the outer characteristic and outside the inner characteristic longer than a preset time; when this condition is

detected, the distance element is blocked to prevent a potential misoperation. These OOS characteristics are also used to detect unstable swings and send trip commands to strategic locations through a communication network to create system islands with balanced generation and load.

The power swing relay described in [17] uses a power swing detection (PSD) method in which the relay measures the local positive-sequence voltage and current and estimates the positive-sequence voltage at the remote line end. Using the local measured and the remote estimated voltage phasors, the relay calculates the angle difference δ between the phasors and then calculates the first and second derivatives of δ with respect to time for identifying unstable swing conditions. Notice that to estimate the voltage at the remote end, the PSD algorithm needs network parameter and network topology information.

One of the main advantages of using synchrophasor-based algorithms for PSD is that they require minimum network parameter or topology information. References [5, 19, 20] propose to use synchrophasors for estimating rotor angle differences across the power system and determining the stability of the power swing by implementing the equal area criterion in real time. Another approach for preventing power system total collapse uses voltage angle differences between generator groups to predict unstable power swing conditions and take remedial actions to split the power system before the unstable operating conditions occur [18].

This chapter proposes a method that uses voltage synchrophasor information from two areas of the power system network to calculate δ, then calculates the slip frequency (first derivative of δ with respect to time) and acceleration (second derivative of δ with respect to time) to identify OOS and power swing conditions [26, 27, 28, 29]. This chapter discusses the application of this method for the following:

- Detection of OOS conditions.
- Detection of power swings.
- Prediction of unstable out-of-step conditions.
- Activation of remedial actions to prevent power system instability.

5.2 Power System Electromechanical Oscillations

Synchronous machines must adapt to different operating conditions when exchanging active power across a power system. The machines accelerate or decelerate to adapt to changing power transfer requirements that occur during system disturbances. Power system dynamics involve the electrical properties, as well as the mechanical properties, of the electrical machines in the power system [64]. For the purpose of this analysis, a two-pole synchronous machine is assumed where the mechanical and electrical degrees are equal.

The difference between the shaft torque T_m and the electromagnetic torque T_e in a machine (see Figure 5.2) determines the accelerating torque T_a (5.1). In generators, $T_a > 0$ accelerates the machine.

$$T_a = T_m - T_e \tag{5.1}$$
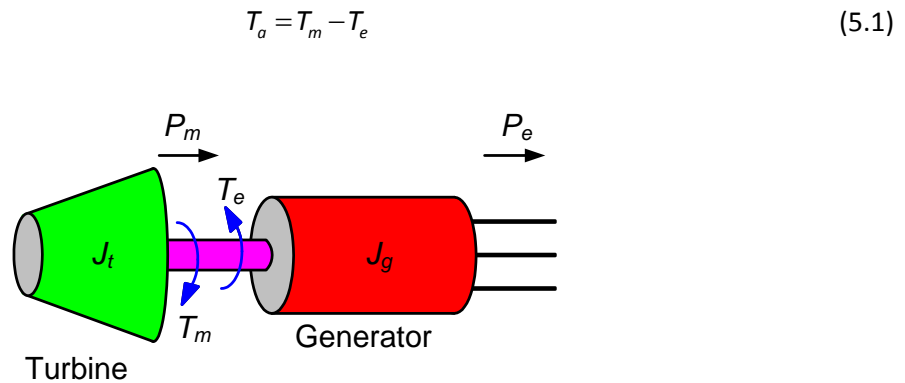
Figure 5.2   Generator connected to a power system network.

The active power P can be represented as a function of the torque T according to (5.2).

$$P = T\omega \tag{5.2}$$

where T is the torque in *N-m* and ω is the angular velocity in *rad/s*.

The change of the angular rotor position θ with respect to time determines the angular velocity ω (5.3).

$$\omega = \frac{d\theta}{dt} \tag{5.3}$$

The torque T is a function of the moment of inertia J and the angular acceleration α, according to (5.4).

$$T = J\,\alpha = J\frac{d\omega}{dt} \tag{5.4}$$

where J is the rotor moment of inertia in $kg\text{-}m^2$ and the angular acceleration α is the change of the angular velocity with respect to time in rad/s^2.

The angular momentum M (5.5) is a function of the moment of inertia J and the angular velocity ω.

$$M = J\,\omega \tag{5.5}$$

where M is the angular momentum in $kg\text{-}m^2/s$. The accelerating power P_a can be represented as a function of the angular acceleration α and as a function of the angular rotor position θ (5.6).

$$P_a = T_a\,\omega = M\,\alpha = M\frac{d^2\theta}{dt^2} \tag{5.6}$$

Figure 5.3 illustrates the rotor angle position $\theta(t)$ with respect to a synchronous reference frame that rotates at the synchronous speed ω_{syn}. The angular rotor position $\theta(t)$ is equal to the phase angle resulting from the synchronous rotating reference $\omega_{syn}t$ plus the angular displacement from the synchronous rotating reference, $\pi/2 + \delta$, as shown in (5.7).

$$\theta(t) = \omega_{syn}t + \frac{\pi}{2} + \delta \tag{5.7}$$
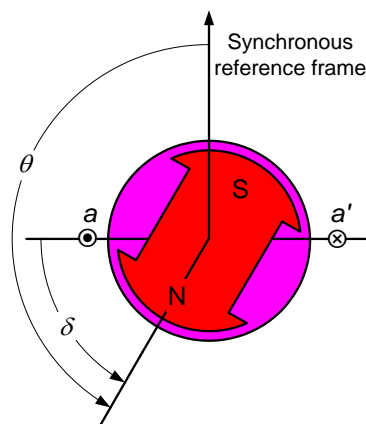
Figure 5.3   Rotor position with respect to a synchronous reference frame.

The machine angular velocity ω is the derivative of the angular rotor position with respect to time θ (t) (5.8).

$$\omega = \frac{d\theta}{dt} = \omega_{syn} + \frac{d\delta}{dt} \tag{5.8}$$

Taking the derivative of the angular velocity with respect to time, (5.6) can be expressed as a function of δ (5.9).

$$P_a = M \frac{d^2\delta}{dt^2} \tag{5.9}$$

P_a (5.9) can be represented as a function of the constant H, with power expressed in per unit by using (5.10).

$$P_a = P_m - P_e = \frac{2H}{\omega_{syn}} \cdot \frac{d^2\delta}{dt^2} = \frac{2H}{\omega_{syn}} \cdot \frac{d\omega}{dt} \tag{5.10}$$

where P_m is the mechanical power supplied to the generator in pu, P_e is the electrical power supplied to the system in pu, and H is the constant of inertia in seconds. Equation (5.10) is known as the swing equation; one swing equation per machine is necessary to model the network dynamics. The angular displacements δ of the machines in a system provide information about the power system dynamics. The solution of the system power swing equations determines how δ changes as a function of time for each machine, and changes in δ provide information about the stability of the power system.

5.3 Out-of-Step and Power Swing Detection Scheme in a Two-Area Power System

In a two-area system, the power system electrical center is the point that corresponds to half of the total impedance between the two sources [50]. The electrical center can be at a point on a transmission line or at any other part of the power system that corresponds to half of the total impedance. The proposed algorithms in the next sections require that the system electrical center be between the phasor measurement and control units (PMCUs) that acquire the synchrophasor

measurements [35]. PMCUs that include programmable logic capabilities allow the implementation of real-time power swing detection algorithms with a minimum of components [26]. The maximum transfer message rate at which the PMCUs described in [26] exchange synchrophasors is 20 messages per second. There are wide-area control applications that require higher message rates for achieving faster operating times and wider frequency bandwidth, e.g. *60* messages per second. For example, the proposed approach, shown in Figure 5.4, uses a synchrophasor processing unit (SPU) [27] that collects synchrophasor data from PMCUs at 60 messages per second. Notice that PMCUs are located close to the generating units; this PMCU placement ensures that the swing center is between the two PMCUs. In this approach, the SPU performs all the calculations for power swing detection in real time and sends remedial action commands to the PMCUs. These remedial actions prevent the occurrence of unstable power swing operating conditions in any part of the power system.
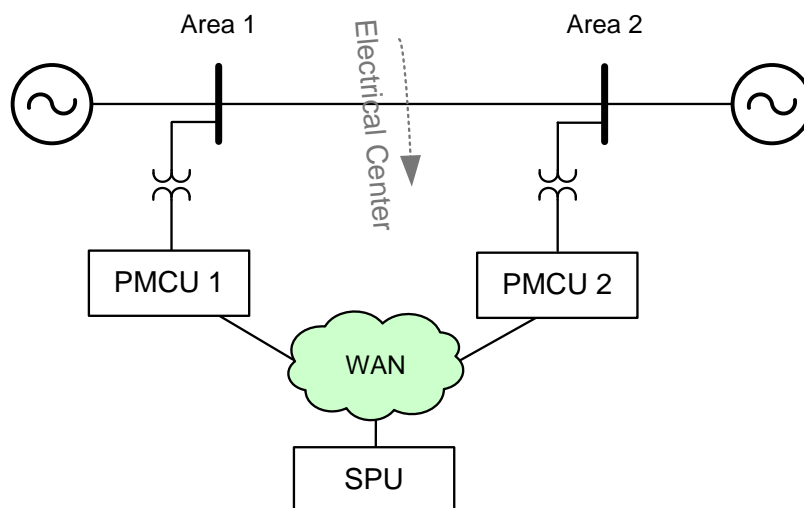
Figure 5.4   Detection scheme suitable for two-area power systems that uses two PMCUs and one SPU for power swing detection.

5.4   Out-of-Step Detection

OOS conditions such as machine pole slip can be detected by using the angle difference of the voltage measurements obtained from the two-area system depicted in Figure 5.4. An out-of-step detection element (OOSD), with logic as shown in Figure 5.5, detects when the angle difference of the machines in one area with respect to the machines in the other area exceeds 180°. Such an angle difference is an indication of an OOS event. The OOSD element calculates the angle difference

δ_k according to (5.11). The OOSD algorithm enables the angle difference calculation when both of the following operating conditions exist:

- The positive-sequence voltage magnitude $\vec{V}_{1\_Mag\,k}^{PMCU1}$ measured by PMCU 1 is greater than 1 V secondary.

- The positive-sequence voltage magnitude $\vec{V}_{1\_Mag\,k}^{PMCU2}$ measured by PMCU 2 is greater than 1 V secondary.

$$\delta_k = \vec{V}_{1\_Ang\,k}^{PMCU1} - \vec{V}_{1\_Ang\,k}^{PMCU2} \tag{5.11}$$

where:

$\vec{V}_{1\_Ang\,k}^{PMCU1}$ is the positive-sequence voltage angle measured by PMCU 1 at the k processing instant,

$\vec{V}_{1\_Ang\,k}^{PMCU2}$ is the positive-sequence voltage angle measured by PMCU 2 at the k processing instant.

The OOSD logic compares δ_k and its absolute value with the OOS threshold, *OOSTH*; this threshold defines the angle difference operating region (ADOR) in the angle difference plane shown in Figure 5.6. The logic monitors whether the angle difference operating point (ADOP) crosses this region. When the ADOP crosses the ADOR region, the logic asserts the *OOSD* bit to indicate the occurrence of an OOS event. Note that ADOP can cross this region from the right or from the left of the angle difference plane. The *OOSD* bit feeds the OOS counter to track the number of OOS events (*OOSCN*) for monitoring purposes.
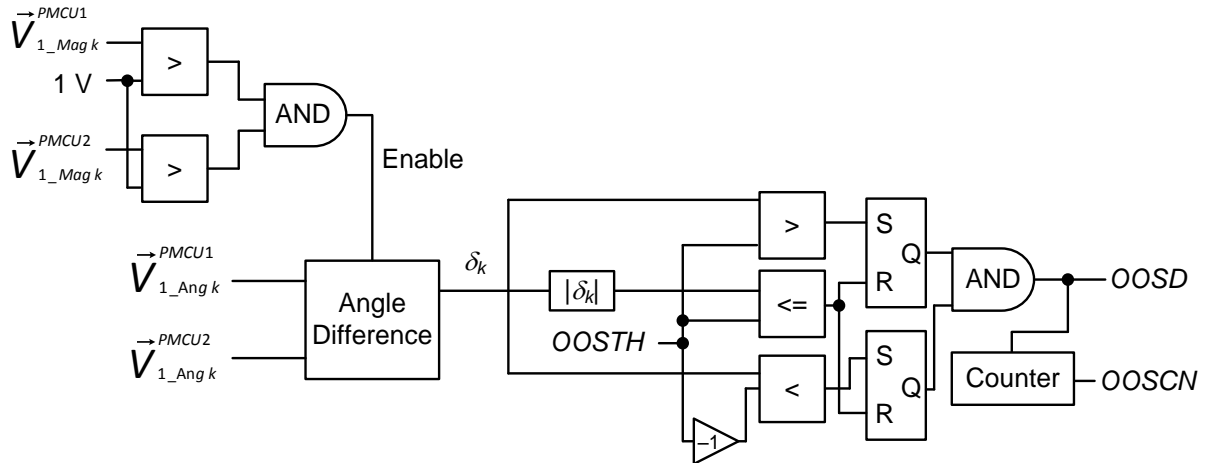
Figure 5.5   OOSD logic uses angle difference information to identify OOS conditions.
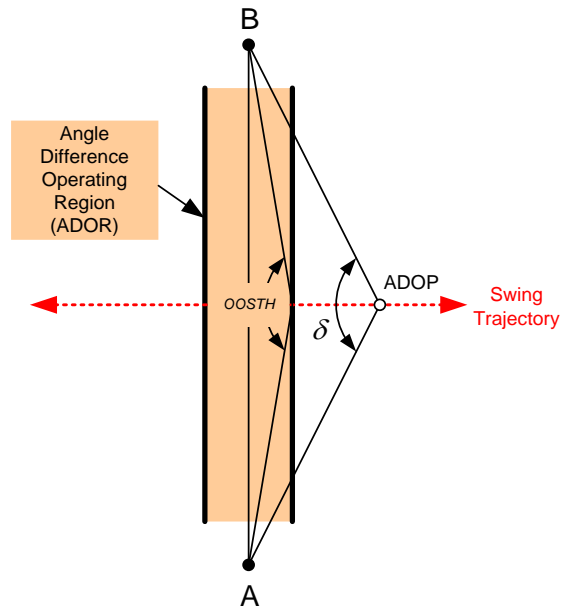
Figure 5.6   Operating characteristic of the OOSD element.

5.5   Power Swing Detection

The PSD algorithm uses the positive-sequence voltage synchrophasors that the PMCUs acquire at two power system buses to calculate the angle difference δ_k between these voltages according to (5.11). The change of δ_k with respect to time defines the slip frequency S_k, given by (5.12), and the change of slip frequency with respect to time defines the acceleration A_k, given by (5.13). The SPU runs the PSD algorithm and calculates the absolute values of S_k and A_k at fixed time instances

according to the synchrophasor message rate. Figure 5.7 shows the block diagram of the PSD algorithm.

$$S_k = \frac{(\delta_k - \delta_{k-1})}{360\,(t_k - t_{k-1})} \qquad (5.12)$$

$$A_k = \frac{S_k - S_{k-1}}{t_k - t_{k-1}} \qquad (5.13)$$

where:

S_k is the slip frequency at the k processing instant,

A_k is the acceleration at the k processing instant,

$t_k - t_{k-1}$ is the interval time between consecutive synchrophasor measurements.
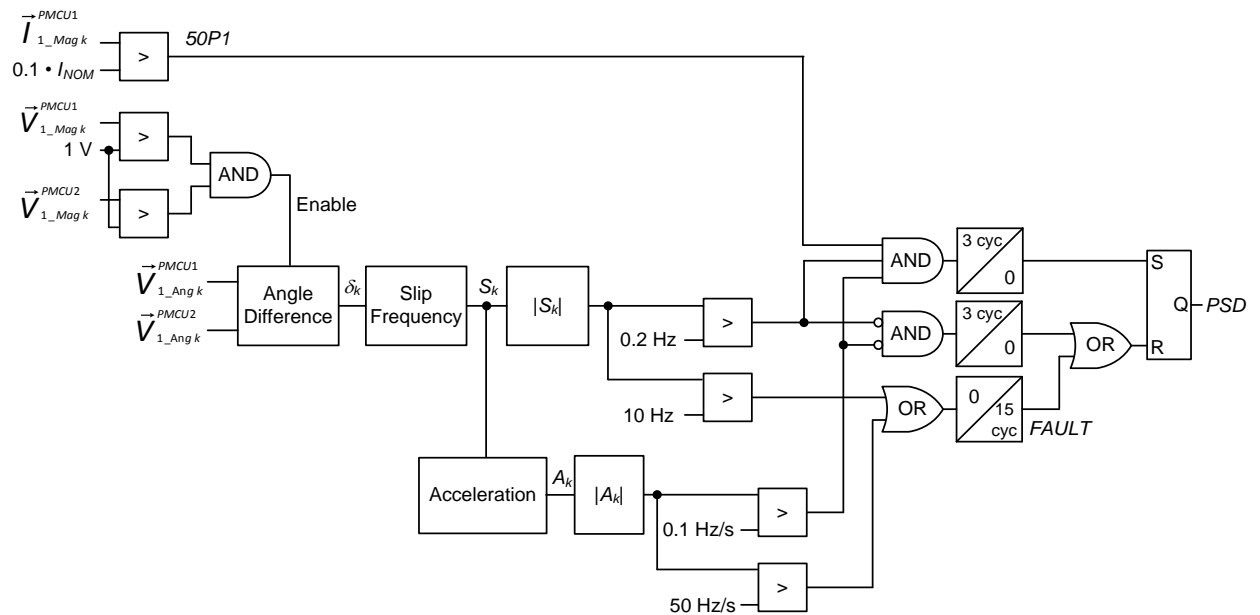
Figure 5.7   Synchrophasor-based power swing detection algorithm.

The PSD algorithms use the enable logic described in Section 5.4 for enabling the angle difference calculation. The algorithm asserts the *PSD* bit (see Figure 5.7), indicating the existence of a power swing condition, when all of the following conditions exist for three cycles:

- The positive-sequence current magnitude $\vec{I}_{1\_\text{Mag}\,k}^{PMCU1}$ measured by PMCU 1 is greater than $0.1 \bullet I_{NOM}$.

- $\left| S_k \right|$ is greater than 0.2 Hz.

- $\left| A_k \right|$ is greater than 0.1 Hz/s.

The *PSD* bit deasserts when any of the following conditions occur:

- $\left| S_k \right|$ is greater than 10 Hz.

- $\left| A_k \right|$ is greater than 50 Hz/s.

- $\left| S_k \right|$ is less than or equal to 0.2 Hz and $\left| A_k \right|$ is less than or equal to 0.1 Hz/s for three cycles.

5.6   Predictive Out-of-Step Tripping

The synchrophasor-based, out-of-step tripping (OOST) method proposed in [26, 27, 28, 29] for two-area power systems requires that the electrical center be between the PMCUs that acquire the synchrophasor measurements. The OOST element uses the positive-sequence voltage synchrophasors measured at two power system buses to calculate angle difference δ_k, slip frequency S_k, and acceleration A_k, according to (5.11), (5.12), and (5.13).

The OOST element characteristic shown in Figure 5.8 defines the power system stable and unstable operating regions on a slip frequency-acceleration plane [26, 27, 28, 29]. This characteristic identifies unstable swings before the OOS condition occurs. When the operating point is outside the stable region for a predetermined time (e.g. 150 ms), the *OOST* element asserts, allowing the protection scheme to take fast remedial actions.
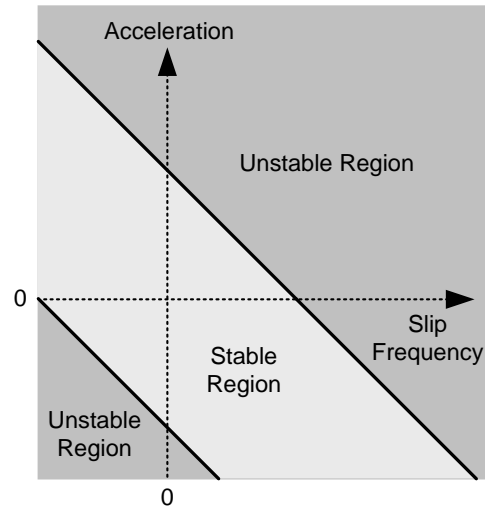
Figure 5.8   The OOST element uses slip frequency and acceleration information to detect unstable swings.

Equations (5.14) and (5.15) define the upper and lower unstable regions of the characteristic; Figure 5.9 illustrates the function block of this element. The calculations are described in more detail in *Appendix F*.

$$A_k > 78\_Slope \cdot S_k + A_{Offset} \tag{5.14}$$

$$A_k < 78\_Slope \cdot S_k - A_{Offset} \tag{5.15}$$
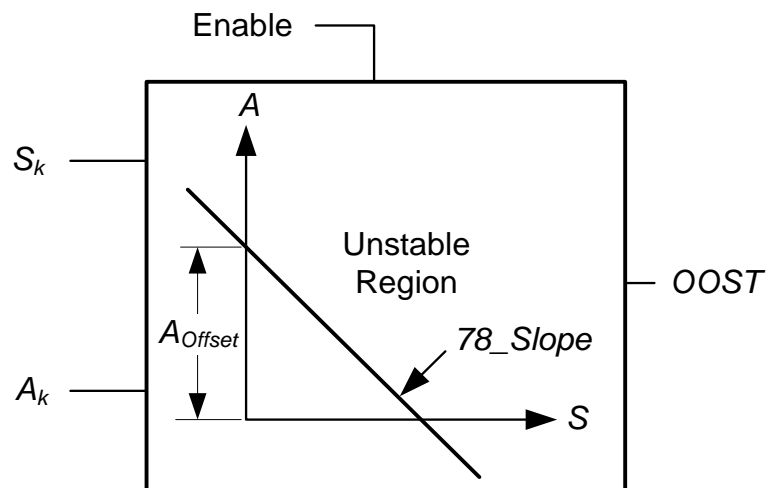
Figure 5.9   *78_Slope* and A_{Offset} define the upper unstable region of the OOST element.

5.6.1 Implementation of an Out-of-Step Tripping SIPS

The OOST SIPS algorithm is implemented in the SPU shown in Figure 5.4. In this scheme, the PMCUs send system voltage phasors to the SPU. The SPU uses its time-deterministic run time system (RTS) to run the logic and algorithms of the OOST element in real time. After time alignment, the positive-sequence voltage phasors that the PMCUs acquire are available to the RTS. The OOST scheme, shown in Figure 5.10, includes the following function blocks:

- PMCU01: PMCU at Area 1.

- PMCU02: PMCU at Area 2.

- Diff: Angle difference calculation.

- Slip_Calc: Slip frequency calculation.

- Acc_Calc: Acceleration calculation.

- Out_of_Step_Trip: Out-of-step tripping algorithm and logic.

- TRIP: Command to send the remedial action.
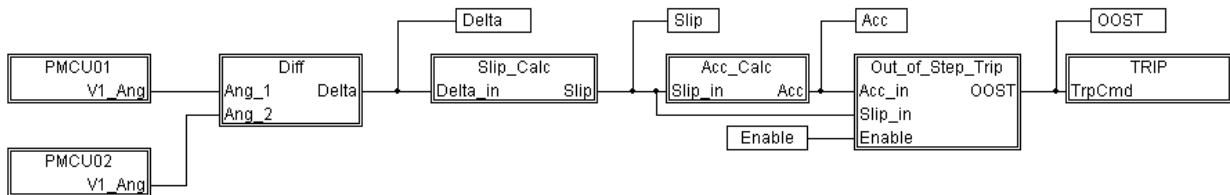
Figure 5.10   Implementation of the OOST scheme through use of the SPU.

5.6.2 Performance of the Out-of-Step Tripping SIPS

The system in Figure 5.11 shows two generators in one area of the power system and a third generator in the other area representing the rest of the power system. In this system, the electrical center is at the transmission line that connects Busbars 2 and 3. Figure 5.11 also shows the main components of the SIPS and the location of the PMCUs that acquire the synchrophasor measurements. PMCU 1 is at the generator Busbar 1. PMCU 2 is at the system Busbar 5. This PMCU placement ensures that the electrical center of the power system is between the two PMCUs. In this application, the PMCUs send synchrophasor messages over Ethernet to the SPU at 60 messages per second. The SIPS detects unstable power swings and sheds the 396 MVA generator (Generator 2) to maintain system stability. This power system was modeled in the Real-Time Digital Simulator (RTDS®) to analyze the performance of the OOST scheme in real time.
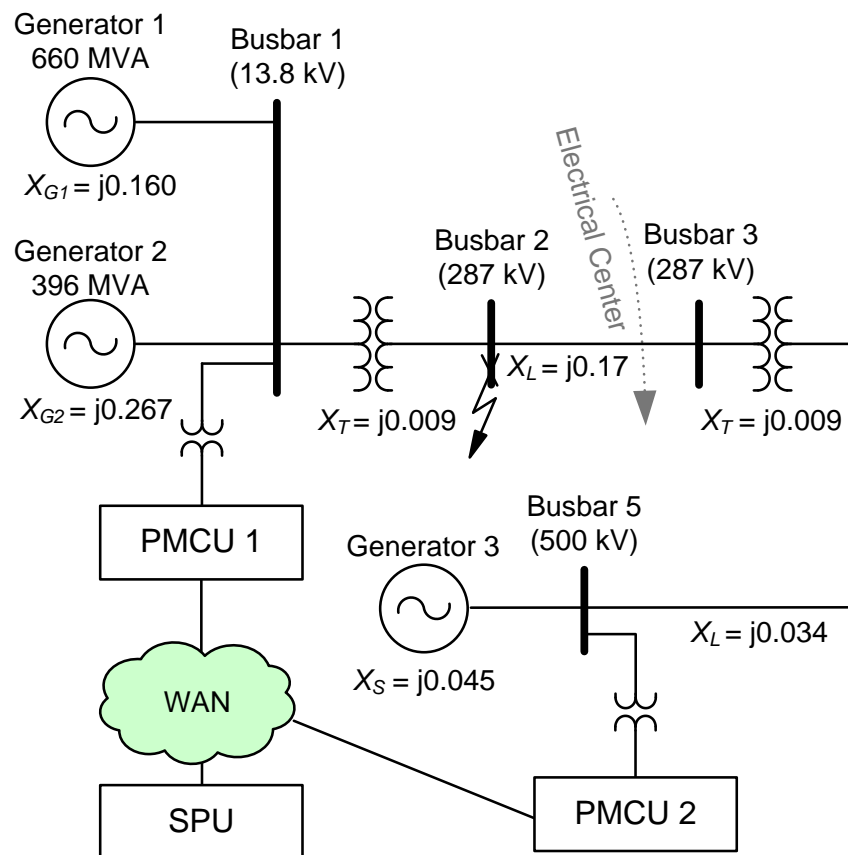
Figure 5.11   System model to analyze the performance of the OOST scheme in real time.

The power system shown in Figure 5.11 experiences a temporary fault at Busbar 2 that causes changes in machine angle, speed, and acceleration. It is assumed that the temporary fault

extinguishes automatically. If the fault clearing time exceeds 6.9 cycles, the critical clearing time, the system becomes unstable. Table 5.1 describes the three scenarios used to analyze the performance of the OOST element [29].

Table 5.1 Scenarios to Analyze the Performance of the OOST Element.

Scenario	Description	Comments
1	Stable operating conditions.	The fault clears in 6.0 cycles and the system remains stable.
2	Unstable operating conditions without remedial action.	The fault clears in 7.0 cycles and the system becomes unstable.
3	Unstable operating conditions with remedial action.	The fault clears in 7.0 cycles, the operating point remains outside the OOST characteristic longer than 9 cycles (150 ms), the scheme detects this operating condition and trips Generator 2 to maintain system stability.

The programmable output message of the SPU together with synchrophasor visualization and archiving software were used to capture the angle difference, slip frequency and acceleration calculations, and the OOST scheme output in real time.

5.6.2.1 Angle Difference Calculations

Figure 5.12, Figure 5.13, and Figure 5.14 show the screen captures of the angle difference calculations for the three scenarios. In the first scenario, the system returns to the initial stable operating conditions in approximately 13 seconds. In the second scenario, the angle difference between the two monitored busbars increases beyond $180°$ after approximately 5.7 seconds, and the system becomes unstable. In the third scenario, the angle difference begins to increase as shown in the angle difference plot of Figure 5.14. The OOST scheme detects that the operating point is outside of its characteristic (see assertion of the *OOSP* bit in the bottom plot of Figure 5.14), and after 150 ms the SPU asserts the *OOST* bit and sends the trip command (approximately 0.9 seconds after the fault clears) to shed Generator 2 and maintain system stability. In this case, the final angle difference of $6°$ corresponds to the new operating condition with Generator 2 out of service.
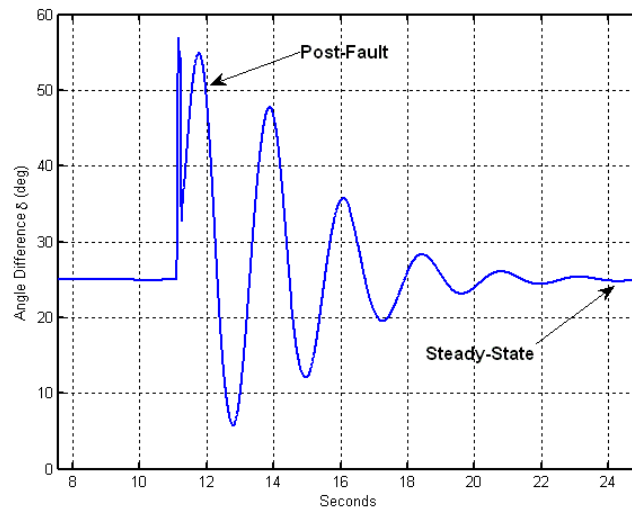
Figure 5.12   Angle difference calculations for stable operating conditions.
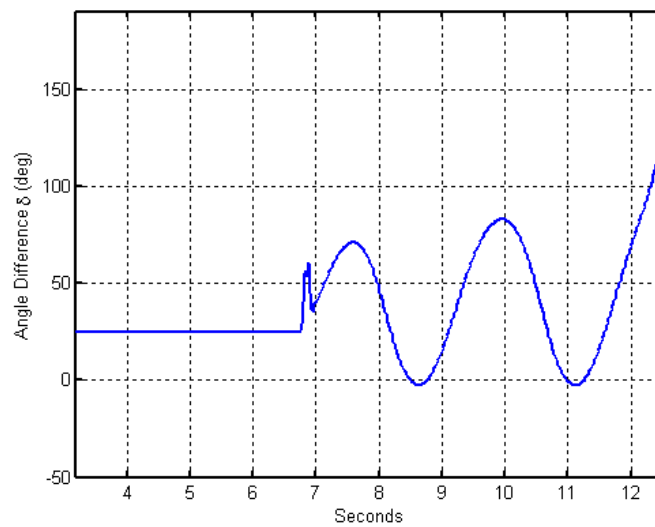
Figure 5.13   Angle difference calculations for unstable operating conditions without remedial action.
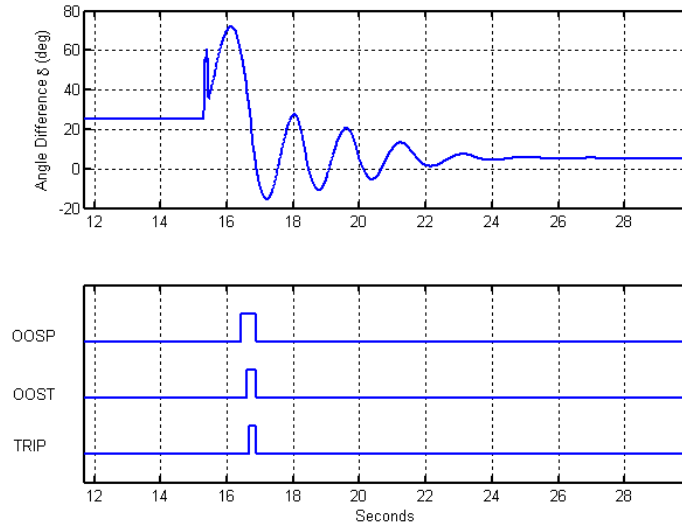
Figure 5.14   Angle difference calculations show that the system becomes unstable after the fault is cleared and stabilizes by the remedial action.

5.6.2.2 Slip Frequency and Acceleration Trajectories on the Slip Frequency-Acceleration Plane

Figure 5.15, Figure 5.16, and Figure 5.17 show the slip frequency and acceleration trajectories and the characteristic of the OOST element on the slip frequency-acceleration plane for the three scenarios. In the first scenario, Figure 5.15 shows that the operating point remains inside the stable region of the OOST element characteristic. In the second scenario, Figure 5.16 shows that the operating point enters the unstable region in each of the oscillations and then increases without restriction after the second oscillation.

Figure 5.17 shows two trajectories for the third scenario: the trajectory before the remedial action and the trajectory after the remedial action. The operating point remains in the unstable region longer than 150 ms, and the OOST scheme trips Generator 2. After the generator trip, the system jumps to the stable region and remains stable.
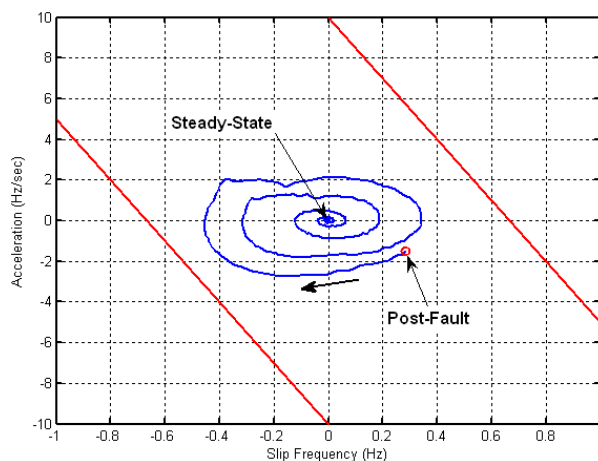
Figure 5.15   Slip frequency and acceleration trajectory for stable operating conditions.
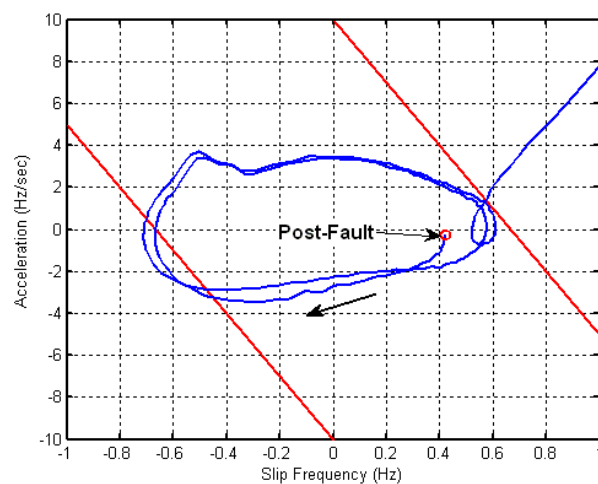
Figure 5.16   Slip frequency and acceleration trajectory for unstable operating conditions.
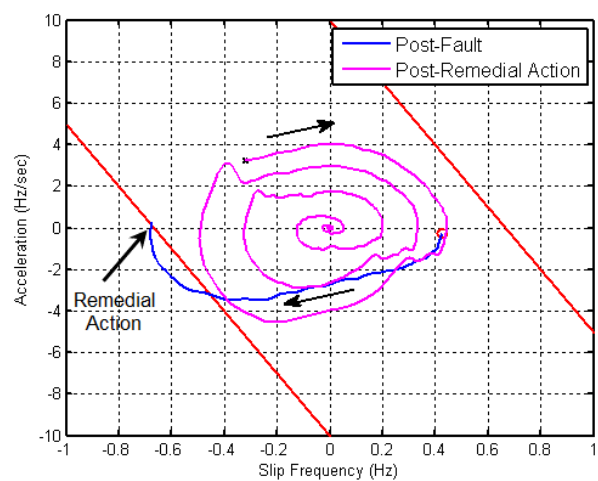
Figure 5.17   Slip frequency and acceleration trajectories before and after the 396 MVA generator trips.

5.7   Summary

The proposed out-of-step detection, power swing detection, and predictive out-of-step tripping algorithms presented in this chapter are included in US Patent 7930117 *Systems and methods for power swing and out-of-step detection using time-stamped data* and in [29]. These algorithms use synchrophasor measurements that allow implementation of SIPSs that require minimum information of the network topology and automatically adapt to changing operating conditions of the power system. This chapter showed that the total operating time of the SIPS is fast enough to maintain power system stability.

Real-time digital simulations of the power swing detection scheme demonstrated the benefit of using the acceleration between two power system areas to identify out-of-step operating conditions before the system becomes unstable.

The synchrophasor processing unit (SPU), described in *Chapter 3*, acquires synchrophasor measurements from PMCUs located at different geographical areas to run synchrophasor applications. Applications of the SPU include closed loop control schemes for detecting and mitigating unstable power swing conditions and unstable power inter-area oscillations. *Appendix F* shows details of the implementation of the proposed SPU power system dynamics monitor. A scheme that identifies inter-area oscillations is discussed in the next chapter.

Chapter 6 System Identification and Real-Time Power System Oscillation Detection Using Modal Analysis

6.1   Introduction

Power system interconnected networks that encompass large geographical regions are prone to dynamic oscillation problems. The August 10, 1996 blackout in the Western Region of North America is one example of such problems [65]. Figure 6.1 shows the real power flow in one of the lines between Malin and Round Mountain measured at Malin during this disturbance. One can observe that power oscillations increased after the Keeler-Allston line tripped at 15:42:03. The power oscillations increased exponentially after the Ross-Lexington line was disconnected from the network and McNary generation dropped off at 15:47:36. Network separation occurred at 15:48:51 because of out-of-step conditions. To avoid these power system disturbances, it is desirable to identify these under-damped oscillations and take remedial actions before the system collapses. Real-time modal analysis allows determination of the signal modal content from measured quantities such as real power, frequency, voltage angle difference, generator rotor angle and speed, and so on. Based on this analysis, this chapter presents a system that identifies undesirable operating conditions and takes automated actions that prevent system collapse. This chapter describes a SIPS that uses an algorithm to determine the mode frequency, amplitude, and damping of these input signals in real time based on the Prony method for modal analysis (PMA) [12, 30, 66, 67]; this method has been typically used for post-mortem analysis.
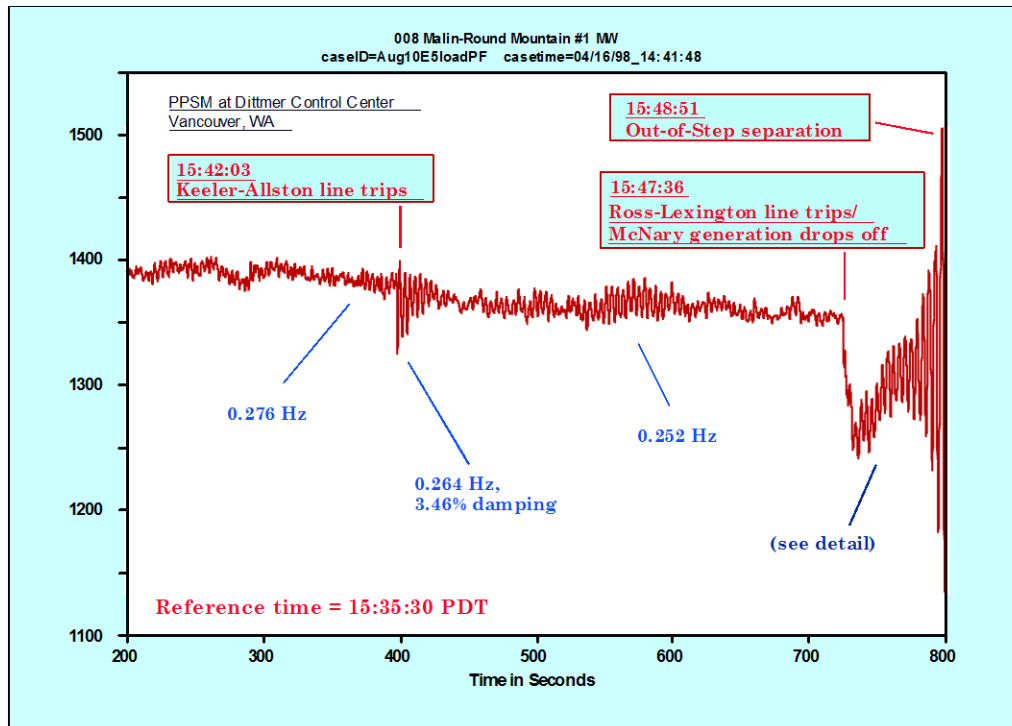
Figure 6.1   Malin-Round Mountain real power oscillations measured during the WSCC (Western Systems Coordinating Council) system August 10, 1996 blackout.

A power system model suitable for small signal stability analysis is used to create power system signals of known system characteristics to emulate field measurements and validate the proposed approach. PMA is used to estimate the eigenvalues, amplitude, frequency, damping, and phase for each mode of the emulated signal and compare the PMA estimated values against known power system characteristics to validate the PMA estimation process. This chapter also describes a wide-area control system that detects power system inter-area oscillations in real time and its application in a transmission network to avoid system collapse and allow increase in power transfer levels between different power system networks.

6.2   Power System Models for Small Signal Analysis

Two cases are presented for identifying the characteristics of power system signals. The first case consists of a model with a single generator equivalent connected to an infinite bus system through one step-up transformer and one transmission line; the machine field excitation system and machine damping windings are ignored for simplicity [68]. In the second case, the machine field circuit dynamics are added to analyze the effects of field flux variations on the rotor angle of the machine.

Both models are used to generate rotor angle and machine speed signals. These signals are later used to estimate system characteristics through the use of PMA.

6.2.1 Power System Model That Excludes Field Circuit Dynamics

Using the system notation shown in Figure 6.2 and excluding all system resistances, Equation (6.1) determines the power, P, at the generator terminals that is equal to the electromagnetic torque, T_e, in per unit.

$$T_e = P = \frac{E_I \cdot E_S}{X_T} \cdot \sin \delta \qquad (6.1)$$

where:

X_T is equal to $X_d' + X_S$,

X_d' is the direct axis transient reactance,

X_S is the network equivalent system impedance at the generator terminals,

E_I is the generator excitation voltage magnitude behind X_d',

E_S is the infinite bus voltage magnitude,

δ is the angle by which the generation excitation voltage leads the infinite bus voltage.
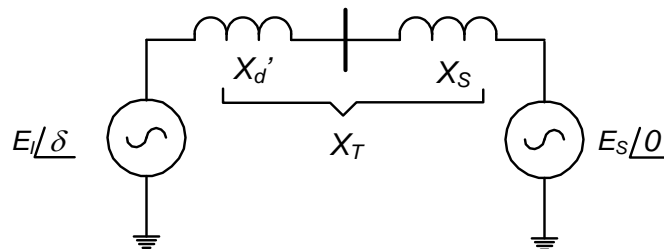
Figure 6.2 Generator connected to a system equivalent network.

Equation (6.2) defines the incremental electromagnetic torque, ΔT_e, around the initial operating conditions, $\delta = \delta_0$.

$$\Delta T_e = \frac{\partial T_e}{\partial \delta} \cdot \Delta \delta = \frac{E_I \cdot E_S}{X_T} \cdot \cos \delta_0 \cdot \Delta \delta = K_S \cdot \Delta \delta \tag{6.2}$$

where:

K_S is the synchronizing torque coefficient in pu torque/rad.

The linearized equations of motion are [68, 69, 70]:

$$\frac{d(\Delta \omega_r)}{dt} = \frac{1}{2 \cdot H} \left[\Delta T_m - K_S \cdot \Delta \delta - K_D \cdot \Delta \omega_r \right] \tag{6.3}$$

$$\frac{d(\Delta \delta)}{dt} = \omega_0 \cdot \Delta \omega_r \tag{6.4}$$

where:

ΔT_m is the incremental mechanical torque in pu,

K_D is the damping torque coefficient in pu torque/pu,

H is the inertia constant in seconds,

$\Delta \omega_r$ is the speed deviation in pu,

$\Delta \delta$ is the rotor angle deviation in electrical radians,

ω_0 is the rated speed in electrical radians/second.

Figure 6.3 shows the linearized model that represents (6.3) and (6.4).
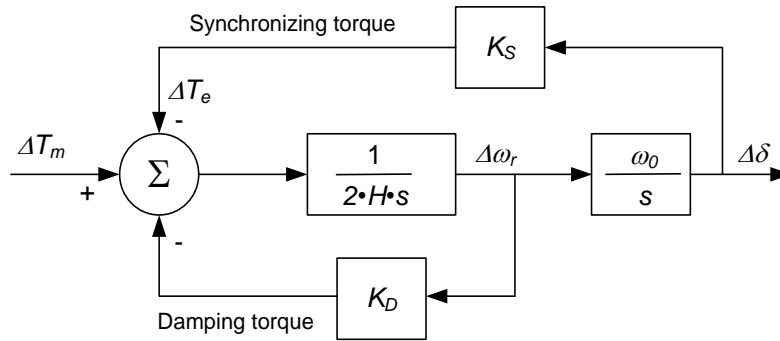
Figure 6.3   Linearized model of a generator connected to a system equivalent network.

The characteristic equation of the system shown in Figure 6.3 is as follows:

$$s^2 + \frac{K_D}{2 \cdot H} \cdot s + \frac{K_S \cdot \omega_0}{2 \cdot H} = 0 \qquad (6.5)$$

Equation (6.5) has the following general form:

$$s^2 + 2 \cdot \zeta \cdot \omega_n \cdot s + \omega_n^2 = 0 \qquad (6.6)$$

where:

ζ is the damping ratio,

ω_n is the under-damped natural frequency.

The solution of (6.5) gives us the system eigenvalues:

$$\lambda_1 = \sigma + j \cdot \omega_d \qquad (6.7)$$

$$\lambda_2 = \sigma - j \cdot \omega_d \qquad (6.8)$$

Obtain the damping ratio, ζ, and the frequency of oscillation, f_{Osc}, in *Hz* from the eigenvalue, λ, as follows:

$$\zeta = -\frac{\sigma}{\sqrt{\sigma^2 + \omega_d^2}} \qquad (6.9)$$

$$f_{Osc} = \frac{\omega_d}{2 \cdot \pi} \qquad (6.10)$$

6.2.2 Power System Model That Includes Field Circuit Dynamics

To include the effect of field flux variations, it is assumed that the field voltage remains constant.
Equation (6.11) represents the linearized form of the electromagnetic torque [68, 69, 70].

$$\Delta T_e = K_1 \cdot \Delta \delta + K_2 \cdot \Delta \Psi_{fd} \tag{6.11}$$

where:

$$K_1 = n_1 \left(\Psi_{ad0} + L_{aqs} \cdot i_{d0} \right) - m_1 \left(\Psi_{aq0} + L'_{ads} \cdot i_{q0} \right) \tag{6.12}$$

$$K_2 = n_2 \left(\Psi_{ad0} + L_{aqs} \cdot i_{d0} \right) - m_2 \left(\Psi_{aq0} + L'_{ads} \cdot i_{q0} \right) + \frac{L'_{ads}}{L_{fd}} \cdot i_{q0} \tag{6.13}$$

$$\Psi_{ad} = -L_{ads} i_d + L_{ads} i_{fd} \tag{6.14}$$

$$\Psi_{aq} = -L_{aqs} i_q \tag{6.15}$$

$$m_1 = \left. \frac{\partial i_d}{\partial \delta} \right|_{\delta_0} = \frac{E_s \left(X_{Tq} \cdot \sin \delta_0 - R_T \cdot \cos \delta_0 \right)}{D} \tag{6.16}$$

$$n_1 = \left. \frac{\partial i_q}{\partial \delta} \right|_{\delta_0} = \frac{E_s \left(R_T \cdot \sin \delta_0 - X_{Td} \cdot \cos \delta_0 \right)}{D} \tag{6.17}$$

$$m_2 = \left. \frac{\partial i_d}{\partial \Psi_{fd}} \right|_{\Psi_{fd0}} = \frac{X_{Tq}}{D} \cdot \frac{L_{ads}}{\left(L_{ads} + L_{fd} \right)} \tag{6.18}$$

$$n_2 = \left. \frac{\partial i_q}{\partial \Psi_{fd}} \right|_{\Psi_{fd0}} = \frac{R_T}{D} \cdot \frac{L_{ads}}{\left(L_{ads} + L_{fd} \right)} \tag{6.19}$$

$$L'_{ads} = \frac{1}{\dfrac{1}{L_{ads}} + \dfrac{1}{L_{fd}}} \tag{6.20}$$

$$R_T = R_a + R_S \tag{6.21}$$

$$X_{Tq} = X_S + \left(L_{aqs} + L_\ell \right) \tag{6.22}$$

$$X_{Td} = X_S + \left(L'_{ads} + L_\ell \right) \tag{6.23}$$

$$D = R_T^2 + X_{Tq} \cdot X_{Td} \tag{6.24}$$

The linearized equations to include the field circuit effect are as follows:

$$\frac{d(\Delta\omega_r)}{dt} = \frac{1}{2\cdot H}\left[\Delta T_m - K_1 \cdot \Delta\delta - K_2 \cdot \Delta\Psi_{fd} - K_D \cdot \Delta\omega_r\right] \tag{6.25}$$

$$\frac{d(\Delta\delta)}{dt} = \omega_0 \cdot \Delta\omega_r \tag{6.26}$$

$$\Delta\Psi_{fd} = \frac{K_3}{1+\dfrac{d(T_3)}{dt}}\left[\Delta E_{fd} - K_4 \cdot \Delta\delta\right] \tag{6.27}$$

where:

$$K_3 = -\frac{L_{fd}}{L_{adu}\left(1 - \dfrac{L_{ads}^{'}}{L_{fd}} + m_2 \cdot L_{ads}^{'}\right)} \tag{6.28}$$

$$K_4 = -\frac{L_{adu} \cdot m_1 \cdot L_{ads}^{'}}{L_{fd}} \tag{6.29}$$

$$T_3 = K_3 \cdot T_{d0}^{'}\frac{L_{fd}}{L_{adu}} \tag{6.30}$$

Figure 6.4 shows the linearized model that represents (6.25), (6.26), and (6.27).
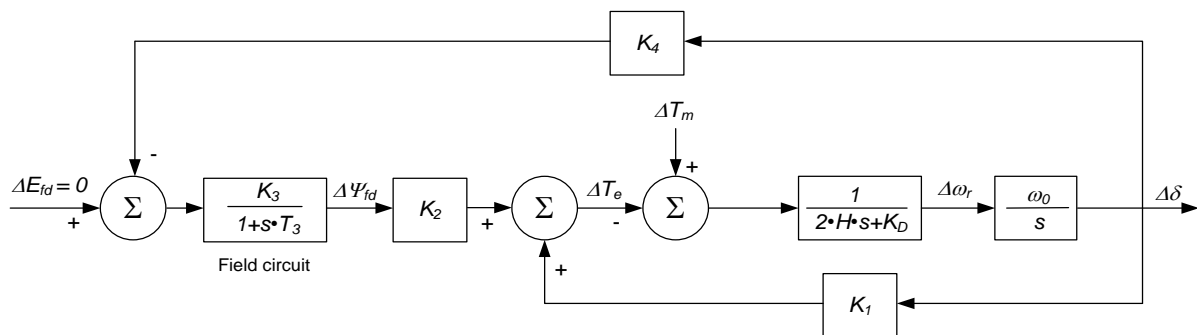
Figure 6.4   Linearized model of a generator connected to a system equivalent network with constant field voltage.

6.3 System Identification Using Modal Analysis (MA)

Modal analysis is intended to fit a time-varying waveform of pre-specified form to the actual waveform [21] in terms of its natural frequencies and associated amplitude, phase, and damping. In this chapter, the PMA method, a method that originated in the 18th century for performing modal analysis [71], is used to extract the modal information of time-varying rotor angle signals obtained by using the previous power system models. PMA fits a linear model to a measured signal $y[n]$ where $y[n]$ is the output signal of a linear dynamic system sampled at a fixed rate. PMA is used to obtain the modes of the output signal $y[n]$; the modes of this signal correspond to the modes of the linear system that generated the output signal (*Appendix G* provides more details about PMA).

PMA uses linear combinations of multiple modes to approximate the original signal $y[n]$. For an array of data samples $y[1]$, …, $y[N]$, the PMA estimates $y[k]$ according to (6.31) for $1 \leq n \leq N$.

$$\hat{y}[n] = \sum_{m=1}^{M} A_m e^{\sigma_m \cdot k \cdot \Delta t} \cdot \cos\left(2 \cdot \pi \cdot f_m \cdot k \cdot \Delta t + \phi_m\right) \tag{6.31}$$

where:

$\hat{y}[n]$	is the estimated signal,
N	is the number of samples of the observation window,
M	is the number of modes,
m	is the signal mode,
A_m	is the amplitude of mode m,
σ_m	is the damping constant of mode m in s^{-1},
f_m	is the frequency of mode m in *Hz*,
ϕ_m	is the phase of mode m in radians,
Δt	is the sampling interval in seconds.

6.3.1 Damping ratio

PMA uses (6.32) to calculate the damping ratio ζ_m from the frequency and the damping constant and to determine the rate of decay in the oscillation amplitude.

$$\zeta_m = -\frac{\sigma_m}{\sqrt{\sigma_m^2 + \left(2 \cdot \pi \cdot f_m\right)^2}} \qquad (6.32)$$

A negative damping ratio (positive σ_m) indicates an increasing oscillation, an unwanted operating condition that can lead to power system instability if a remedial action is not taken within a few seconds.

6.3.2   Signal-to-noise ratio

PMA also compares the estimated signal against the original signal. MA uses (6.33) to calculate the signal-to-noise ratio *SNR* (dB), quantifying the quality of the fit. PMA is a linear approximation technique, so it will produce a low *SNR* value if the data sample array contains nonlinear transitions. In power systems, discrete switching events (such as line tripping) can cause nonlinear transitions. The *SNR* value normally improves as a switching event leaves the observation window of PMA and the power system settles into pure oscillation mode. A high *SNR* value (greater than 80 dB, for example) indicates that the analysis result is a good approximation of the original signal [66].

$$SNR = 10 \bullet Log_{10}\left(\frac{\sum\limits_{n=1}^{N} y[n]^2}{\sum\limits_{n=1}^{N}\left(y[n] - \hat{y}[n]\right)^2}\right) \qquad (6.33)$$

where:

$y[n]$ is the original signal,

$\hat{y}[n]$ is the estimated signal.

Next, rotor angle signals are generated using the model power systems discussed previously. In the first case, the model does not include field circuit dynamics. In the second case, field circuit dynamics are included and the power system performance is shown with and without field circuit dynamics. The estimated eigenvalues, oscillating frequency, and damping ratio are compared against the analytically calculated characteristics. Additionally, the estimated signal is compared against the original signal through the use of *SNR* calculations.

6.3.3 Case 1 Power System Model Identification That Excludes Field Circuit Dynamics

The system shown in Figure 6.5 corresponds to Example 12.2 in [68]. The model includes one generator equivalent, one transformer, one transmission line, and the network equivalent.
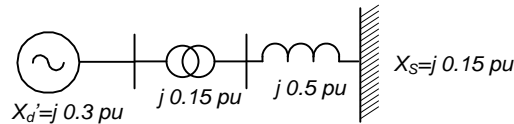
Figure 6.5   Power system model used to generate the rotor angle signal. The model includes one generator, one transformer, one transmission line, and the network equivalent impedance.

Figure 6.6 shows the corresponding Simulink$^®$ model; the figure also includes the input values of ω_0, H, K_S, K_D, and the initial rotor angle δ_{ini}. This model calculates the machine rotor speed, ω_r, and rotor angle, δ. The rotor angle signal that this model generates is used to estimate the eigenvalues of the system and the amplitude and phase for each mode. To generate a system transient, the simulation is started with a five electrical degree change in the machine rotor angle. The original signal-sampling rate is 960 Hz. This signal is decimated by 16 to obtain the data signal sampled at 60 Hz. Signals sampled at 30 or 60 Hz (in 60 Hz systems) are typically used for small signal stability analysis.
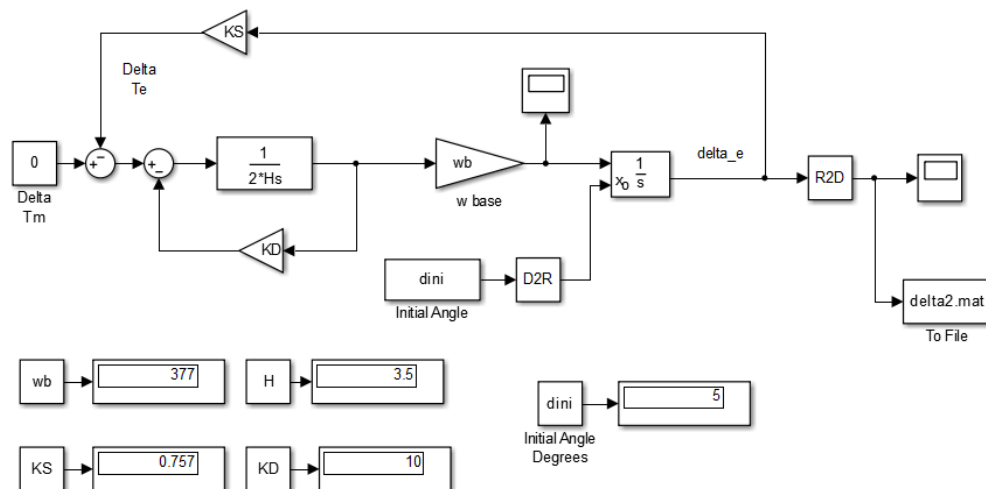
Figure 6.6   Linearized Simulink$^®$ model of a generator connected to a system equivalent network.

Table 6.1 compares the analytically calculated eigenvalues, oscillation frequency, and damping ratio with the PMA estimated values. The estimated values are approximately equal to the calculated values.

Table 6.1   Calculated and estimated eigenvalues, oscillation frequency, and damping ratio for the system model that excludes field circuit dynamics.

	Calculated Values	Estimated Values
Eigenvalues, λ	- 0.714 $\pm$ j 6.35	- 0.7143 $\pm$ j 6.345
Oscillation frequency, f_{Osc} (Hz)	1.0101	1.0098
Damping Ratio, ζ	0.112	0.1119

The *SNR* of the estimated signal is 266 dBs. Figure 6.7 shows the plot of the original and estimated signals; the estimated signal is on top of the original signal. The figure demonstrates an excellent fit.
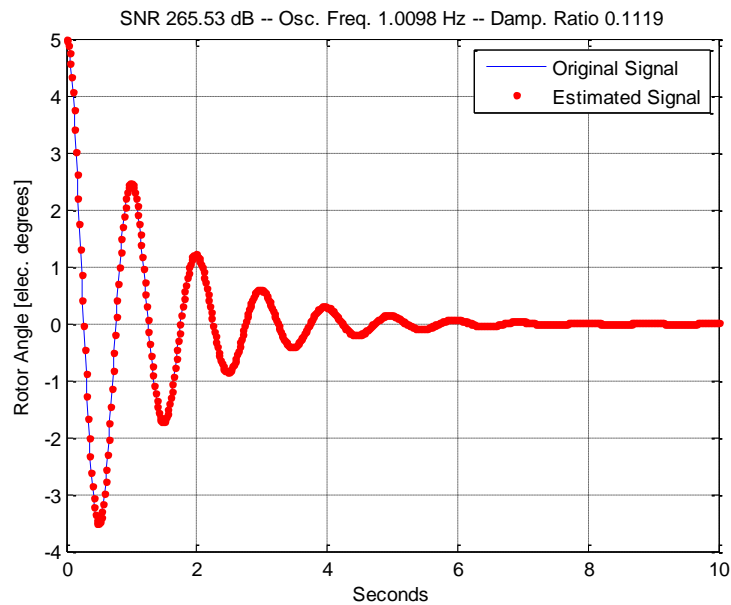
Figure 6.7   The *SNR* of the estimated signal is 265 dB, which is an indication of an excellent fit.

6.3.4 Case 2 Power System Model Identification That Includes Field Circuit Dynamics

The power system in Case 2 is similar to the system in Case 1; the only difference is that, in this case, the model includes field circuit dynamics. This case corresponds to Example 12.3 in [68]. Figure 6.8 shows the corresponding Simulink® model; the figure also includes the input values of ω_0, H, K_1, K_2, K_3, K_4, T_3, and the rotor initial angle δ_{ini}.
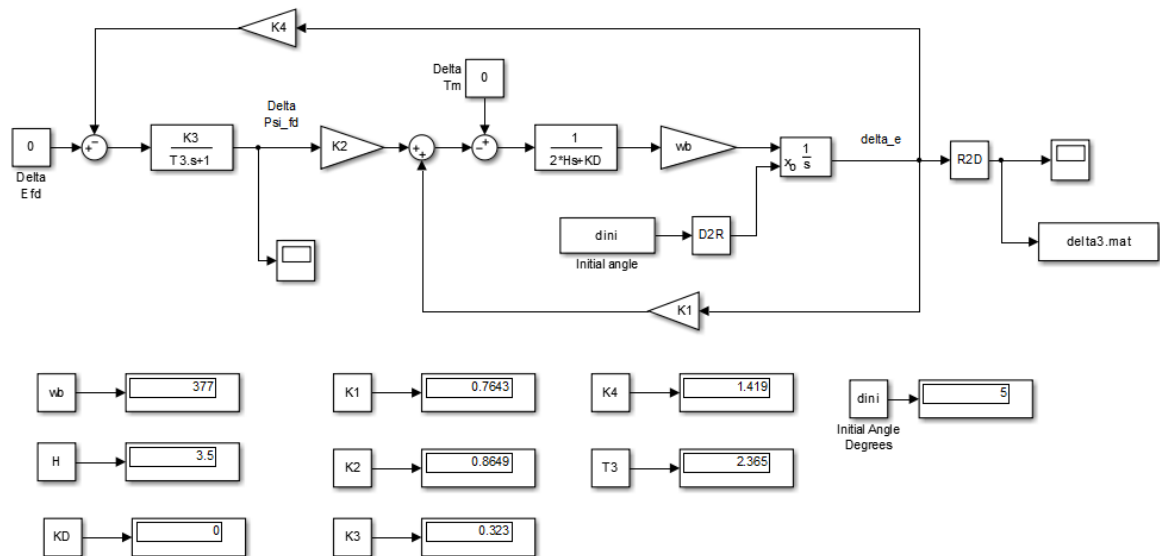
Figure 6.8   Linearized Simulink® model of a generator connected to a system equivalent network with constant field voltage.

Table 6.2 compares the analytical calculation of the eigenvalues, oscillation frequency, and damping ratio with the corresponding values estimated using PMA for the system that includes field circuit dynamics. As in the previous case, the estimated values are very close to the calculated values.

Table 6.2   Calculated and estimated eigenvalues, oscillation frequency, and damping ratio for the system model that considers field circuit dynamics.

	Calculated Values	Estimated Values
Eigenvalues, λ	- 0.11 $\pm$ j 6.41	- 0.1095 $\pm$ j 6.4114
	- 0.204	- 0.2038
Oscillation frequency, f_{Osc} (Hz)	1.02	1.0204
Damping Ratio, ζ	0.017	0.0171

The *SNR* of the estimated signal is 57 dBs, which is an indication of a good fit. Figure 6.9 shows the plot of the original and estimated signals; the estimated signal is on top of the original signal. Again, the fit is good.
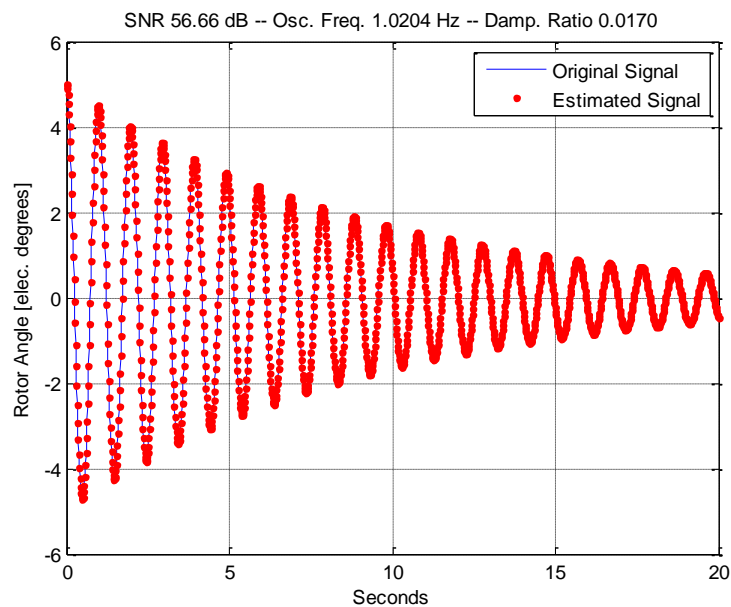
Figure 6.9   The *SNR* of the estimated signal is 57 dBs, which is an indication of a good fit.

6.4 Real-Time Power System Inter-Area Oscillation Detection Using Modal Analysis

Power system disturbances, such as line tripping and the dropping of generation, cause local and inter-area power system oscillations. Local oscillations involve a few generators within a small portion of a power system and have little impact on the overall power system. Usually, local oscillation frequency ranges from 1 to 5 Hz. Inter-area oscillations, which generally involve a group of generators in one area of the power system that swings against a group of generators in another area, normally range in frequency from 0.1 to 0.8 Hz [72]. Inter-area oscillations constrain the amount of power that can be transferred through some parts of interconnected power grids. Without proper remedial actions, inter-area oscillations can result in power system islanding or major blackouts.

Traditionally, power system planners study inter-area oscillations by applying MA to the results of power system dynamic simulations and perform post-mortem analysis of system disturbances. This analysis, while good for understanding what happened after the disturbance, neither prevents occurrence of the disturbance nor aids in fast mitigation of disturbance effects. A system that performs real-time MA is required to promptly identify undesirable operating conditions and take remedial action to maintain system stability.

The power system disturbance detection scheme implemented in the SPU in Figure 6.10 detects unstable inter-area oscillations in real time; the SPU processes the incoming data at fixed time intervals and automatically initiates remedial actions. The system uses synchronized phasor measurements that are taken at strategic locations of the power system as inputs to MA calculations. The input signal for MA can be selected from original synchrophasor measurements or from quantities derived from synchrophasors. This input signal could be: frequency, phasor magnitude, phasor angle, power, angle difference, etc. MA calculation output includes the following information per mode: amplitude, phase, frequency, damping constant, and damping ratio. The Local PMCU (C37.118 server) can be configured to send the results of the MA calculations to an external C37.118 client. The MA calculations are also available to the mode identification and control logic (MICL) that detects undesired oscillations, issues alarms, and sends remedial action commands when the logic detects undesired operating conditions that compromise the operation of the power system.
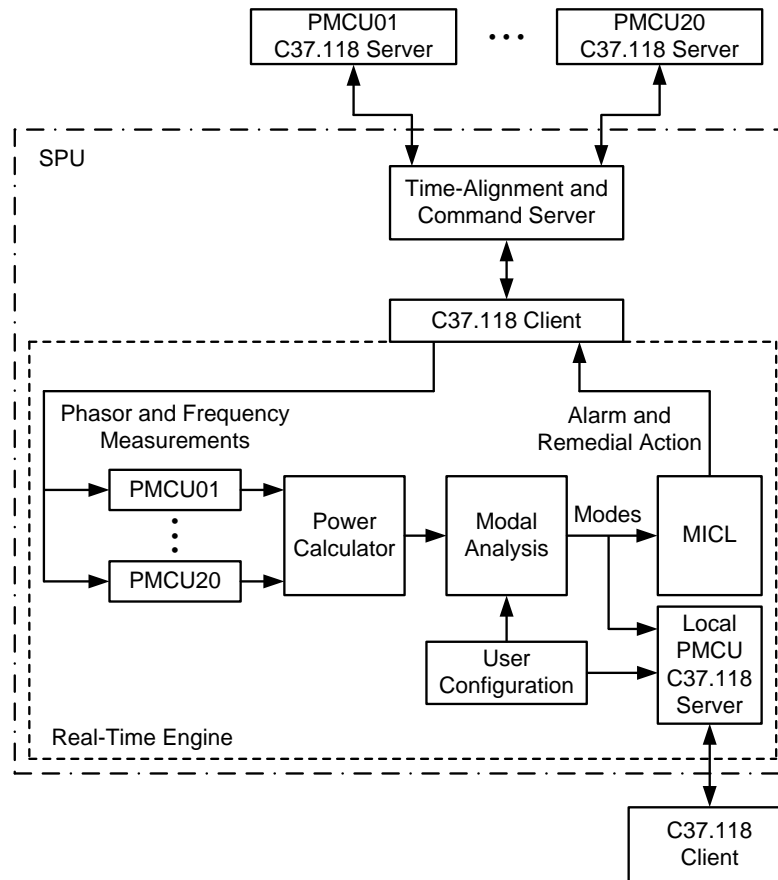
Figure 6.10   Real-time power system disturbance detection scheme.

6.4.1   Mode Identification and Control Logic (MICL)

The MICL is part of the real-time power system disturbance detection scheme shown in Figure 6.10. The output of the modal analysis calculation is fed into the input of the MICL. The MICL identifies the existence of a particular mode of interest when the frequency of the monitoring signal is within a predefined frequency band. If the amplitude of the identified mode is greater than a predefined threshold and the damping ratio is less than a predefined threshold for a certain time, the logic activates a remedial action and issues an oscillation alarm. Figure 6.11 shows three steps of the MICL: mode identification, under-damped oscillation detection, and activation of the remedial action. The command to activate the remedial action is sent to the PMCUs through the command server shown in Figure 6.10.

Mode Identification and Control Logic
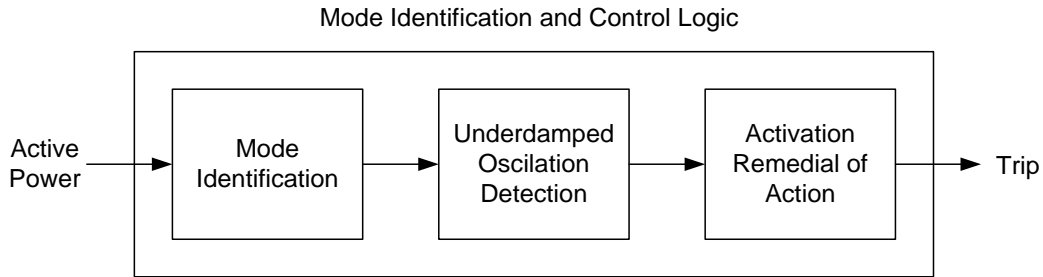
Figure 6.11   The mode identification and control logic identifies under-damped oscillations and activates the remedial action.

Figure 6.12 shows logic that identifies a particular mode of interest based on the oscillation frequency. When the oscillation frequency f_{mi} is within a pre-defined band defined by the limits f_{High} and f_{Low} and the mode amplitude A_{mi} exceeds a pre-defined threshold, A_{Thre}, the logic asserts the oscillation alarm and enables the damping ratio check. If the damping ratio is less than the pre-defined threshold, ζ_{Thre}, the logic activates the damping ratio alarm. If the above conditions persist longer than the *DRPU* delay, the logic activates a remedial action. The alarms and remedial action commands are routed to selected external devices through the command server. The command server then processes the remedial actions and sends the corresponding commands to external devices that execute the remedial actions.
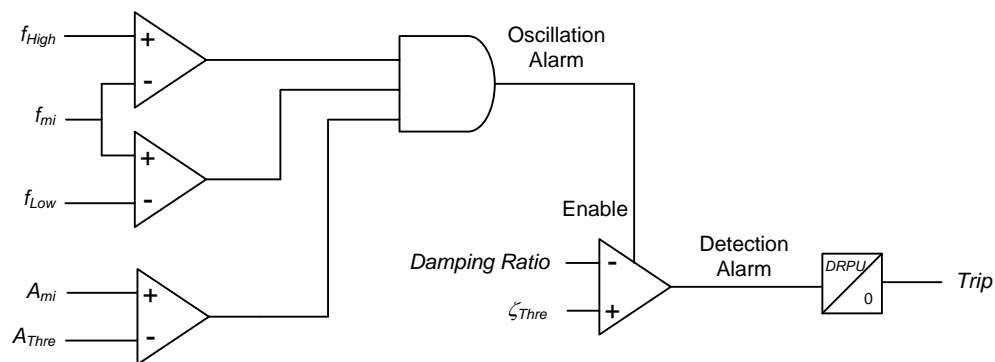
Figure 6.12   Mode identification logic and remedial action control logic.

6.4.2   Practical Application of Inter-Area Oscillation Detection

The power system shown in Figure 6.13 consists of two transmission networks with very different generation resources. The 400 kV network has more than 50 GW of installed capacity and is a strong system compared to the 230 kV network that has an installed capacity of about 7 GW. The

400/230 kV transformer interconnects these two networks to take advantage of the generation resources of the 400 kV network [31].

The 230 kV transmission network shown in Figure 6.13 distributes some of the imported power from the 400 kV network to the local network and wheels most of the power to the rest of the 230 kV system. Figure 6.13 also shows a system integrity protection scheme (SIPS) implemented to prevent collapse of the 230 kV network because of uncontrolled active power inter-area oscillations on the interconnection lines *CA6-CA9* and *CA8-CA9* that connect the power system to the rest of the 230 kV network. The SIPS consists of two PMCU field installations at the *CA6* and *CA8* substations in the corresponding interconnection line that send voltage and current synchrophasor measurements through a wide-area network (WAN) to an SPU installed at the control center.
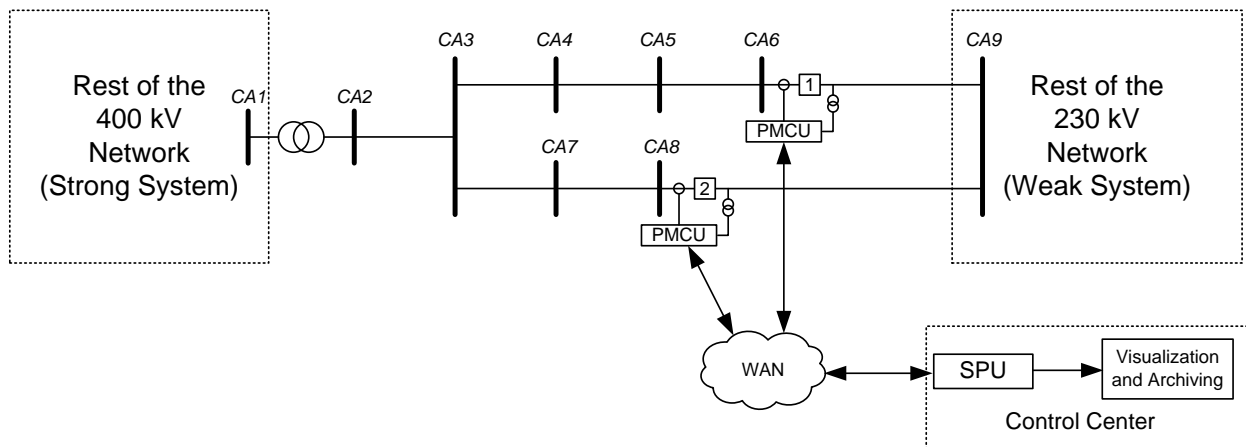
Figure 6.13   Interconnected transmission networks and SIPS to prevent power system collapse.

The SPU runs the real-time power system disturbance detection scheme (shown in Figure 6.10) that detects unstable power inter-area oscillations based on PMA and sends trip commands to Breakers 1 and 2 through the same WAN to disconnect the rest of the 230 kV, preventing system collapse. The SPU also sends the synchrophasor measurements to synchrophasor clients for visualization and archiving.

6.4.2.1 Synchrophasor and Command Messages

The PMCUs send voltage and current synchrophasors according to IEEE Std C37.118.2 [51] by using user datagram protocol (UDP) over Internet at 30 messages per second to the SPU. The SPU sends

remedial action commands to the PMCUs. These commands are embedded in the IEEE Std C37.118.2 command frame through use of transmission control protocol (TCP) over Internet (see Figure 6.14).
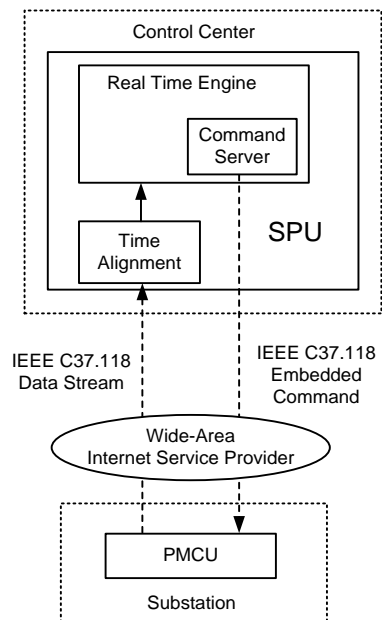
Figure 6.14   Synchrophasor data and command data exchange among PMCUs and SPU.

6.4.2.2 SPU Configuration

The SPU time aligns the synchrophasors from the two PMCUs, calculates the active powers of the two lines and adds them to obtain the total power of the interconnection (see Figure 6.15). The SPU executes the modal analysis algorithm, identifies the frequency of interest, verifies that the signal has adequate amplitude, runs the under-damped oscillation detection logic and, if necessary, sends trip commands to Breakers 1 and 2 to execute the remedial action.
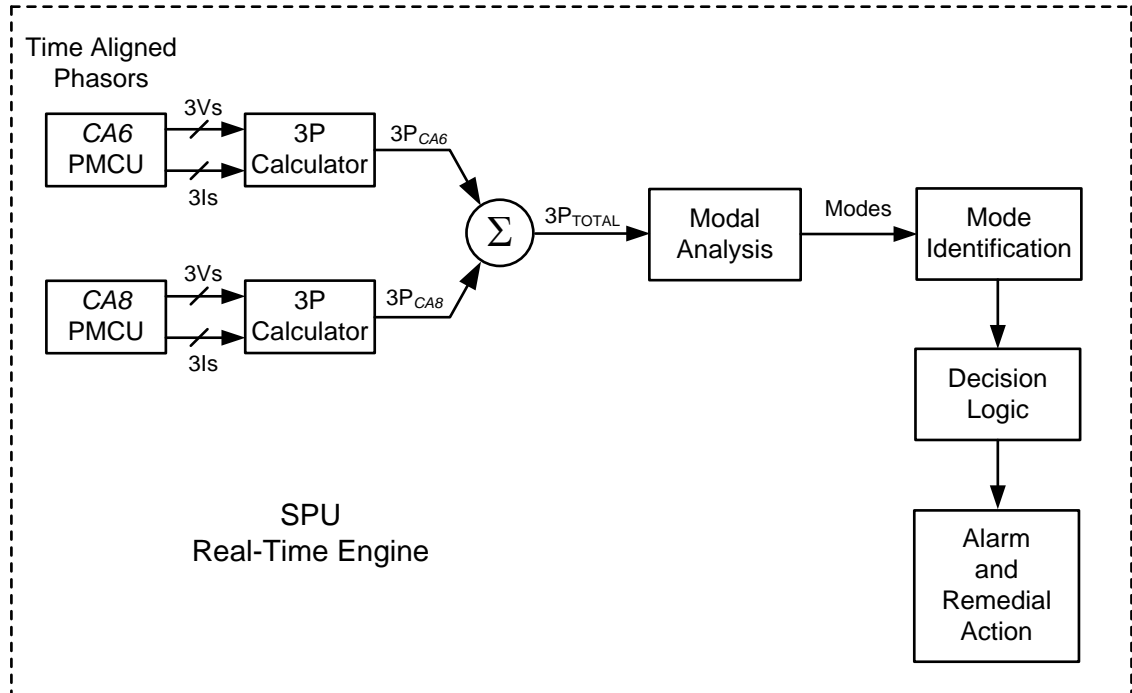
Figure 6.15   Algorithm of the SIPS to detect unstable active power oscillations and take remedial
actions.

To determine the band of frequencies of the inter-area oscillations of interest, the active power

threshold, and the damping ratio percentage threshold, the system recorded the voltage and current

synchrophasors of several inter-area power oscillation events such as the event shown in Figure 6.16.

From the figure, one can observe that the inter-area active power is greater than 70 MW, the

oscillation frequency is about 0.19 Hz, and the damping ratio is less than *5* percent. The figure also

shows the permanent existence of the local mode at about 5.1 Hz. Figure 6.17 shows the amplitudes

and frequencies of the local and inter-area modes before and during the inter-area power
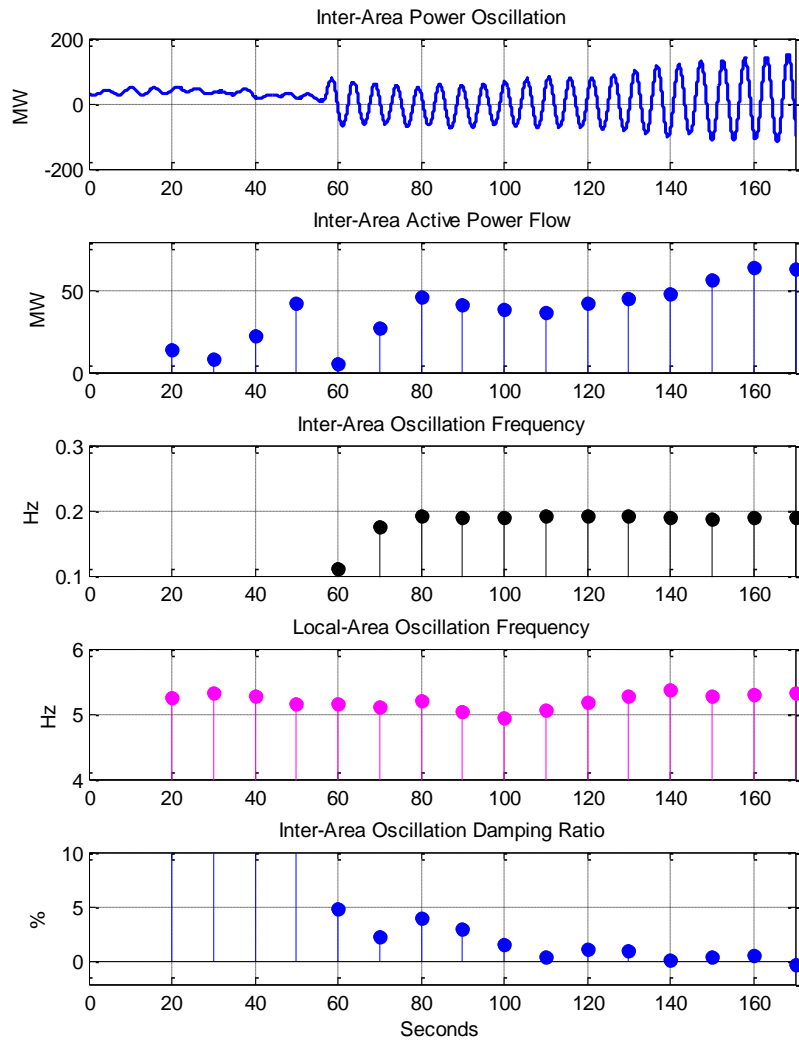
oscillations.

Figure 6.16   Unstable active power oscillation event provides information to configure the SIPS.
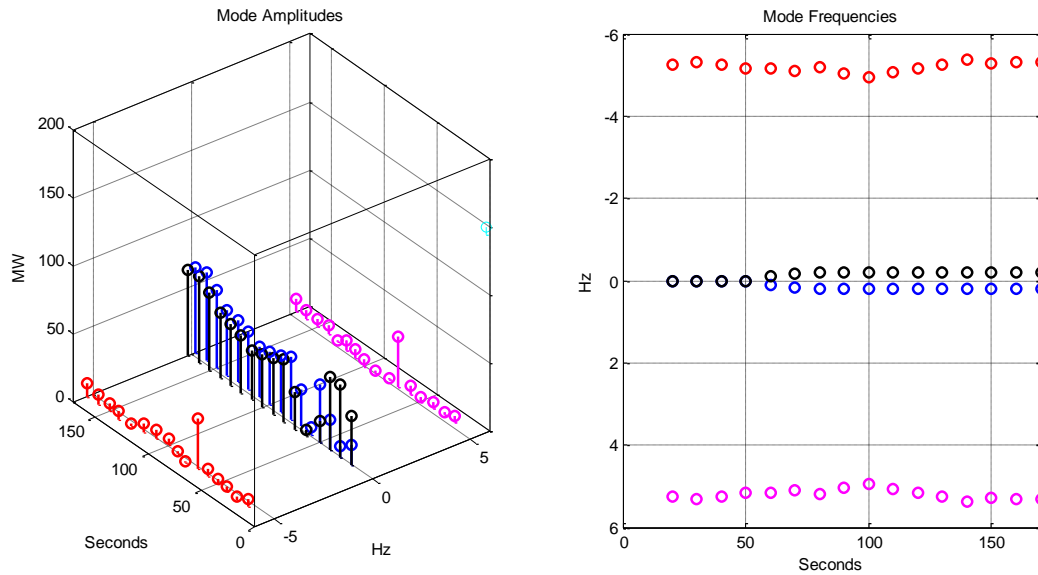
Figure 6.17   Amplitude of the local and inter-area modes before and during the inter-area power oscillations.

After the analysis of several field events such as the event shown in Figure 6.16, the following parameters were identified:

- The frequency band of interest from 0.1 to 0.3 Hz.
- The amplitude threshold of 70 MW.
- The damping ratio of 5 percent.

Figure 6.18 shows the MICL logic with the corresponding settings.
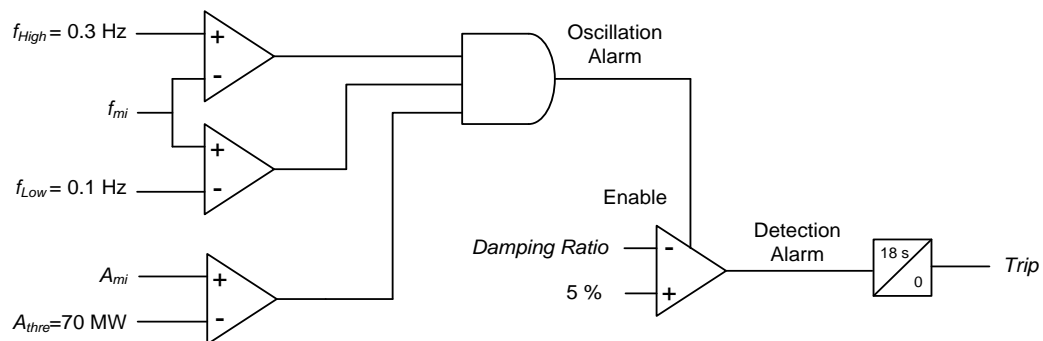
Figure 6.18   Configuration settings of the mode identification and under-damped oscillation detection logic.

6.4.2.3 SIPS Detects Inter-Area Power Oscillations

Shortly after the SIPS was in operation, it detected an inter-area active power oscillation event of 0.22 Hz. The oscillations started after part of the 230 kV was synchronized to the rest of the 230 kV network. Figure 6.19 shows the inter-area active power oscillations, the instant when the scheme detected the operation, and the activation of the trip command. Additionally, the figure shows the following:

- The inter-area power oscillation exceeding the 70 MW threshold.
- The power oscillation frequency inside the 0.1 - 0.3 Hz band.
- The damping ratio below 5 percent.
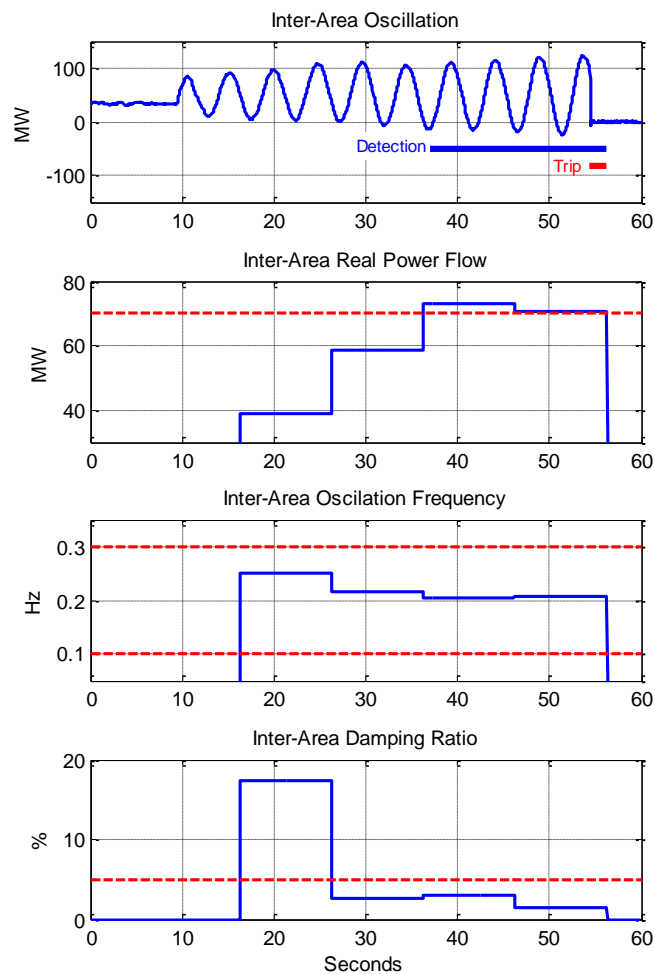
Figure 6.19   Under-damped active power oscillations and operation of the SIPS.

Figure 6.20 shows the active power through the *CA5-CA6* line before and after the remedial action and power system separation. After the remedial action, the oscillations quickly subside because this part of the 230 kV network remains connected to the strong 400 kV network. Figure 6.21 shows the frequencies of the two separated networks before and during the power oscillations and after the opening of the interconnection; notice that the two systems remained stable. The frequency of the strong system only drops 10 mHz to 60.09 Hz after the oscillations subside, and the frequency of the rest of the 230 kV network drops to 59.95 Hz. Also notice that the frequency of the strong system oscillates for approximately 10 cycles at 0.7 Hz after the isolation of the networks.
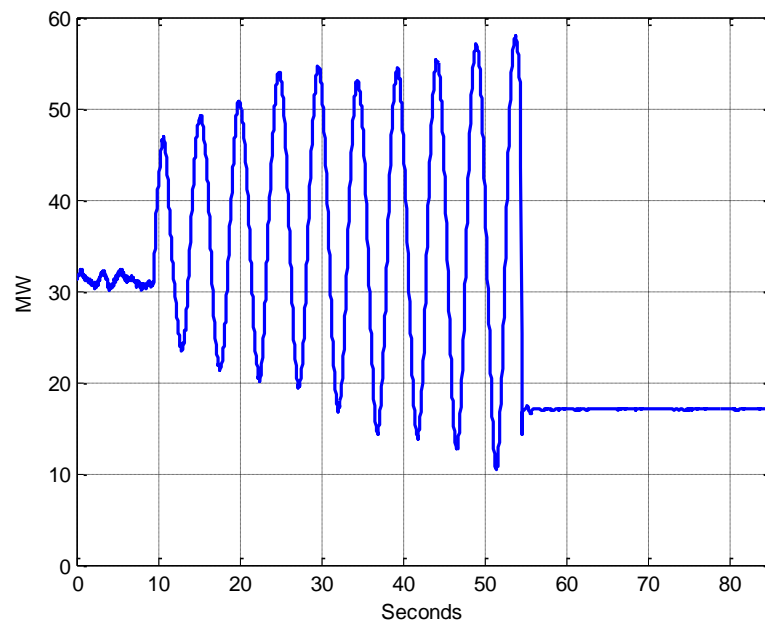
Figure 6.20   Active power flow through the *CA5-CA6* line before and after system separation.
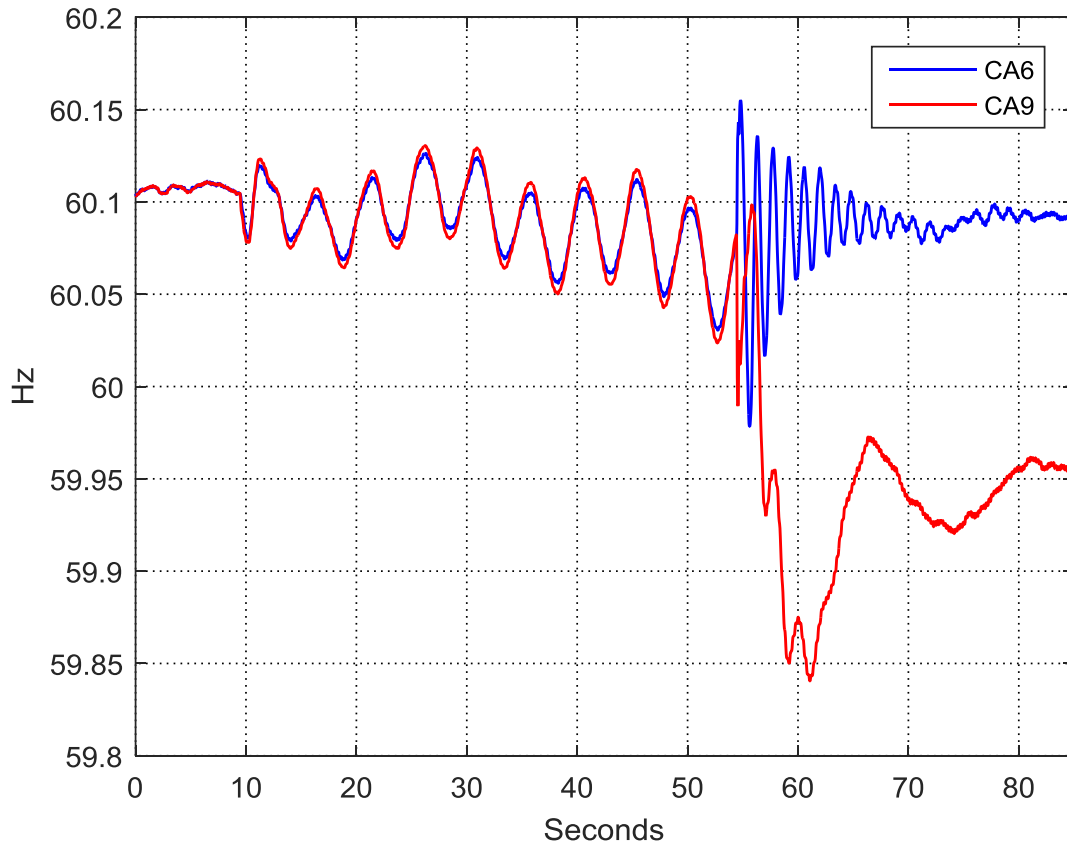
Figure 6.21   Frequencies of the separated networks before and after the remedial action.

6.5   Summary

The small signal generator models that are part of the overall power system model this chapter presents, generate signals to properly evaluate the performance of the Prony modal analysis method. It was shown that the estimated system characteristics match the analytically calculated characteristics presented in [68].

The Prony modal analysis method is an excellent tool for identifying power system dynamic characteristics. The Prony algorithm provides meaningful results when analyzing clean power system signals. Properly designed data acquisition and processing systems provide signals suitable for Prony modal analysis. The quadrature demodulation method with the filtering for 30 messages/s proposed in *Chapter 2* achieves the desired results for this application.

The proposed SIPS performs MA in real time, identifies inter-area power oscillations within the frequency band of interest, and takes a remedial action if the amplitude of the signal is greater than a predefined threshold and the damping ratio is lower than a predefined threshold for a predefined time.

The proposed SIPS has proven to be effective in a field application and has prevented power system collapse when inter-area power oscillations occur on multiple occasions, as described in [31]. This MA-based SIPS allows for optimizing the energy resources of the power system. Because of the success of the scheme described in this chapter, an additional transmission link was added to the original scheme.

Chapter 7 Conclusions and Future Work

7.1   Summary

This dissertation presents original concepts to implement efficient and reliable real-time wide-area synchrophasor-based protection and control applications. It provides implementation details of these applications and analyzes the performance of each of the applications by using computer simulations and field data. The objective of this work is to demonstrate the use of synchrophasor measurements and technology beyond visualization and post-mortem power system disturbance analysis.

As time keeping, communication network, and computing technologies advance, and as field experiences such as those this work presents demonstrate improvements in power system reliability and efficiency, real-time wide-area protection and control applications that use synchrophasors will become more common. These type of applications make synchrophasor technology an important part of the operation of modern power systems.

7.2   Conclusions and contributions

7.2.1   Synchrophasor Estimation

The quadrature demodulation method for synchrophasor estimation proposed in *Chapter 2* provides adequate performance for the real-time wide-area protection and control applications this work proposes. One of the objectives of this work is to point out that the DFT method to estimate synchrophasors, described in *Chapter 2*, is not suitable for SIPSs that detect inter-area oscillations. This application requires filtering with flat passband frequency response within a predetermined frequency range and heavy attenuation outside this frequency range.

The quadrature demodulation method, proposed in *Chapter 2*, is becoming popular for synchrophasor estimation and now is used as the basic synchrophasor estimation model included in the IEEE Std C37.118.1 [23]. This method allows tailoring of the total filter response to a particular application. Such an application might include, for example, fast response for fault protection or narrow frequency bandwidth for inter-area oscillation detection.

7.2.2   Phasor Data Concentration and Real-Time Processing

Devices that include phasor data concentration and real-time synchrophasor processing such as the PMCUs and SPUs described in *Chapters 3*, *4*, *5*, and *6* include PDC and command server functionality for implementing efficient and reliable SIPSs with minimum system components. The SPUs used in the proposed applications have a hard real-time operating system that runs the required tasks within a predetermined time interval. This capability allows the SPU to perform fast real-time calculations.

7.2.3   SIPSs Based on Synchrophasor Angle Difference

Chapter 3 proposed a SIPS that uses synchrophasor angle difference information to shed excess generation when the power transfer capability of the transmission network is reduced due to loss of key transmission lines. This SIPS uses the angle difference estimation to detect topology changes in the transmission network. The automatic generation-shedding scheme (AGSS) presented in *Chapter 3* requires only two voltage measurements and one communication channel for tripping the proper number of generators to maintain the proper generator-load balance and power system stability. Field tests for single contingencies validate the power system model used to estimate the angle difference for double contingencies. This SIPS has been efficiently implemented using only two PDC/PMCU as described in *Chapter 3*. This AGSS has been included in the paper *Using synchronized phasor angle difference for wide-area protection and control* [24], which was selected as the second best paper of the *Protection, Metering and Control Study Group*, CIGRÉ Brazil. The paper was published in the *EletroEvolução* magazine, Edition #55, July-2009 (published by CIGRÉ Brazil). This AGGS scheme is also included in [73, 74, 75].

7.2.4   Line Protection for Ground Faults Using Synchrophasors

Chapter 4 introduced algorithms that use time-synchronized local and remote negative-sequence and zero-sequence currents to detect ground faults in two terminal transmission lines. This algorithm has the following benefits:

- Uses only local and remote currents in its protection element characteristics.
- Provides backup line protection during loss-of-potential conditions.
- Detects high resistance faults without compromising faulted phase selectivity.
- Is immune to communication-channel delay asymmetry.

US Patent 8655608 [25] and the paper *Backup transmission line protection for ground faults and power swing detection using synchrophasors* [26] also provide information about this synchrophasor-based protection application. The description of this backup power line protection scheme is also included in the Negative- and Zero-Sequence Line Differential Protection section of the PSRC report *Use of Synchrophasor Measurements in Protective Relaying Applications* [74] and in [73].

7.2.5   Out-of-Step Power Swing Detection

Chapter 5 proposed a scheme that uses synchrophasor angle difference calculations together with their first and second derivatives to reliably detect out-of-step conditions in a two-area power system. This SIPS has the benefit of requiring minimum network topology information and being able to automatically adapt to changes in the operating conditions of the power system. The use of the first and second derivatives of the angle difference allows identification of out-of-step operating conditions before the system becomes unstable. The proposed out-of-step detection, power swing detection, and predictive out-of-step tripping algorithms are included in US Patent 7930117 *Systems and methods for power swing and out-of-step detection using time-stamped data* and in [29, 73]. Following are extensions of this work.

7.2.5.1 Early Prediction of Unstable Operating Conditions Minimize Load-Shedding Requirements

Franco et al. [76] studied the efficiency of the power system swing and out-of-step detection algorithms proposed in this dissertation by using a detailed dynamic model of an actual power system. The scheme operating time for the modeled contingencies show that load shedding and network separation can be achieved in 250 ms a time fast enough to maintain system stability. The simulation results were compared against traditional methods such as underfrequency load shedding and impedance-based OOST for activating load-shedding and network separation actions. The study shows that the underfrequency load-shedding scheme and the impedance-based OOST require 44 and 18 percent additional load shedding, respectively, to maintain system stability. The thesis [77] relating Franco's work on this topic was selected as the best masters thesis by the Uruguayan National Academy of Engineering in 2013.

7.2.5.2 Wide-Area, Synchrophasor-Based Islanding Detection Scheme

The two-area OOST detection scheme presented in *Chapter 5* is a fundamental component of the wide-area islanding detection scheme described in [78]. The OOST scheme has been complemented with the angle difference comparator shown in Figure 7.1 to detect slow slip frequencies that occur when power mismatch is minimal.
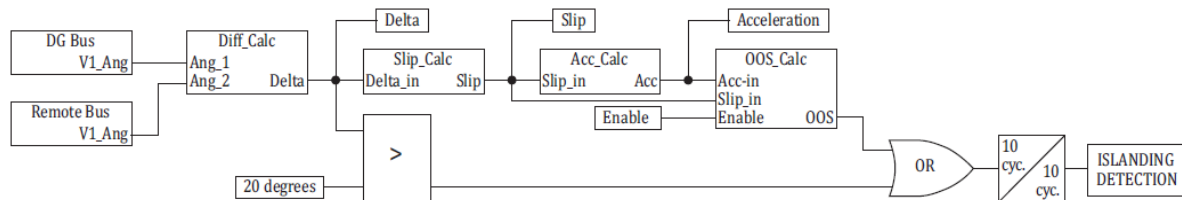
Figure 7.1   Implementation of the wide-area islanding detection scheme by using the power swing detection and angle difference schemes.

7.2.5.3 Improved Local Area Islanding Detection Scheme

Figure 7.2 shows a variation of the OOST characteristic through use of local frequency measurements for detecting islanding conditions [79]. The protective element that uses this characteristic compares the frequency deviation from nominal and the rate-of-change of frequency to quickly and securely

detect islanding conditions. This fast rate-of-change frequency element is faster than traditional frequency elements [78].
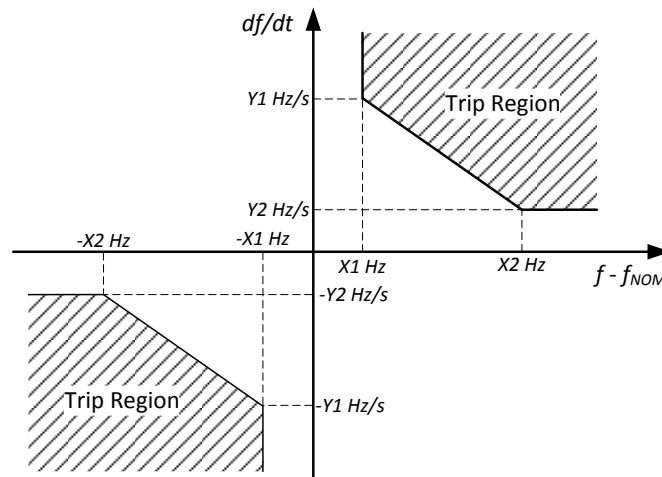
Figure 7.2   Local-area islanding detection element.

7.2.6   Detection of Inter-area Oscillations in Real Time

Chapter 6 proposed a SIPS based on real-time modal analysis; this real-time power system disturbance detection scheme has detected multiple inter-area oscillations in the field and prevented power system collapse on multiple occasions [31]. This scheme allows optimization of generation resources in the region. Because of the success of the scheme *Chapter 6* describes, an additional transmission link was added to the original scheme. The modified scheme adds the real powers of three transmission links and uses this total real power in the inter-area oscillation detection algorithm.

The December 2013 issue of *PACWorld* magazine included this synchrophasor application under the title *Wide-Area Protection and Control Scheme (Maintains Central America's Power System Stability)*. The PSRC report [74] and [73] also describe the proposed mode identification logic shown in Figure 6.12 for detecting inter-area oscillations.

7.3   Future Work

7.3.1   Reliable Time-Synchronization Reference

The synchrophasor technology for wide-area protection and control applications has many challenges to overcome. One of these challenges is the dependence on the time-synchronization signal from GPS. This dependence makes the use of synchrophasors a last resort for SIPS critical applications or relegates these schemes to redundant or backup protection applications. This dependence poses an application problem that needs to be addressed to improve SIPS reliability. One possible solution is to use promising technologies that provide a more reliable distribution of time references. These technologies combine multiple clocks and communication networks for terrestrial time distribution [80, 81]. Figure 7.3 shows one of these networks using the IEEE 1588 Precision Time Protocol. In these networks, the IEEE 1588 boundary clocks at Substations B, C, and D have two time reference options; the clocks include algorithms to select the most accurate time reference available in real time. Additionally, clock holdover times can be improved with atomic precision clocks built into GPS receivers to overcome vulnerabilities caused by temporary outages of the time reference signal [82]. Another possibility is to use clocks with multiple input sources from different Global Navigation Satellite Systems (GNSSs) such as GPS (USA), GLONASS (Russia), GALILEO (Europe), and BeiDou (China). The receiver can compare the different time outputs to determine if the time outputs are valid.
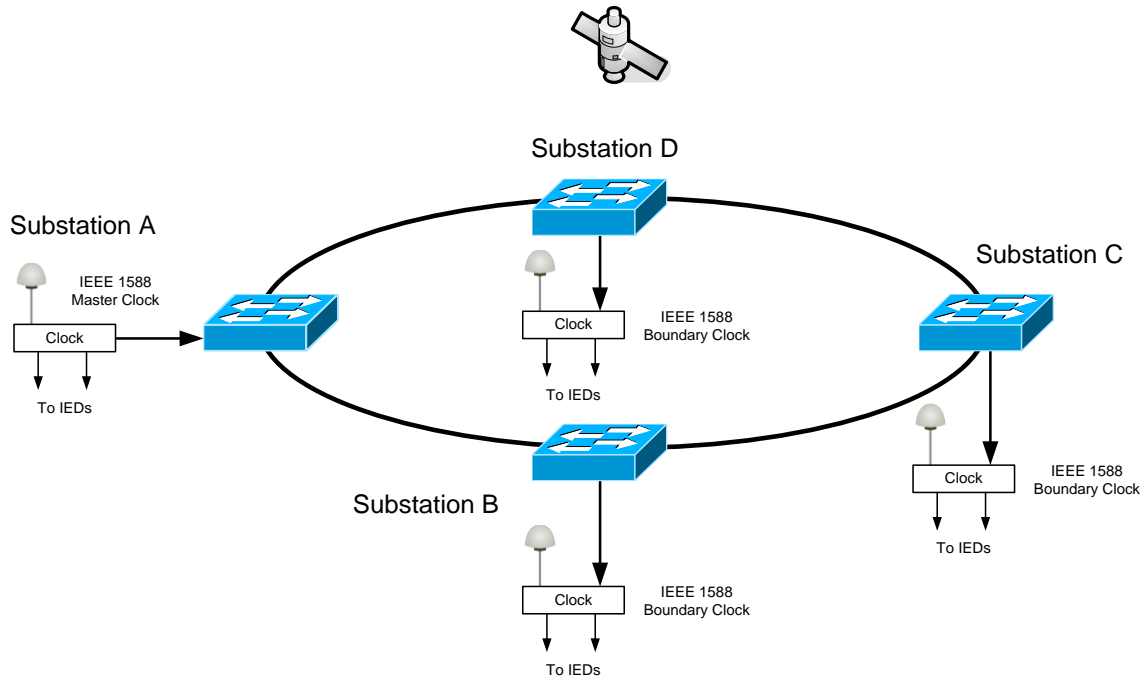
Figure 7.3   Time distribution using multiple clocks and terrestrial time distribution using IEEE 1588 Precision Time Protocol.

7.3.2   Synchrophasor Applications for Power System Fault Protection

Another challenge for synchrophasors is their application in high-speed fault protection schemes. To address this challenge, the latest version of the IEEE Std C37.118.1 [23] defines two filtering requirements: P for protection and M for metering. Presently, protection schemes are being developed using signal filtering techniques to reduce protection scheme operating times.

In *Chapter 4* , a backup transmission line protection scheme for power system faults was introduced. The operating times obtained with the proposed approach are in the order of 150 ms. For this reason, the scheme is used as backup protection. The operating times required for primary power system fault protection applications are in the order of 20 ms or less. To achieve faster operating times, the bandwidth requirements of the filtering process must be relaxed and the processing intervals must be reduced to protective relay processing rates (2 ms or less). Figure 7.4 shows the total frequency magnitude response of a filtering process that uses the quadrature demodulation method with a digital low-pass filter that has a rectangular window of 16 taps and sampling frequency of 960 Hz. Notice that this frequency response is similar to the response obtained with the DFT method described in *Chapter 2*. The corresponding step response of this filtering process is

depicted in Figure 7.5. This figure also includes the step response of the 60 message per second filter described in *Chapter 2* for comparison. The rise time to 90 percent of the final value is 15 ms for the filter with rectangular window and 44 ms for the filter with narrow bandwidth. The time response of the filtering process with rectangular window is suitable for fault protection. The operating times through the use of this filtering process are about 20 ms. Other approaches need to be investigated for obtaining faster protection. Synchrophasor filtering for fault protection applications is presently an area of study in power system protection.
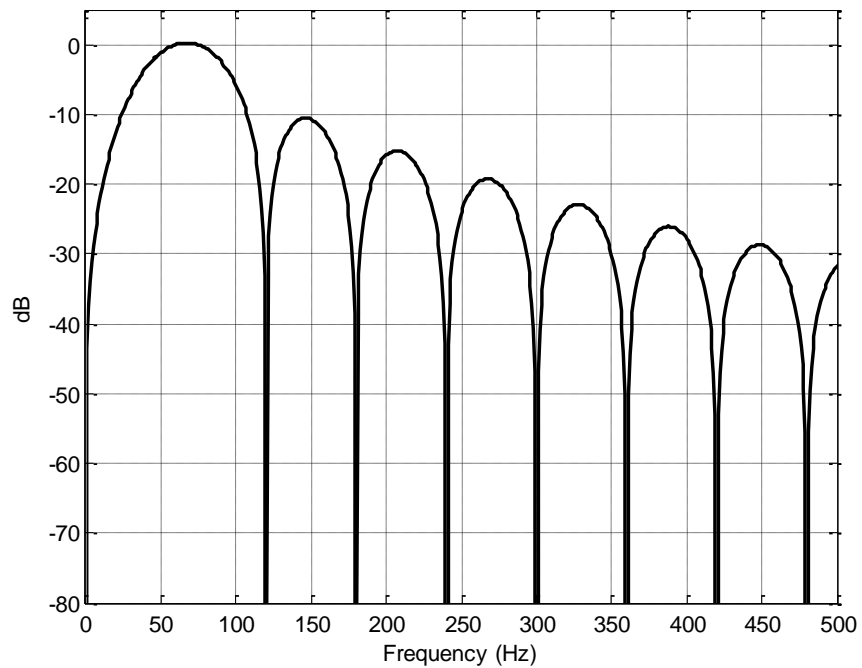
Figure 7.4   Total filtering magnitude frequency response when using the quadrature demodulation method with a one power system cycle rectangular window.
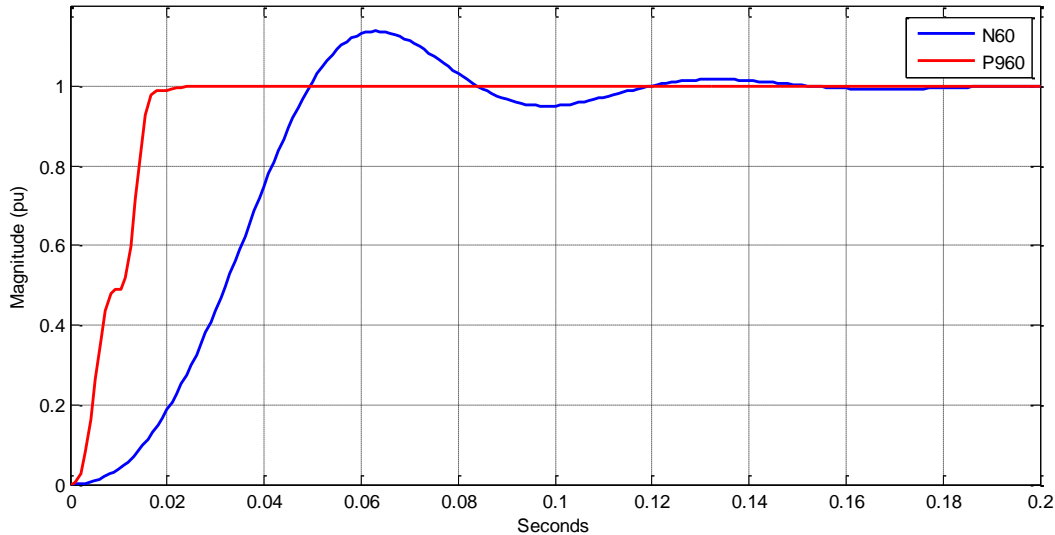
Figure 7.5   Step responses of the rectangular window (P960) and the narrow bandwidth (N60) filtering processes.

7.3.3   Real-Time Modal Analysis

One of the remaining challenges of the real-time modal analysis-based application described in *Chapter 6* is to identify what is causing the inter-area oscillations and eliminate the occurrence of these oscillations in the first place. A method for identifying the source of the power oscillations in real time through calculation of the direction of energy flow is described in [83]. Alternative approaches to achieve the same goal need to be investigated. Additionally, methods for detecting power system operating conditions that could evolve to inter-area oscillations are being investigated in the power industry and academia.

7.4   Final Remarks

The availability of synchrophasor measurements in devices such as protective relays, disturbance fault recorders, and meters, together with increased communication bandwidth and processor computing power contribute to fast deployment of synchrophasor technology. Synchrophasor and accurate time distribution technologies facilitate power system analysis and improve the reliability of SIPSs for preventing or minimizing power system disturbances and for improving the efficiency of the operation of the power system.

References

[1]   G. Missout and P. Girard, "Measurement of bus voltage angle between Montreal and Sept-Iles," *IEEE Transactions on power Apparatus and Systems, Vol. PAS-99, No. 2,* pp. 536-539, March/April 1980.

[2]   G. Missout, J. Beland, G. Bedard and Y. Lafleur, "Dynamic measurement of the absolute voltage angle on long transmission lines," *IEEE Transactions on Power Apparatus and Systems, Vol. PAS-100, No. 11,* pp. 4428-4434, November 1981.

[3]   P. Bonanomi, "Phase angle measurements with synchronized clocks – Principles and applications," *IEEE Transactions on Power Apparatus and Systems, Vol. PAS-100, No. 12,* pp. 5036-5043, December 1981.

[4]   R. O. Burnett, Jr., "Field experience with absolute time synchronism between remotely located fault recorders and sequence of events recorders," *IEEE Transactions on Power Apparatus and Systems, Vol. PAS-103, No. 7,* pp. 1739-1742, July 1984.

[5]   J. S. Thorp, A. G. Phadke, S. H. Horowitz and M. M. Begovic, "Some applications of phasor measurements to adaptive protection," *IEEE Transactions on Power Systems, Vol. 3, No. 2,* May 1988.

[6]   A. G. Phadke, Computer Relaying for Power Systems, Taunton, Sommerset, England: Research Studies Press Ltd., 1988.

[7] A. G. Phadke and J. S. Thorp, "Improved power system protection and control through synchronized phasor measurements," in *Proceedings of the 6th National Conference*, Bombay, India, 1990.

[8] R. E. Wilson, "Methods and uses of precise time in power systems," *IEEE Transactions on Power Delivery, Vol. 7, No. 1,* pp. 126-132, January 1992.

[9] D. Novosel, V. Madani, B. Bhargava, Khoi Vu and J. Cole, "Down of the grid synchronization," *IEEE Power and Energy Magazine, Vol. 6, No. 1,* pp. 49-60, 2008.

[10] C. W. Taylor, D. C. Erickson, K. E. Martin and R. E. Wilson, "WACS-Wide-Area Stability and Voltage Control System: R&D and online demonstration," *IEEE Energy Infrastructure Defense Systems, Vol. 93, No. 5,* pp. 892-906, May 2005.

[11] J. León, A. Jarquín, E. Mora and E. Godoy, "Reliability analysis for a generation shedding scheme on the CFE main transmission network," in *29th Annual Western Protective Relay Conference*, Spokane, WA, USA, 2002.

[12] J. F. Hauer, C. J. Demeure and L. L. Scharf, "Initial results in Prony analysis of power system response signals," *IEEE Transactions on Power Systems, Vol. 5, No. 1,* pp. 80-89, February 1990.

[13] D. J. Trudnowski, J. W. Pierre, N. Zhou, J. F. Hauer and M. Parashar, "Performance of three mode-meter block-processing," *IEEE Transactions on Power Systems, Vol. 23, No. 2,* pp. 680-690, May 2008.

[14] A. Argaval, J. Balance, B. Bhargava, J. Dyer, K. Martin and J. Mo, "Real Time Dynamics Monitoring System (RTDMS®) for use with synchrophasor technology in power systems," in *IEEE Power and Energy Society General Meeting*, San Diego, CA, 2011.

[15] P. Denys, C. Counan, L. Hossenlopp and C. Holweck, "Measurement of voltage phase for the French future defence plan against losses of synchronism," *IEEE Transactions on Power Delivery, Vol. 7, No. 1,* January 1992.

[16] Y. Ohura, K. Matsuzawa, H. Ohtsuka, N. Nagai, T. Gouda, H. Oshida, S. Takeda and S. Nishida, "Develpoment of a generator tripping system for transient stability augmentation based on the energy function method," *IEEE Transactions on Power Delivery, Vol. PWRD-1, No. 3,* pp. 68-77, July 1986.

[17] E. O. Schweitzer III, T. T. Newton and R. A. Baker, "Power swing relay also records disturbances," in *13th Annual Western Protective Relay Conference Proceedings*, Spokane, WA, 1986.

[18] Y. Ohura, M. Suzuki, K. Yanagihashi, M. Yamaura, K. Omata and T. Nakamura, "A predictive out-of-step protection system based on observation of the phase difference between substations," *IEEE Transactions on Power Delivery, Vol. 5, No. 4,* November 1990.

[19] V. Centeno, J. De La Ree, A. G. Phadke, G. Mitchell, R. J. Murphy and R. O. Burnett Jr., "Adaptive out-of-step relaying using phasor measurement techniques," *IEEE Computer Applications in Power, Vol. 6, No. 4,* October 1993.

[20] V. Centeno, A. G. Phadke, A. Edris, J. Benton, M. Gaudi and G. Michel, "An adaptive out-of-step relay," *IEEE Transactions on Power Delivery, Vol. 12, No. 1,* January 1997.

[21] Task Force on Identification of Electromechanical Modes of the Power System Stability Subcommittee, "Identification of Electromechanical Modes in Power Systems," IEEE, 2012.

[22] A. Guzmán, S. Samineni and M. Bryson, "Protective relay synchrophasor measurements under fault conditions," in *32nd Annual Western Protective Relay Conference*, Spokane, WA, USA, 2005.

[23] *IEEE Standard for Synchrophasor Measurements for Power Systems, IEEE Std C37.118.1-2011.*

[24] E. Martínez, N. Juárez, A. Guzmán, G. Zweigle and J. León, "Using synchronized phasor angle difference for wide-area protection and control," in *33rd Annual Western Protective Relay Conference*, Sopokane, WA, 2006.

[25] A. Guzmán-Casillas, "Symmetrical component amplitude and phase comparators for line protection using time stamped data". US Patent 8655608, 18 February 2014.

[26] A. Guzmán, V. Mynam and G. Zweigle, "Backup transmission line protection for ground faults and power swing detection using synchrophasors," in *34th Annual Western Protective Relay Conference*, Spokane, WA, USA, 2007.

[27] E. O. Schweitzer III, D. E. Whitehead, A. Guzmán, Y. Gong and M. Donolo, "Advanced real-time synchrophasor applications," in *35th Annual Western Protective Relay Conference*, Spokane, WA, 2008.

[28] A. Guzmán-Casillas, "Systems and methods for power swing and out-of-step detection using time-stamped data". US Patent 7930117, 19 April 2011.

[29] E. O. Schweitzer III and A. Guzmán, "Synchrophasor processor detects out-of-step conditions," in *IEEE Smart Grid Communications (SmartGridComm)*, Brussels, Belgium, 2011.

[30] Y. Gong and A. Guzmán-Casillas, "Real-time power system oscillation detection using modal analysis". US Patent 7987059, 26 July 2011.

[31] J. V. Espinoza, A. Guzmán, F. Calero, V. Mynam and E. Palma, "Wide-area protection and control scheme mantains Central America's power system stability," in *39th Annual Western Protective Relay Conference Proceedings*, Spokane, WA, USA, 2012.

[32] C. P. Steinmetz, "Complex quantities and their use in electrical engineering," in *AIEE Proceedings of the International Electrical Congress*, Chicago, IL, USA, 1893.

[33] J. A. Edminister, Theory and Problems of Electric Circuits 2nd Edition, New York: McGraw-Hill, 1983.

[34] *IRIG Standard 200-04. "IRIG Standard Time Formats," Telecommunications Working Group, Inter-Range Instrumentation Group, Range Commanders Council,* 2004.

[35] G. Benmouyal, E. O. Schweitzer III and A. Guzmán, "Synchronized phasor measurement in protective relays for protection, control, and analysis of electric power systems," in *29th Annual Western Protective Relay Conference*, Spokane, WA, USA, 2002.

[36] A. G. Phadke, "Synchronized sampling and phasor measurements for relaying and control," *IEEE Transactions on Power Delivery, Vol. 9, No. 1,* January 1994.

[37] K. Behrendt and K. Fodero, "The perfect time: An examination of time-synchronization techniques," in *60th Annual Georgia Tech Protective Relay Conference*, Atlanta. GA, USA, 2006.

[38] E. O. Brigham, The Fast Fourier Transform, Englewood Cliffs, NJ, USA: Prentice Hall, Inc., 1974.

[39] A. G. Phadke, J. S. Thorp and M. G. Adamiak, "A new measurement technique for tracking voltage phasors, local system frequency, and rate of change of frequency," *IEEE Transactions on Power Apparatus and Systems, Vol. PAS-102, No. 5,* May 1983.

[40] A. G. Phadke and J. S. Thorp, Synchronized Phasor Measurements and Their Applications, New York, NY: Springer Science+Business Media, LLC, 2008.

[41] D. E. Simon, An Embedded Software Primer, Boston, MA, USA: Addison-Wesley, 1999.

[42] L. H. Fink and K. Carlsen, "Operating under stress and strain," *IEEE Spectrum, Vol. 15,* pp. 48-53, March 1978.

[43] A. Guzmán, "Power system reliability using multifunction protective relays," *Power Transmission and Distribution,* pp. 56-58, June/July 2004.

[44] A. Guzmán, J. B. Mooney, G. Benmouyal and N. Fischer, "Transmission line protection system for increasing power system requirements," in *55th Annual Conference for Protective Relay Engineers*, College Station, TX, USA, 2002.

[45] T. F. 38.02.19, "System Protection Schemes in Power Networks, No. 187," CIGRE, June, 2001.

[46] C. W. Taylor, Power System Voltage Stability, EPRI McGraw-Hill International Edition, 1994.

[47] M. Begovic, D. Fulton, M. R. Gonzalez, J. Goossens, E. A. Guro, R. W. Haas, C. F. Henville, G. Manchur, G. L. Michel, R. C. Pastore, J. Postforoosh, G. L. Schmitt, J. B. Williams and K. Zimmerman, "Summary of system protection and voltage stability," *IEEE Transactions on Power Delivery, Vol. 10, No. 2,* pp. 631-638, April 1995.

[48] G. C. Bullock, "Cascading voltage collapse in West Tennessee," in *17th Annual Western Protective Relay Conference*, Spokane, WA, USA, 1990.

[49] C. W. Taylor and R. E. Wilson, "BPA's wide-area stability and voltage control (WACS): Overview and large-scale simulations," in *Proc. IX Symposium of Specialists in Electric Operational and Expansion Planning (IX SEPOPE)*, Rio de Janero, Brazil, 2004.

[50] A. Guzmán, D. Tziouvaras, E. O. Schweitzer and K. E. Martin, "Local and wide-area network protection systems improve power system reliability," in *31st Annual Western Protecive Relay Conference*, Spokane, WA, 2004.

[51] *IEEE Standard for Synchrophasor Data Transfer for Power Systems, IEEE Std C37.118.2-2011.*

[52] G. C. Zweigle, A. Guzmán, C. E. Petras and P. Jiang, "Apparatus, method, and system for wide-area protection and control using power system data having a time component associated therewith". US Patent 7630863, 8 December 2009.

[53] E. O. Schweitzer III, A. Guzmán, H. J. Altuve, D. A. Tziouvaras and J. Needs, "Real-time synchrophasor applications in power system control and protection," in *Developments in Power System Protection (DPSP 2010). Managing the Change, 10th IET*, Manchester, UK, 2010.

[54] E. O. Schweitzer III, L. S. Anderson, A. Guzmán-Casillas, G. C. Zweigle and G. Benmouyal, "Protective relay with synchronized phasor measurement capabiltiy for use in electric power systems". US Patent 6662124, 18 January 2005.

[55] E. O. Schweitzer III and J. B. Roberts, "Distance relay element design," in *19th Annual Western Protective Relay Conference Proceedings*, Spokane, WA, USA, 1992.

[56] J. B. Roberts and D. Tziouvaras, "Fault type selection system for identifying faults in an electric power system". US Patent 6525543, 25 February 2003.

[57] J. B. Roberts, D. A. Tziouvaras, G. Benmouyal and H. J. Altuve, "The effect of multiprinciple line protection on dependability and security," in *55th Annual Georgia Tech Protective Relay Conference*, Atlanta, GA, USA, 2001.

[58] A. R. v. C. Warrington, Protective Relays: Their Theory and Practice, Vol. 1, London: Chapman and Hall, 1974.

[59] F. Calero and W. A. Elmore, "Current differential and phase comparison relaying schemes," in *19th Annual Western Protective Relay Conference Proceedings*, Spokane,WA, USA, 1992.

[60] K. C. Behrendt, "Relay-to-relay digital logic communication for line protection, monitoring, and control," in *51st Annual Georgia Tech Protective Relaying Conference Proceedings*, Atlanta, GA, USA, 1997.

[61] G. Benmouyal, "The trajectories of line current differential faults in the alpha plane," in *32nd Annual Western Protective Relay Conference Proceedings*, Spokane, WA, USA, 2005.

[62] E. Clarke, Circuit Analysis of AC Power Systems, Vol. 2, New York: Wiley and Sons, 1950.

[63] M. McDonald and D. Tziouvaras, "Power swing and out-of-step considerations on transmision lines," IEEE Power Systems Relay Committee WG D6, 2005.

[64] W. D. Stevenson, Elements of Power System Analysis. 3rd Edition, McGraw-Hill Kogakusha, 1975.

[65] J. F. Hauer, M. J. Beshir and W. A. Mittelstadt, "Dynamic performance validation in the Western power system," in *APEx 2000*, Kananaskis, Alberta, Canada, 2000.

[66] J. F. Hauer, "Application of Prony analysis in the determination of modal content and equivalent models for measured power system response," *IEEE Transactions on Power Systems, Vol. 6, No. 3,* pp. 1062-1068, August 1991.

[67] Y. Gong and A. Guzmán, "Synchrophasor-based online modal analysis to mitigate power system interarea oscillation," in *DistribuTECH Conference and Exhibition*, San Diego, CA, USA, 2009.

[68] P. Kundur, Power System Stability and Control, New York: McGraw-Hill, 1994.

[69] F. P. Demello and C. Concordia, "Concepts of synchronous machine stability as affected by excitation control," *IEEE Transactions on Power Apparatus and Systems, Vol. PAS-88, No. 4,* pp. 316-328, April 1969.

[70] W. G. Heffron and R. A. Phillips, "Effect of a modern amplidyne voltage regulator on underexited operation of large turbine generators," *AIEE Transactions on Power Apparatus and Systems, No. PAS-71 ,* pp. 692-697, August 1952.

[71] R. Prony, "Essai expérimental et analytique sur les lois de la dilatabilité des fluides élastiques et sur celles de la force expansive de la vapeur de l'eau et de la vapeur de l'alkool, à différentes températures," *Journal de l'Ecole Polytechnique (Paris), Vol. 1,* pp. 24-76, 1795.

[72] M. Klein, G. J. Rogers and P. Kundur, "A fundamental study of inter-area oscillations in power systems," *IEEE Transactions on Power Systems, Vol. 6, No. 3,* pp. 914–921, August 1991.

[73] H. J. Altuve-Ferrer and E. O. Schweitzer III, Modern Solutions for Protection, Control, and Monitoring of Electric Power Systems, Pullman, WA, USA: Schweitzer Engineering Laboratories, Inc., 2010.

[74] J. O'Brien, "Use of synchrophasor measurements in protective relaying applications," IEEE Power System Relaying Committee WG C-14, 2014.

[75] V. Terzija, "Wide Area Protection and Control Technologies," CIGRE WG B5.14, to be published.

[76] R. Franco, C. Sena, G. N. Taranto and A. Giusto, "Using synchrophasors for controlled islanding - A prospective application for the Uruguayan power system," *IEEE Transactions on Power Systems, Vol. 28, No. 2,* May 2013.

[77] R. Franco, Uso de sincrofasores para la detección de oscilaciones de potencia y pérdida de sincronismo. Aplicación al sistema eléctrico Uruguayo para la separación controlada en islas, Montevideo, Uruguay: ISSN 1688-2806, 2012.

[78] J. Mulhausen, J. Schaefer, M. Mynam, A. Guzmán and M. Donolo, "Anti-islanding today, successful islanding in the future," in *36th Annual Western Protective*, Spokane, WA, USA, 2009.

[79] A. Guzmán-Casillas, M. V. Mynam and M. A. Donolo, "Islanding detection in an electrical power delivery system". US Patent 8346402, 1 January 2013.

[80] *IEEE Standard for a Precision Clock Synchronization Protocol for Networked Measurements and Control Systems, IEEE Std. 1588-2008.*

[81] K. Fodero, C. Huntley and D. Whitehead, "Secure, wide-area time synchronization," in *12th Annual Western Power Delivery Automation Conference*, Spokane, WA, USA, 2010.

[82] F. Chan, M. Joerger and B. Pervan, "Stochastic modeling of atomic receiver clock for high integrity navigation," *IEEE Transactions on Areospace and Electronic Systems, Vol. 50, No. 3,* pp. 1749-1764, 2014.

[83] D. Yang, J. Li, H. Xu and C. Luo, "Method for determining position of forced power oscillation disturbance source in regional interconnected power grid". US Patent 2014/034369 A1, 30 October 2014.

[84] J. W. H. Hayt and J. E. Kemmerly, Engineering Circuit Analysis, 2nd Edition, Tokyo, Japan: Mc Graw-Hill Kogakusha, Ltd., 1971.

[85] *IEC Programmable Controllers Part 3 Programming Language, IEC-61131-3 Standard. 2nd Edition,* 2003-01.

[86] S. L. Marple, Digital Spectral Analysis with Applications, Englewood Cliffs, NJ: Prentice-Hall Inc., 1987.

[87] F. B. Hildebrand, Introduction to Numerical Analysis, New York: McGraw-Hill, 1956.

Appendix A Phasor Estimation Using Discrete Fourier Transform

The Discrete Fourier Transform (DFT) is used to estimate phasors in many electrical engineering applications. Phasors represent sinusoidal voltage or current signals that are defined according to (A.1) and illustrated in Figure A.1 [33, 84]. The sinusoidal signal *x(t)* can be expressed in complex form using (A.2) [32].

$$x(t) = X_{pk} \bullet \cos(\omega \bullet t + \phi) \tag{A.1}$$

where:

X_{pk} is the amplitude of the signal *x(t)*,

ω is the frequency in radians per second,

ϕ is the phase angle in radians.

$$x(t) = \sqrt{2}\,\text{Re}\left(\frac{X_{pk}}{\sqrt{2}} e^{i\omega t} e^{i\phi} \right) \tag{A.2}$$
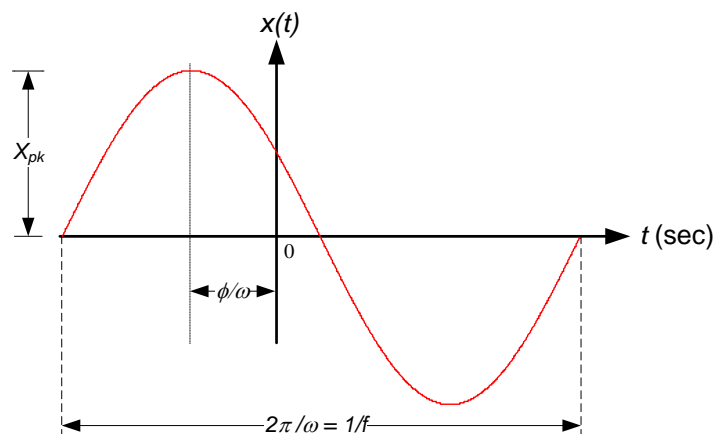
Figure A.1   Sinusoidal voltage signal *x(t)* with amplitude, X_{pk} , phase angle, ϕ , and frequency ω.

In steady state, the only quantities in (A.2) that provide information are X_{pk} and ϕ. Therefore, the phasor X (A.3) represents $x(t)$ in steady state.

$$X = \frac{X_{pk}}{\sqrt{2}} e^{i\phi} \tag{A.3}$$

In (A.4) and (A.5), $x(t)$ is expressed as a function of the phasor X.

$$x(t) = \sqrt{2}\,\mathrm{Re}\left(Xe^{i\omega t}\right) \tag{A.4}$$

$$x(t) = \frac{1}{\sqrt{2}}\left(Xe^{i\omega t} + \overline{X}e^{-i\omega t}\right) \tag{A.5}$$

Equation (A.6) shows the discrete form x_k that represents $x(t)$ sampled at Δt intervals. The sampling rate f_s is the multiplicative inverse of the processing interval Δt.

$$x_k = \frac{1}{\sqrt{2}}\left(Xe^{ik\omega\Delta t} + \overline{X}e^{-ik\omega\Delta t}\right) \tag{A.6}$$

The nominal frequency $(\omega_0 = 2\pi f_0)$ phasor χ_r is obtained by using the DFT with an observation window of N samples as expressed in (A.7) and (A.8). In these equations, r corresponds to the initial sample of the observation window [40]. The ½ factor creates coefficients with central symmetry.

$$\chi_r = \frac{1}{\sqrt{2}}\frac{2}{N}\sum_{k=r}^{r+N-1} x_k e^{-i(k+1/2)\omega_0\Delta t} \tag{A.7}$$

$$\chi_r = \frac{\sqrt{2}}{N}\sum_{k=r}^{r+N-1} x_k e^{-i(k+1/2)\omega_0\Delta t} \tag{A.8}$$

Equation (A.9) expresses Δt in terms of the nominal frequency f_0 and N.

$$\Delta t = \frac{1}{f_s} = \frac{2\pi}{N\omega_0} = \frac{1}{Nf_0} \tag{A.9}$$

By substitution of (A.6) in (A.8), the nominal frequency phasor χ_r can be stated in terms of X (A.10).

$$\chi_r = \frac{1}{N}\sum_{k=r}^{r+N-1}\left(Xe^{ik\omega\Delta t} + \overline{X}e^{-ik\omega\Delta t}\right)e^{-i(k+1/2)\omega_0\Delta t} \tag{A.10}$$

After the multiplication of the exponential terms that are function of ω with the exponential term that is function of ω_0, the resulting χ_r expression consists of the frequency difference $(\omega - \omega_0)$ and the frequency sum $(\omega + \omega_0)$ components. In (A.11), the first term corresponds to the frequency difference χ_{r_DIF} component and the second term χ_{r_SUM} corresponds to the frequency sum component.

$$\chi_r = \frac{1}{N}\sum_{k=r}^{r+N-1}Xe^{i(k+1/2)(\omega-\omega_0)\Delta t} + \frac{1}{N}\sum_{k=r}^{r+N-1}\overline{X}e^{-i(k+1/2)(\omega+\omega_0)\Delta t} = \chi_{r\_DIF} + \chi_{r\_SUM} \tag{A.11}$$

Next, the phasor χ_r is estimated at the $r+N-1$ sample where r is the initial sample, ϕ is the phase angle, ω is the operating frequency, and ω_0 is the nominal frequency. Equation (A.12) corresponds to χ_{r_DIF}, where the constant term is outside of the summation term.

$$\chi_{r\_DIF} = \frac{1}{N}\sum_{k=r}^{r+N-1}Xe^{i(k+1/2)(\omega-\omega_0)\Delta t} = \frac{1}{N}Xe^{i(r+1/2)(\omega-\omega_0)\Delta t}\sum_{k=0}^{N-1}e^{ik(\omega-\omega_0)\Delta t} \tag{A.12}$$

The generic expression developed in *Appendix B* is used to express the sum from $k = 0$ to $k = N-1$ — in (A.12) — in terms of sine and exponential functions according to (A.13) and (A.14).

$$\chi_{r\_DIF} = Xe^{i(r+1/2)(\omega-\omega_0)\Delta t}\frac{\sin\left[\dfrac{N(\omega-\omega_0)\Delta t}{2}\right]}{N\sin\left[\dfrac{(\omega-\omega_0)\Delta t}{2}\right]}e^{i(N-1)\frac{(\omega-\omega_0)\Delta t}{2}} \tag{A.13}$$

$$\chi_{r\_DIF} = Xe^{i(r+1/2)\frac{2\pi}{N}\frac{f-f_0}{f_0}}\frac{\sin\left[\pi\dfrac{f-f_0}{f_0}\right]}{N\sin\left[\pi\dfrac{f-f_0}{Nf_0}\right]}e^{i\pi\frac{N-1}{N}\frac{f-f_0}{f_0}} \tag{A.14}$$

In (A.16), the expression for χ_{r_DIF} is simplified using $\Pi_{DIF}(f)$ from (A.15).

$$\Pi_{DIF}(f) = \pi \frac{f - f_0}{f_0} \tag{A.15}$$

$$\chi_{r\_DIF} = \overline{X} e^{i \frac{\Pi_{DIF}(f)}{N}[2(r+1/2)+N-1]} \frac{\sin[\Pi_{DIF}(f)]}{N \sin\left[\frac{\Pi_{DIF}(f)}{N}\right]} \tag{A.16}$$

Then in (A.17), X is substituted according to (A.3) for obtaining the expression of χ_{r_DIF} as a function of X_{pk} and ϕ.

$$\chi_{r\_DIF}(r,f,\phi) = \frac{X_{pk}}{\sqrt{2}} e^{i\phi} e^{i \frac{\Pi_{DIF}(f)}{N}[2(r+1/2)+N-1]} \frac{\sin[\Pi_{DIF}(f)]}{N \sin\left[\frac{\Pi_{DIF}(f)}{N}\right]} \tag{A.17}$$

In similar manner, Equation (A.18) corresponds to χ_{r_SUM}.

$$\chi_{r\_SUM} = \frac{1}{N} \sum_{k=r}^{r+N-1} \overline{X} e^{-i(k+1/2)(\omega+\omega_0)\Delta t} = \frac{1}{N} \overline{X} e^{-i(r+1/2)(\omega+\omega_0)\Delta t} \sum_{k=0}^{N-1} e^{-ik(\omega+\omega_0)\Delta t} \tag{A.18}$$

Equations (A.19) and (A.20) express the sum from $k = 0$ to $k = N-1$ — in (A.18) — in terms of sine and exponential functions.

$$\chi_{r\_SUM} = \overline{X} e^{-i(r+1/2)(\omega+\omega_0)\Delta t} \frac{\sin\left[\frac{N(\omega+\omega_0)\Delta t}{2}\right]}{N \sin\left[\frac{(\omega+\omega_0)\Delta t}{2}\right]} e^{-i(N-1)\frac{(\omega+\omega_0)\Delta t}{2}} \tag{A.19}$$

$$\chi_{r\_SUM} = \overline{X} e^{-i(r+1/2)\frac{2\pi}{N}\frac{f+f_0}{f_0}} \frac{\sin\left[\pi \frac{f+f_0}{f_0}\right]}{N \sin\left[\pi \frac{f+f_0}{Nf_0}\right]} e^{-i\pi \frac{N-1}{N}\frac{f+f_0}{f_0}} \tag{A.20}$$

In (A.22), the expression for χ_{r_SUM} is simplified using $\Pi_{SUM}(f)$ from (A.21).

$$\Pi_{SUM}(f) = \pi \frac{f + f_0}{f_0} \tag{A.21}$$

$$\chi_{r\_SUM} = \overline{X}e^{-i\frac{\Pi_{SUM}(f)}{N}[2(r+1/2)+N-1]} \frac{\sin[\Pi_{SUM}(f)]}{N\sin\left[\dfrac{\Pi_{SUM}(f)}{N}\right]} \tag{A.22}$$

Then in (A.23), X is substituted according to (A.3) for obtaining the expression of χ_{r_SUM} as function of X_{pk} and ϕ.

$$\chi_{r\_SUM}(r,f,\phi) = \frac{X_{pk}}{\sqrt{2}}e^{-j\phi}e^{-i\frac{\Pi_{SUM}(f)}{N}[2(r+1/2)+N-1]} \frac{\sin[\Pi_{SUM}(f)]}{N\sin\left[\dfrac{\Pi_{SUM}(f)}{N}\right]} \tag{A.23}$$

Finally, the simplified expression (A.24) defines the phasor as a function of r, f, and ϕ.

$$\chi_r(r,f,\phi) = \chi_{r\_DIF}(r,f,\phi) + \chi_{r\_SUM}(r,f,\phi) \tag{A.24}$$

Figure A.2 shows the phasor calculations using (A.24) for 30, 45, 60, 75, and 90 Hz with $N = 32$, $r = 0$, and $0 \le \phi \le 360°$ (*Appendices C* and *D* include the Mathcad® and MATLAB® scripts that generate this figure). The phasors that correspond to $f = 60$ Hz plot a circle with constant magnitude while the phasors for the off nominal frequencies plot ellipses with variable magnitude. The elliptical plots are caused by phase angle and magnitude errors. These errors need to be compensated according to the frequency deviation from nominal for accurate phasor estimation from a single phase quantity (e.g. A-phase voltage).
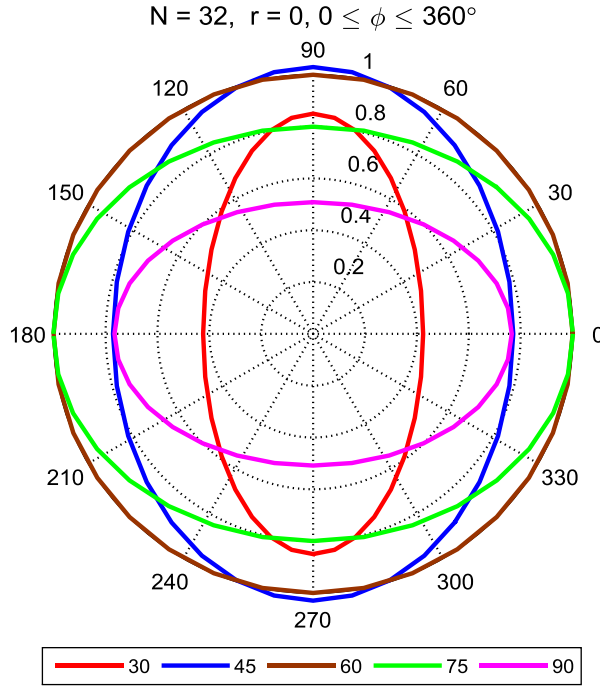
Figure A.2   Phasor estimations at 30, 45, 60, 75, and 90 Hz

Equation (A.25) determines the magnitude error in (A.17) , and (A.26) determines the corresponding magnitude error in (A.23).

$$M_{DIF} = \frac{\sin\left[\Pi_{DIF}(f)\right]}{N\sin\left[\dfrac{\Pi_{DIF}(f)}{N}\right]} \tag{A.25}$$

$$M_{SUM} = \frac{\sin\left[\Pi_{SUM}(f)\right]}{N\sin\left[\dfrac{\Pi_{SUM}(f)}{N}\right]} \tag{A.26}$$

To simplify the error analysis, the phase angle error in (A.17) is defined according to (A.27), and the corresponding error in (A.23) is defined according to (A.28).

$$A_{DIF} = e^{i\frac{\Pi_{DIF}(f)}{N}[2(r+1/2)+N-1]} \tag{A.27}$$

$$A_{SUM} = e^{-i\frac{\Pi_{SUM}(f)}{N}[2(r+1/2)+N-1]} \tag{A.28}$$

The signal x_k in (A.29) sampled at $N = 32$ times the nominal frequency ($f_0 = 60$ Hz) with $X_{pk} = \sqrt{2}$, $f_{op} = 45$ Hz, and $\phi = 0°$ (shown in Figure A.3) is used to illustrate the magnitude and phase angle errors at off nominal frequencies. The ½ offset in (A.29) is used to match the coefficients of the centered window of the DFT. The corresponding DFT based phasor χ_k is obtained by using (A.30).

$$x_k = X_{pk} \cdot \cos\left(2\pi f_{op}(k-1/2)\Delta t + \phi\right) \tag{A.29}$$

$$\chi_k = \frac{\sqrt{2}}{N} \sum_{n=r}^{r+N-1} x_{k-n} e^{-i(n+1/2)\frac{2\pi}{N}} \tag{A.30}$$

χ_k is a phasor that rotates $\frac{2\pi}{N}$ degrees every sample. In (A.31), the contra-rotating phasor $e^{ik\frac{2\pi}{N}}$ multiplies the rotating phasor χ_k to create a stationary phasor χ_{k_S} at nominal frequency.

$$\chi_{k\_S} = \chi_k e^{ik\frac{2\pi}{N}} \tag{A.31}$$
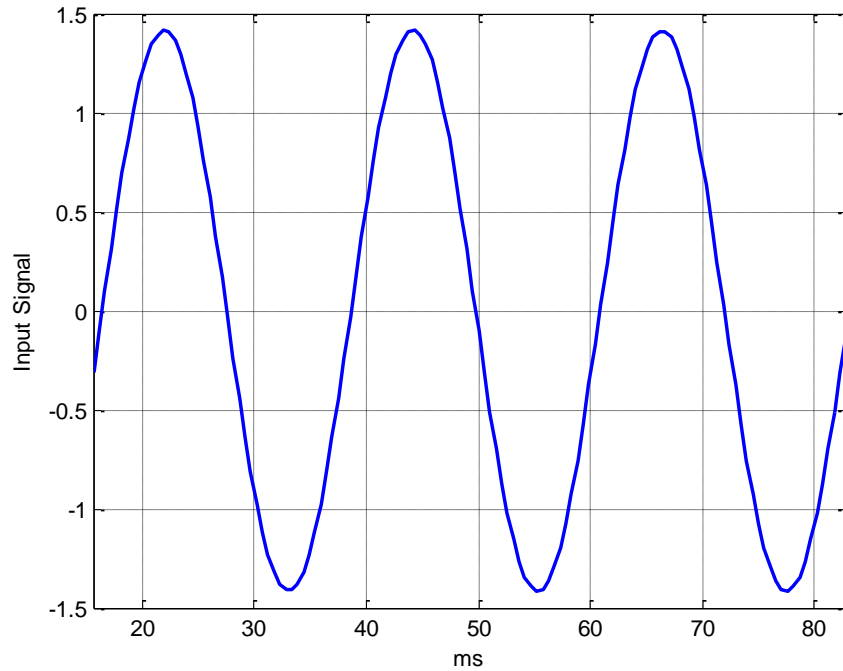
Figure A.3   Sinusoidal input signal (45 Hz).

Figure A.4 and Figure A.5 show the magnitude and phase of the stationary phasor that represents the 45 Hz input signal of Figure A.3 (*Appendices C* and *E* include the Mathcad® and MATLAB® script files that generate Figure A.4 and Figure A.5). Notice that the relative phase of the stationary phasor increases at a rate proportional to the frequency deviation from nominal frequency. Figure A.4 includes the limits based on M_{DIF} and M_{SUM} for maximum and minimum magnitude errors according to (A.32), (A.33), (A.34), and (A.35) . The signal magnitude oscillates between these limits at 90 Hz, which is twice the input frequency (45·2 Hz).

$$M\varepsilon_{L1} = \left| M_{DIF} - M_{SUM} \right| \tag{A.32}$$

$$M\varepsilon_{L2} = \left| M_{DIF} + M_{SUM} \right| \tag{A.33}$$

$$M\varepsilon_{MAX} = \max(M\varepsilon_{L1}, M\varepsilon_{L2}) \tag{A.34}$$

$$M\varepsilon_{MIN} = \min(M\varepsilon_{L1}, M\varepsilon_{L2}) \tag{A.35}$$
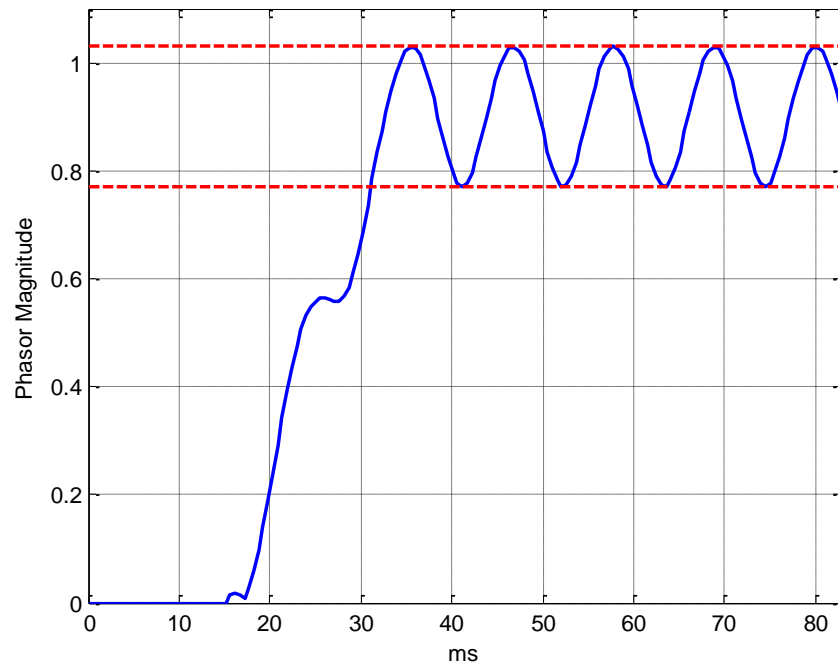
Figure A.4   Magnitude of the phasor of the 45 Hz sinusoidal signal.

Figure A.5 shows oscillations of the phase angle. In order to show the range of values of these oscillations, the stationary phasor χ_{k_s} is multiplied by a contra-rotating phasor according to (A.36), which is function of the deviation of nominal frequency: $\Delta f = f_{op} - f_0$ (see Figure A.6).

$$\chi_{k\_Sf} = \chi_{k\_s}\, e^{ik2\pi\left(\frac{f_{op}-f_0}{Nf_0}\right)} = \chi_{k\_s}\, e^{ik2\pi\left(\frac{\Delta f}{Nf_0}\right)} \tag{A.36}$$

Equation (A.37) defines the average phase angle of the oscillation, (A.38) and (A.39) define the limits of the phase angle errors. Figure A.6 shows the angle oscillation, the average phase angle, and the oscillation limits for the 45 Hz input signal.

$$A_{avg} = \angle\left(A_{DIF} M_{DIF}\right) \tag{A.37}$$

$$A\varepsilon_{L1} = \angle\left[A_{DIF} M_{DIF} + \left|A_{SUM} M_{SUM}\right| e^{i\left(A_{avg}-\frac{\pi}{2}\right)} \right] \tag{A.38}$$

$$A\varepsilon_{L2} = \angle\left[A_{DIF} M_{DIF} + \left|A_{SUM} M_{SUM}\right| e^{i\left(A_{avg}+\frac{\pi}{2}\right)} \right] \tag{A.39}$$
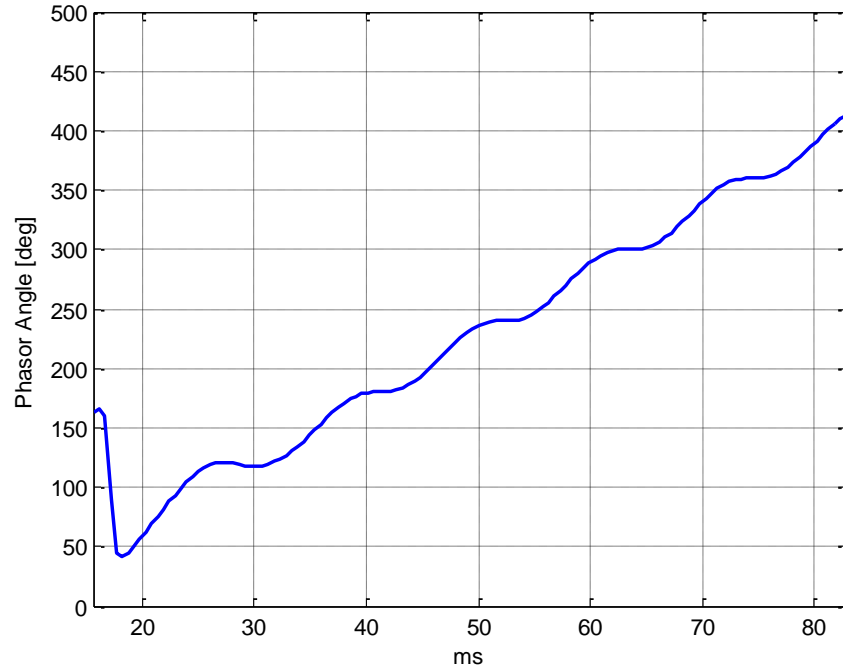
Figure A.5   Phase of the stationary phasor of the 45 Hz sinusoidal signal.
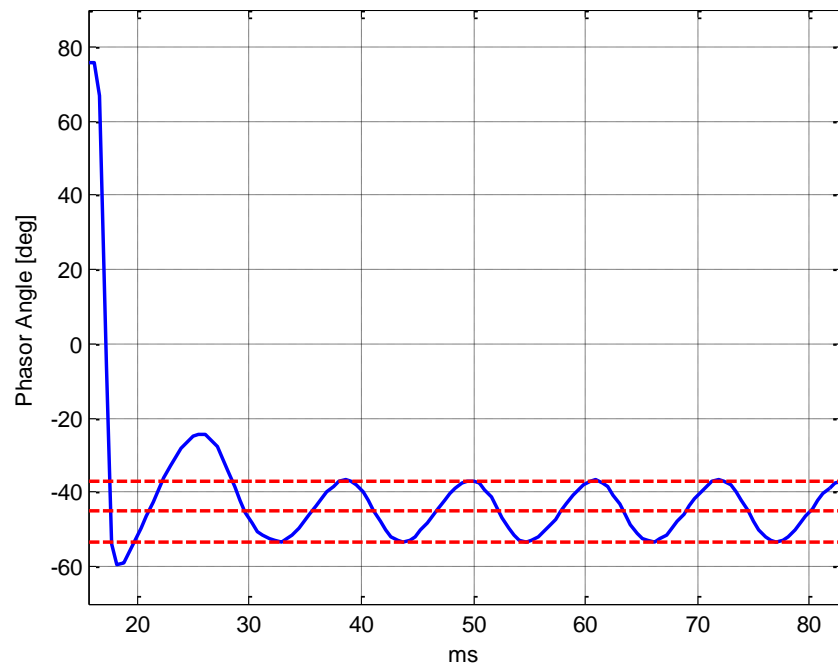
Figure A.6   Variations in phase angle of the 45 Hz sinusoidal signal.

Figure A.7 shows the comparison among the phasors of the estimated 45 Hz input signal using the DFT — ○ marks — and the calculated phasors using (A.24) — + marks. Notice that it takes 32 samples for the estimated phasor to match the calculated phasor. This number of samples correspond to the window length of the DFT used in the phasor estimation.
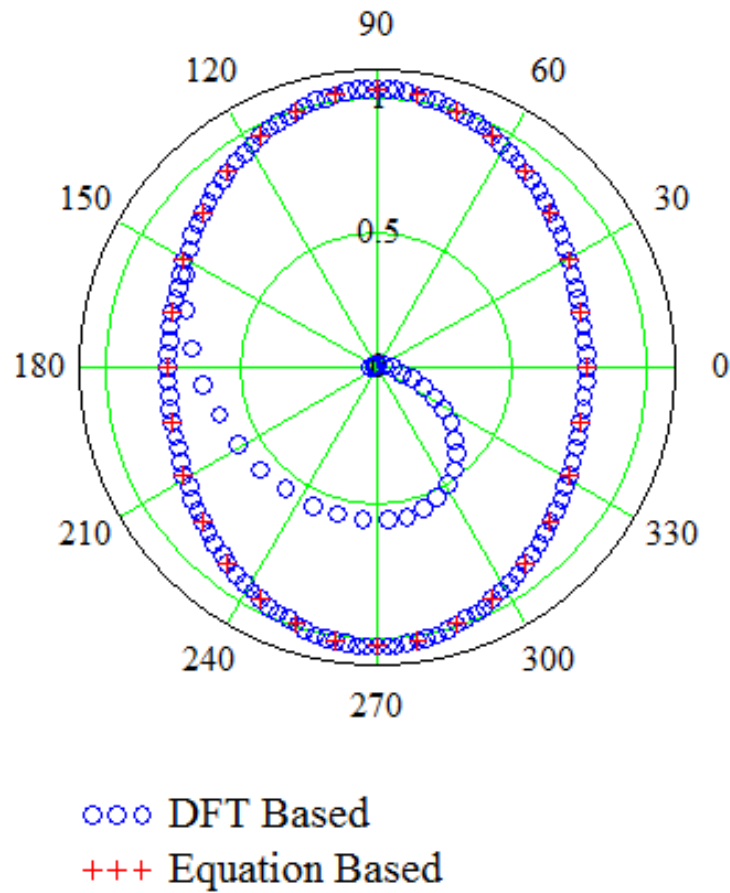
Figure A.7   The analytically calculated phasors match the DFT estimated phasors.

Appendix B Exponential Sum Formula

The sum of exponential functions can be represented in terms sine and exponential functions (B.6) as shown in the below derivation.

$$\sum_{k=0}^{N-1}\left(e^{i\theta}\right)^k = \frac{e^{iN\theta}-1}{e^{i\theta}-1} \tag{B.1}$$

$$\frac{e^{iN\theta}-1}{e^{i\theta}-1} = \frac{e^{iN\frac{\theta}{2}} \cdot e^{iN\frac{\theta}{2}} - e^{iN\frac{\theta}{2}} \cdot e^{-iN\frac{\theta}{2}}}{e^{i\frac{\theta}{2}} \cdot e^{i\frac{\theta}{2}} - e^{i\frac{\theta}{2}} \cdot e^{-i\frac{\theta}{2}}} \tag{B.2}$$

$$\frac{e^{iN\frac{\theta}{2}} \cdot e^{iN\frac{\theta}{2}} - e^{iN\frac{\theta}{2}} \cdot e^{-iN\frac{\theta}{2}}}{e^{i\frac{\theta}{2}} \cdot e^{i\frac{\theta}{2}} - e^{i\frac{\theta}{2}} \cdot e^{-i\frac{\theta}{2}}} = \frac{\left(e^{iN\frac{\theta}{2}} - e^{-iN\frac{\theta}{2}}\right)e^{iN\frac{\theta}{2}}}{\left(e^{i\frac{\theta}{2}} - e^{-i\frac{\theta}{2}}\right)e^{i\frac{\theta}{2}}} \tag{B.3}$$

$$\frac{\left(e^{iN\frac{\theta}{2}} - e^{-iN\frac{\theta}{2}}\right)e^{iN\frac{\theta}{2}}}{\left(e^{i\frac{\theta}{2}} - e^{-i\frac{\theta}{2}}\right)e^{i\frac{\theta}{2}}} = \frac{\left(e^{iN\frac{\theta}{2}} - e^{-iN\frac{\theta}{2}}\right)}{\left(e^{i\frac{\theta}{2}} - e^{-i\frac{\theta}{2}}\right)}e^{i(N-1)\frac{\theta}{2}} \tag{B.4}$$

$$\frac{\left(e^{iN\frac{\theta}{2}} - e^{-iN\frac{\theta}{2}}\right)}{\left(e^{i\frac{\theta}{2}} - e^{-i\frac{\theta}{2}}\right)}e^{i(N-1)\frac{\theta}{2}} = \frac{2i\sin\left(\dfrac{N\theta}{2}\right)}{2i\sin\left(\dfrac{\theta}{2}\right)}e^{i(N-1)\frac{\theta}{2}} \tag{B.5}$$

$$\sum_{k=0}^{N-1}(e^{i\theta})^k = \frac{2i\sin\left(\dfrac{N\theta}{2}\right)}{2i\sin\left(\dfrac{\theta}{2}\right)}e^{i(N-1)\frac{\theta}{2}} = \frac{\sin\left(\dfrac{N\theta}{2}\right)}{\sin\left(\dfrac{\theta}{2}\right)}e^{i(N-1)\frac{\theta}{2}} \tag{B.6}$$

Then (B.7) is a more generic expression where r defines the start of the summation.

$$\sum_{k=r}^{r+N-1}\left(e^{j\theta}\right)^k = e^{ir\theta}\sum_{k=0}^{N-1}\left(e^{i\theta}\right)^k = e^{ir\theta}\frac{\sin\left(\dfrac{N\theta}{2}\right)}{\sin\left(\dfrac{\theta}{2}\right)}e^{i(N-1)\frac{\theta}{2}} \tag{B.7}$$

Appendix C DFT-Based Phasor Estimation Using Mathcad®

Estimation of Phasors at Off-Nominal Frequency Using DFT

Small number to avoid division by zero

$$\varepsilon := 10^{-99}$$

Frequency difference factor
$$\Pi_{DIF}(f) := \pi \, \frac{f - f_0 + \varepsilon}{f_0}$$

Frequency sum factor
$$\Pi_{SUM}(f) := \pi \, \frac{f + f_0 + \varepsilon}{f_0}$$

Magnitude errors

$$M_{DIF}(f) := \frac{\sin\left(\Pi_{DIF}(f)\right)}{N \cdot \sin\left(\dfrac{\Pi_{DIF}(f)}{N}\right)} \qquad\qquad M_{SUM}(f) := \frac{\sin\left(\Pi_{SUM}(f)\right)}{N \cdot \sin\left(\dfrac{\Pi_{SUM}(f)}{N}\right)}$$

Phase angle errors

$$A_{DIF}(f) := e^{\, i \cdot \frac{\Pi_{DIF}(f)}{N}\left[2 \cdot \left(r + \frac{1}{2}\right) + N - 1\right]} \qquad\qquad A_{SUM}(f) := e^{\, -i \cdot \frac{\Pi_{SUM}(f)}{N} \cdot \left[2 \cdot \left(r + \frac{1}{2}\right) + N - 1\right]}$$

Frequency difference phasor component

$$\chi_{r\_DIF}(r, f, \phi) := \frac{X_{pk}}{\sqrt{2}} \cdot e^{j \cdot \phi} \cdot A_{DIF}(f) \cdot M_{DIF}(f)$$

Frequency sum phasor component

$$\chi_{r\_SUM}(r, f, \phi) := \frac{X_{pk}}{\sqrt{2}} \cdot e^{-j \cdot \phi} \cdot A_{SUM}(f) \cdot M_{SUM}(f)$$

Phasor estimation

$$\chi_r(r, f, \phi) := \chi_{r\_DIF}(r, f, \phi) + \chi_{r\_SUM}(r, f, \phi)$$

Phasor peak value $\qquad$ $X_{pk} \equiv \sqrt{2}$

Nominal frequency $\qquad$ $f_0 \equiv 60$

Samples per cycle $\qquad$ $N \equiv 32$

Phasor angles $\qquad$ $\phi_{in} \equiv \left(0, \dfrac{2\pi}{N} .. 2\cdot\pi \right)$

Signal frequency $\qquad$ $f_{op} \equiv 45$

Initial sample $\qquad$ $r \equiv 0$

Phasor Estimation
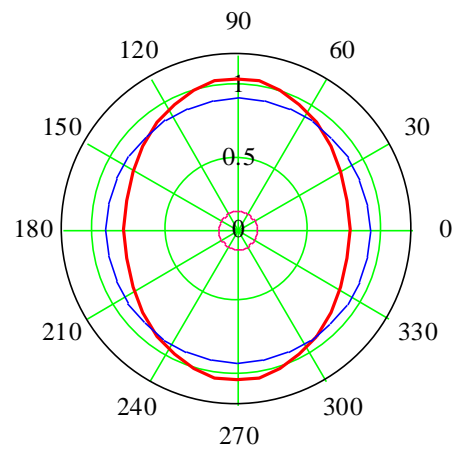
— Xr
— Xr_DIF
— Xr_SUM

Comparison between the analytical and actual signal magnitude and phase angle errors

$$f_s := N \cdot f_0$$ Sampling rate

$$\Delta t := \frac{1}{f_s}$$ Sampling interval

$$\theta := 0$$ Signal phase at t=0

$$k_i := N - 1 + r$$ Initial sample

$$k_f := N \cdot 10$$ Final sample

$$k := k_i .. k_f$$ Sample range

Input signal

$$x_k := X_{pk} \cdot \cos\left[2 \cdot \pi \cdot f_{op} \cdot \left(k - \frac{1}{2} \right) \cdot \Delta t + \theta \cdot \deg \right]$$
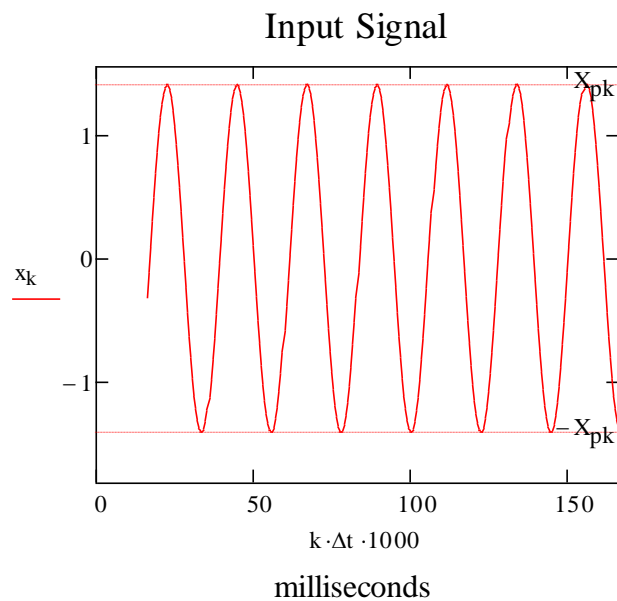
Input Signal

Input signal DFT

$$\chi_k := \frac{\sqrt{2}}{N} \cdot \sum_{n=r}^{r+N-1} \left[x_{k-n} \cdot e^{-i \cdot \left(n + \frac{1}{2} \right) \cdot \frac{2 \cdot \pi}{N}} \right]$$

Stationary phasor

$$\chi_{S_k} := \chi_k \cdot e^{\,i \cdot k \cdot \frac{2 \cdot \pi}{N}}$$

Phasor magnitude and magnitude error limits

$$M\varepsilon_{L1} := \left| M_{DIF}(f_{op}) - M_{SUM}(f_{op}) \right| \qquad M\varepsilon_{L2} := \left| M_{DIF}(f_{op}) + M_{SUM}(f_{op}) \right|$$

$$M\varepsilon_{MAX} := \max\left(M\varepsilon_{L1}, M\varepsilon_{L2} \right)$$

$$M\varepsilon_{MIN} := \min\left(M\varepsilon_{L1}, M\varepsilon_{L2} \right)$$

Phasor Magnitude
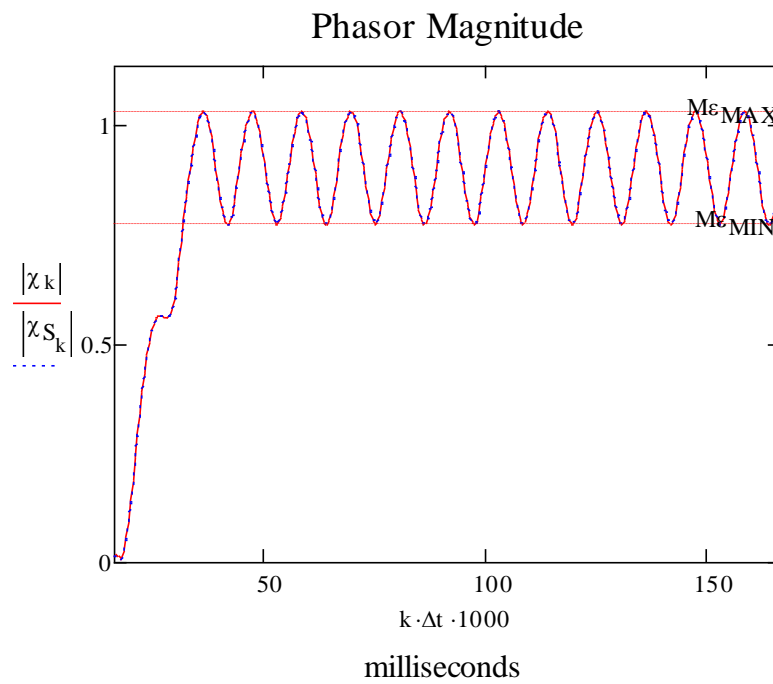
$M\varepsilon_{MAX} = 1.0297$

$M\varepsilon_{MIN} = 0.7712$

$k \cdot \Delta t \cdot 1000$

milliseconds

Stationary phasor phase angle
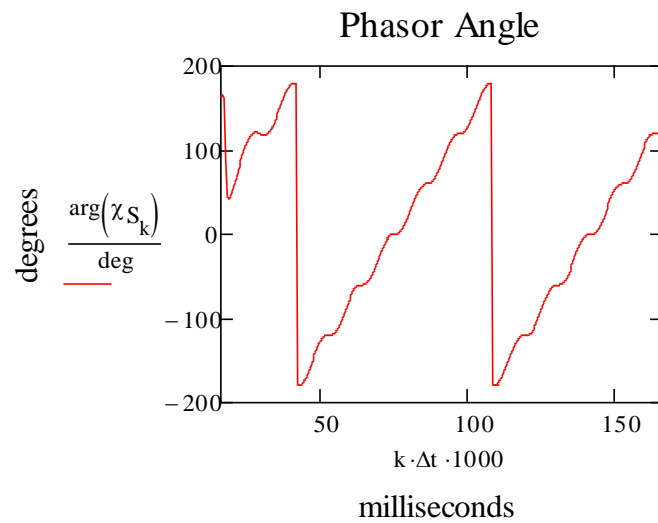
Phasor Angle

Stationary phasor angle error limits

Phasor with frequency deviation from nominal compensation

$$\chi_{Sf_k} := \chi_{S_k} \cdot e^{\,i \cdot k \cdot 2 \cdot \pi \left(f_{op} - f_0\right) \cdot \Delta t}$$

Average oscillation value

$$A_{avg}(f) := \arg\left(A_{DIF}(f) \cdot M_{DIF}(f)\right)$$

Oscillation limits

$$A\varepsilon_{L1} := \frac{\arg\left[A_{DIF}\left(f_{op}\right) \cdot M_{DIF}\left(f_{op}\right) + \left|A_{SUM}\left(f_{op}\right) \cdot M_{SUM}\left(f_{op}\right)\right| \cdot e^{\,i \cdot \left(A_{avg}\left(f_{op}\right) + \frac{\pi}{2}\right)}\right]}{deg}$$

$$A\varepsilon_{L2} := \frac{\arg\left[A_{DIF}\left(f_{op}\right) \cdot M_{DIF}\left(f_{op}\right) + \left|A_{SUM}\left(f_{op}\right) \cdot M_{SUM}\left(f_{op}\right)\right| \cdot e^{\,i \cdot \left(A_{avg}\left(f_{op}\right) - \frac{\pi}{2}\right)}\right]}{deg}$$

$$A\varepsilon_{MAX} := \max\left(A\varepsilon_{L1}, A\varepsilon_{L2}\right)$$

$$A\varepsilon_{MIN} := \min\left(A\varepsilon_{L1}, A\varepsilon_{L2}\right)$$

Phase Angle Error

$$A\varepsilon_{MAX} = -36.8311$$

$$A\varepsilon_{MIN} = -53.1689$$
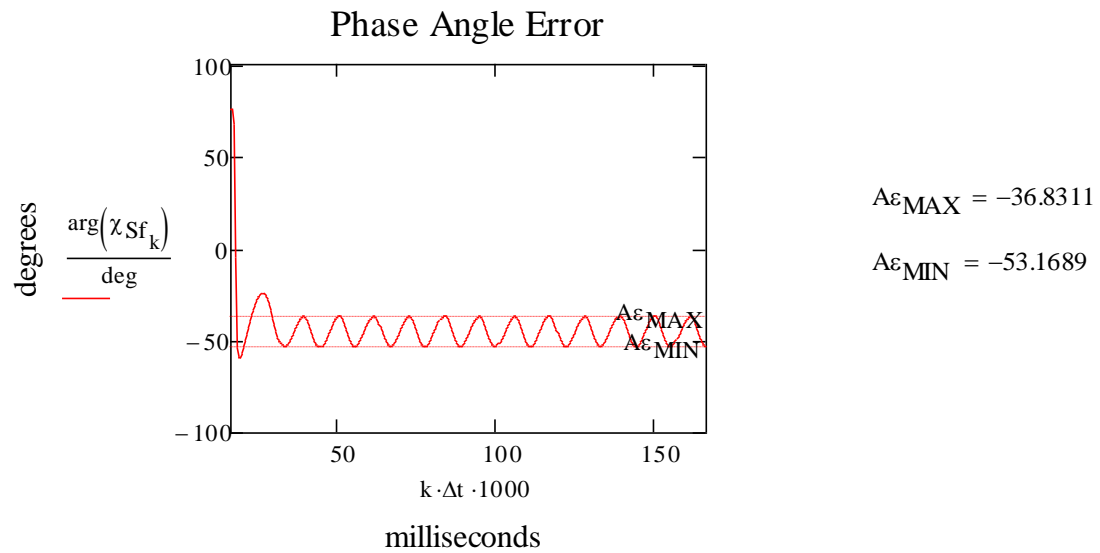
Phasor comparison between analytical (equation based) and actual phasor of the input signal

Input Signal Phasors

○ ○ ○ DFT Based
+ + + Equation Based
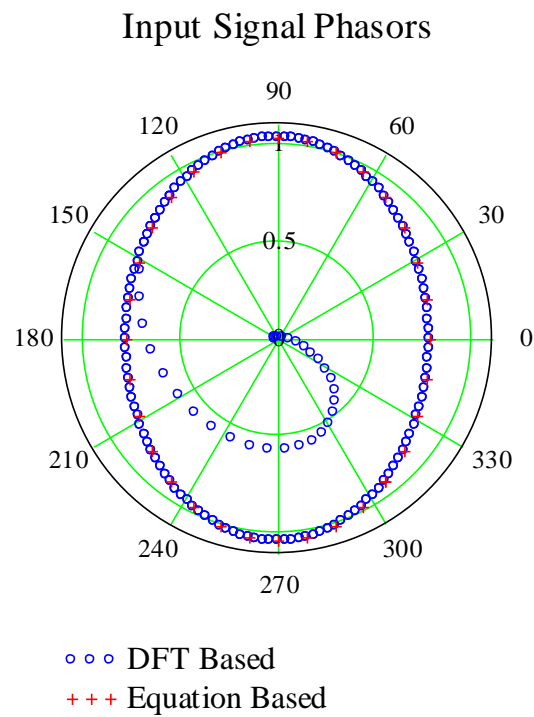
Appendix D DFT-Based Phasor Estimation at Different Frequencies Using Matlab®

```matlab
%Phasor
clear all;close all;
% Input signal frequencies: 30, 45, 60, 75 and 90 Hz
N=32;
r=0;
color='r-';
f=30;
phasor_plot(N,f,r,color)
hold on
color='b-';
f=45;
phasor_plot(N,f,r,color)
color='k-';
f=60;
phasor_plot(N,f,r,color)
color='g-';
f=75;
phasor_plot(N,f,r,color)
color='m-';
f=90;
phasor_plot(N,f,r,color)
hold off

function phasor_plot(N,f,r,color)
f0=60;%Nominal frequency (Hz)
Xpk=sqrt(2);%Input signal peak value
phi=0:2*pi/N:2*pi;

%Phasor Estimation
PIsum=pi*(f+f0+eps)/f0;
PIdif=pi*(f-f0+eps)/f0;
Mdif=sin(PIdif)/(N*sin(PIdif/N));
Msum=sin(PIsum)/(N*sin(PIsum/N));

Adif=exp(1i*PIdif*(2*(r+1/2)+N-1)/N);
Asum=exp(-1i*PIsum*(2*(r+1/2)+N-1)/N);

Xrdif=(Xpk/sqrt(2))*exp(1i*phi)*...
      Adif*Mdif;
Xrsum=(Xpk/sqrt(2))*exp(-1i*phi)*...
      Asum*Msum;
Xr=Xrdif+Xrsum;

polar(angle(Xr),abs(Xr),color)
title('N = 32,  r=0, 0 \leq \phi \leq 360\circ','FontSize',12);
```

Appendix E DFT-Based Magnitude and Angle Phasor Estimation Using Matlab®

```matlab
%% General Data
clear all;close all;
deg=180/pi;
Xpk=sqrt(2);%Input signal peak value
N=32;%Samples per cycle
phi=0:2*pi/N:2*pi;%Input signal phase
f=45;%Input signal frequency (Hz)
f0=60;%Nominal frequency (Hz)
fs=N*f0;%Sampling frquency
dt=1/fs;%Sampling interval
r=0;%Initial sample
%% Phasor Estimation
PIsum=pi*(f+f0+eps)/f0;%Frequency sum factor
PIdif=pi*(f-f0+eps)/f0;%Frequency difference factor
%Magnitude errors
Mdif=sin(PIdif)/(N*sin(PIdif/N));
Msum=sin(PIsum)/(N*sin(PIsum/N));
%Phase angle errors
Adif=exp(1i*PIdif*(2*(r+1/2)+N-1)/N);
Asum=exp(-1i*PIsum*(2*(r+1/2)+N-1)/N);
%Phasor's amplitude and phase
X=(Xpk/sqrt(2))*exp(1i*phi);
%Frequency difference phasor component
Xrdif=X*Adif*Mdif;
%Frequency sum phasor component
Xrsum=conj(X)*Asum*Msum;
%Phasor estimation
Xr=Xrdif+Xrsum;

Xrang_shift=angle(Xr.*exp(-1i*phi));

%Phasor magnitude and magnitude error limits
MeL1=abs(Mdif-Msum);
MeL2=abs(Mdif+Msum);

MeMAX=max([MeL1 MeL2]);
MeMIN=min([MeL1 MeL2]);
%Input signal additional data
ki=N-1+r;                                %Initial sample
kf=N*5;                                  %Final sample
k=ki:kf;                                 %Sample range
theta=0;                                 %Signal phase at t=0
x(k)=Xpk*cos(2*pi*f*(k-1/2)/fs+theta);   %Input signal
t=(0:(length(x)-1))/fs;                  %Time vector

%Input signal DFT
```

```matlab
b=(sqrt(2)/N)*exp(-1i*(0.5:[N-1+0.5])*2*pi/N);
b=circshift(b',-r)';
Xdft=filter(b,1,x);
for k=k(1):k(length(k))
%Stationary phasor
Xr_S(k)=Xdft(k)*exp(1i*k*2*pi/N);
%Frequency deviation from nominal compensation
Xr_Sf(k)=Xr_S(k)*exp(1i*k*2*pi*(f-f0)/fs);
end

%Average oscillation value
A_avg=angle(Adif*Mdif);
%Oscillation limits
Ae_L1=angle(Adif*Mdif+abs(Asum*Msum)*exp(1i*(A_avg+pi/2)));
Ae_L2=angle(Adif*Mdif+abs(Asum*Msum)*exp(1i*(A_avg-pi/2)));
Aemax=max(Ae_L1,Ae_L2);
Aemin=min(Ae_L1,Ae_L2);

%% Plots
ms=1000;% Millisecond factor
figure('windowbuttondownfcn','zoom on;');
plot(t*ms,x,'b','LineWidth',2)
axis([t(1)*ms t(length(t))*ms -1.5 1.5])
ylabel('Input Signal')
xlabel('ms')
title([num2str(f),' Hz'])
axis([t(ki)*ms t(kf)*ms -1.5 1.5])
grid

figure('windowbuttondownfcn','zoom on;');
plot(t*ms,abs(Xr_S),'b')
plot(t*ms,abs(Xr_S),'b',[t(1) t(length(t))]*ms,[MeMAX MeMAX],'r--
',...
     [t(1) t(length(t))]*ms,[MeMIN MeMIN],'r--','LineWidth',2)
axis([t(1)*ms t(length(t))*ms 0 1.1])
ylabel('Phasor Magnitude')
xlabel('ms')
title([num2str(f),' Hz'])
grid

figure('windowbuttondownfcn','zoom on;');
plot(t*ms,unwrap(angle(Xr_S))*deg,'b',...
     'LineWidth',2)
ylabel('Phasor Angle [deg]')
xlabel('ms')
title([num2str(f),' Hz'])
axis([t(ki)*ms t(kf)*ms 0 500])
grid
figure('windowbuttondownfcn','zoom on;');
plot(t*ms,angle(Xr_Sf)*deg,'b',...
```

```
        [t(1) t(length(t))]*ms,[Aemax Aemax]*deg,'r--',...
        [t(1) t(length(t))]*ms,[Aemin Aemin]*deg,'r--',...
        [t(1) t(length(t))]*ms,[A_avg A_avg]*deg,'r--','LineWidth',2)
ylabel('Phasor Angle [deg]')
xlabel('ms')
title([num2str(f),' Hz'])
axis([t(ki)*ms t(kf)*ms -70 90])
grid
```

Appendix F Implementation of Out-of-Step and Power Swing Detection Algorithms

The out-of-step detection, power swing detection, and predictive out-of-step tripping algorithms – from *Chapter 5* – were implemented in a power system dynamics monitor through use of the SPU. Figure F.1 shows the required functionality of the SPU for this application. The PMCUs send system voltage and current phasors to the SPU. The SPU uses the programming tool CoDeSys [85] to implement and run user programmed logic and algorithms in real time. CoDeSys uses IEC-61131-3 programming language for programmable logic controllers (PLCs). After time alignment, the C37.118 Server of the SPU makes the synchrophasor measurements available to the CoDeSys Runtime System (RTS).
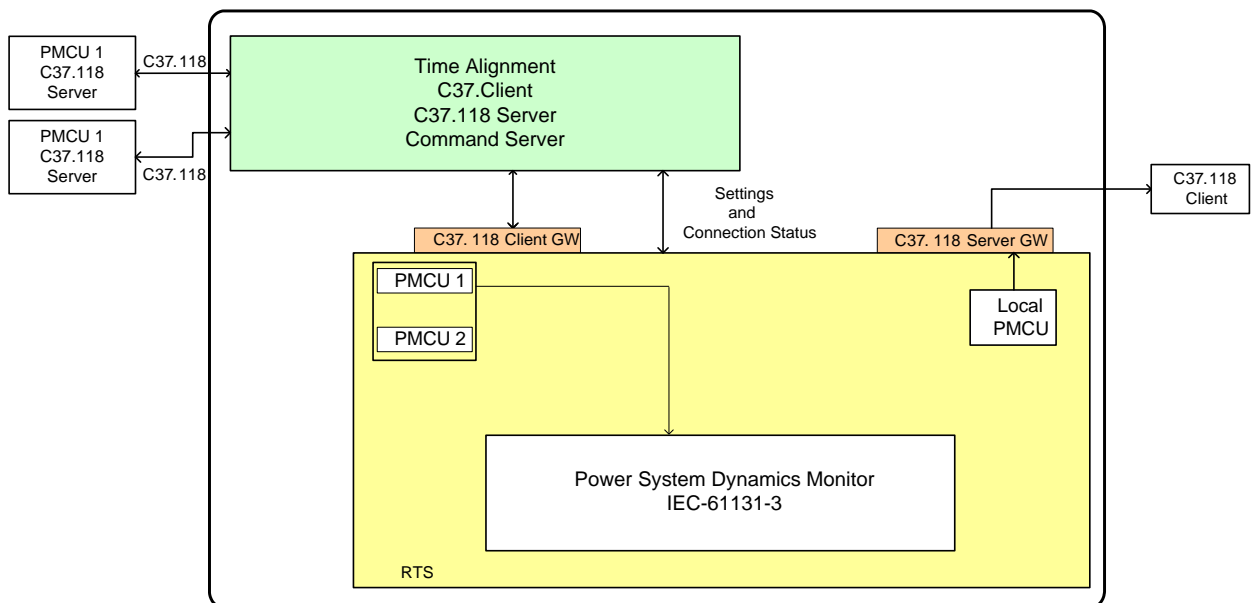
Figure F.1   SPU functionality for power dynamics monitoring.

The application example, in Figure F.2, corresponds to the power system dynamics monitor shown in Figure F.1. This example includes the following blocks:

- PMCU01. PMCU at the generator terminals with IDCODE=1. The IDCODE identifies the unit in the wide-area system.

- PMCU02. PMCU at the generator terminals with IDCODE=2.

- Diff. Angle difference calculation.

- Slip_Calc. Slip frequency calculation.

- Acc_Calc. Acceleration calculation.

- Power_Swing_Detector.

- Out_of_Step_Trip.

- Out_of_Step_Detector.

- Heart Beat.

- Trip.
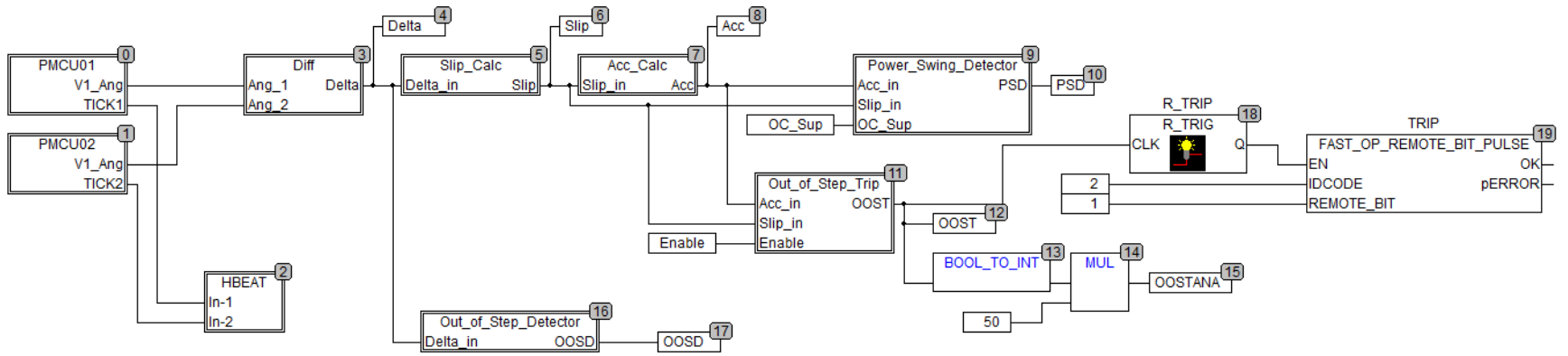
Figure F.2   SPU power system dynamics monitor.

F.1 PMCU 1 and PMCU 2 Assignment and V1 and I1 Phasor Extraction

The PMCU01 and PMCU02 blocks include the PMCU_IN and the V1_I1 blocks. The PMCU_IN block creates an instance of the PMCU associated with the IDCODE setting. In Figure F.3, the PMCU_IN block associates the PMCU_IN instance to PMCU 1; which has IDCODE=1. The TICK1 output indicates that a message has been received and PMCU 1 is working OK. The continuous function chart shown in Figure F.3 also includes the V1_I1 function block that outputs the positive-sequence voltage and current phasor magnitudes and angles.
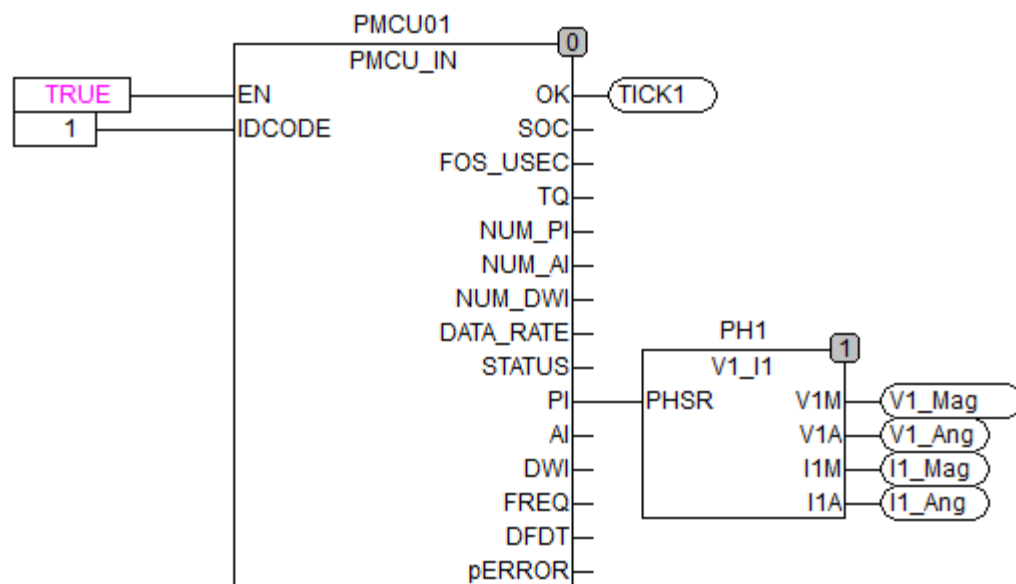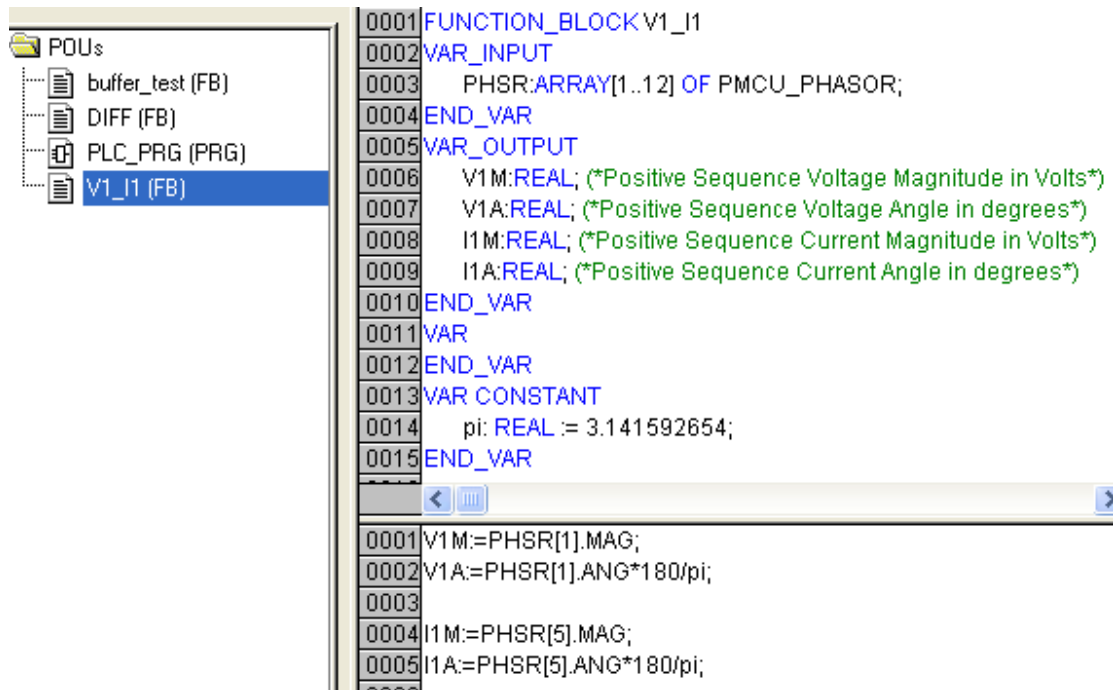
Figure F.3   PMCU assignment and positive-sequence voltage and current extraction.

F.1.1 V1_I1 Function Block

Figure F.4 shows the structured text of the V1_I1 function block. This block extracts the positive-sequence voltage and current phasors from the PMCU synchrophasor message and routes them to the output to simplify applications that use positive-sequence phasor information.


```
0001 FUNCTION_BLOCK V1_I1
0002 VAR_INPUT
0003     PHSR:ARRAY[1..12] OF PMCU_PHASOR;
0004 END_VAR
0005 VAR_OUTPUT
0006     V1M:REAL; (*Positive Sequence Voltage Magnitude in Volts*)
0007     V1A:REAL; (*Positive Sequence Voltage Angle in degrees*)
0008     I1M:REAL; (*Positive Sequence Current Magnitude in Volts*)
0009     I1A:REAL; (*Positive Sequence Current Angle in degrees*)
0010 END_VAR
0011 VAR
0012 END_VAR
0013 VAR CONSTANT
0014     pi: REAL := 3.141592654;
0015 END_VAR
```

```
0001 V1M:=PHSR[1].MAG;
0002 V1A:=PHSR[1].ANG*180/pi;
0003
0004 I1M:=PHSR[5].MAG;
0005 I1A:=PHSR[5].ANG*180/pi;
```

Figure F.4   Structured text of the V1_I1 function block. This block extracts the positive-sequence voltage and current phasors from the PMCU synchrophasor message.

F.2 Angle Difference Calculation Function Block

The angle difference calculation function block, in Figure F.5, calculates the angle difference between two phasors. The engineer can program the angle difference through use of the phase angle information from the V1_I1 function block. The output of the angle difference calculation function block is the instantaneous value of the phase angle difference between the two phasors.

Figure F.5   Angle difference calculation function block.

F.3 Slip Frequency Calculation

The slip frequency calculation algorithm, in Figure F.6, receives the angle difference information and calculates the difference between the present value and the value of 1/60th of a second ago for a message rate of 60 Hz. It uses the buffer test function block to age the angle difference value by one processing interval.

Figure F.6   Slip frequency calculation algorithm.

F.4   Acceleration Calculation

The acceleration calculation algorithm, in Figure F.7, receives the slip frequency information and calculates the difference between the present value and the value of 1/60th of a second ago. It uses the buffer test function block to age the slip frequency value by one processing interval.
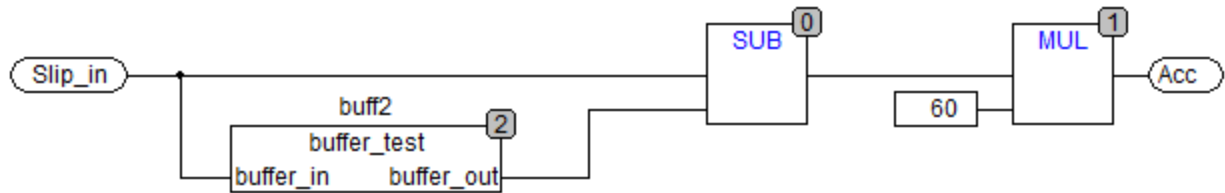
Figure F.7   Acceleration calculation algorithm.

F.5   Power Swing Detector

The power swing detector algorithm, in Figure F.8, receives slip frequency and acceleration information to identify power swings when they start to occur. When this happens, this logic asserts the *PSD* bit to alarm the power system operator of the undesirable operating condition.
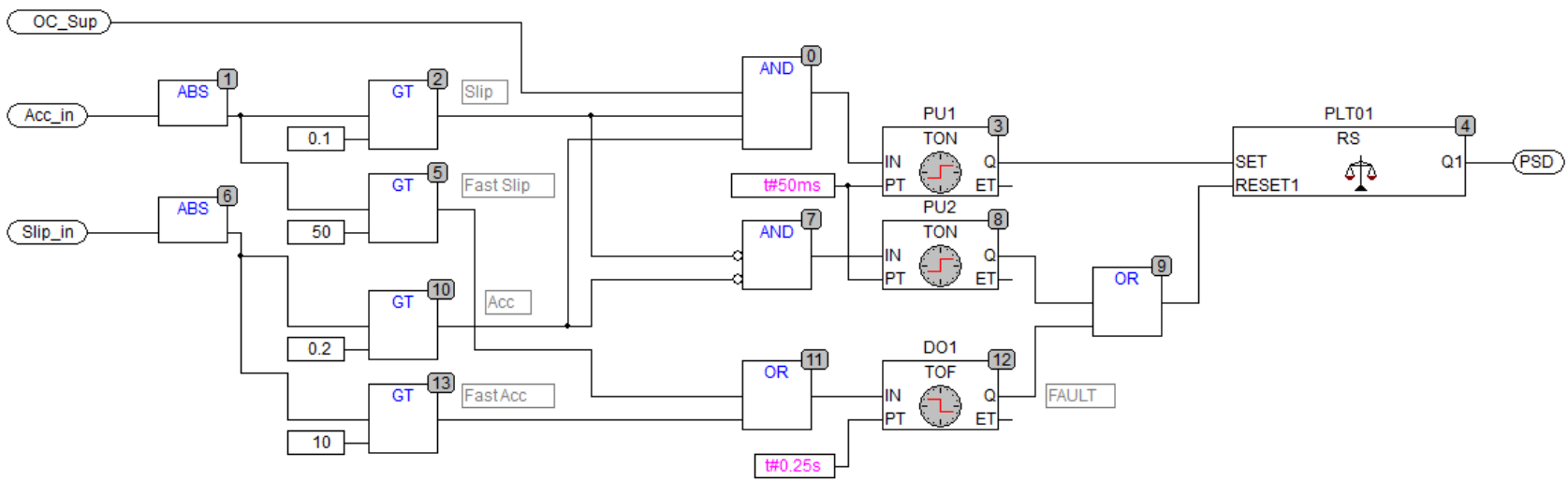
Figure F.8   Power swing detector algorithm.

F.6   Out-of-Step Trip

The out-of-step trip algorithm, in Figure F.9, receives slip frequency and acceleration information to predict unstable operating conditions. The logic asserts the *OOST* output to take a remedial action to minimize system disturbance.
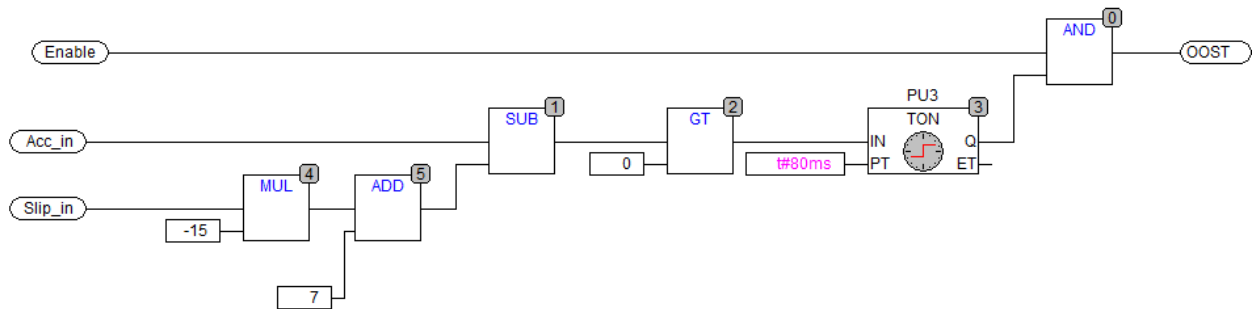
Figure F.9   Out-of-step trip algorithm predicts unstable operating conditions.

F.7   Out-of-Step Detector

The out-of-step detector logic, in Figure F.10, receives angle difference information to identify when the out-of-step condition happens. The output *OOSD* can be used for monitoring or for tripping to minimize equipment damage.
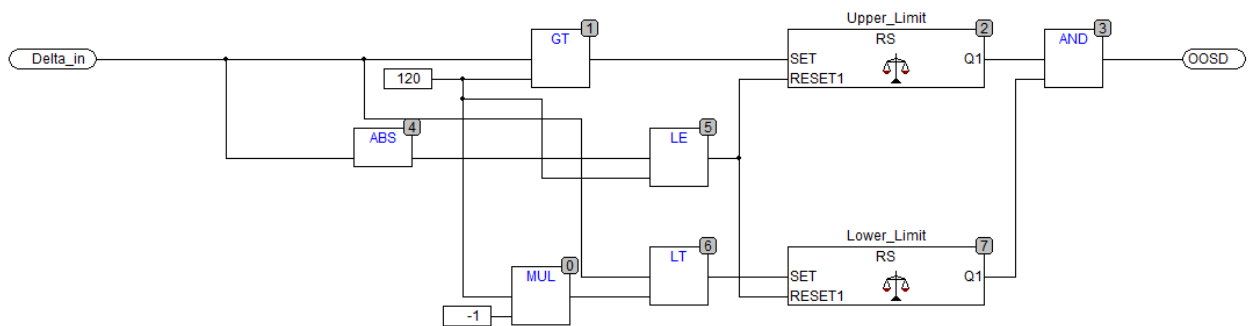
Figure F.10   Out-of-step detector logic.

F.8 Heart Beat

The heart beat logic shown in Figure F.11 acts as a watch dog circuit that monitors the health of the scheme. Every time any of the PMCUs sends a message indicating healthy operating condition, the logic continues to run. The counter asserts the test output after 9999 messages have been received.
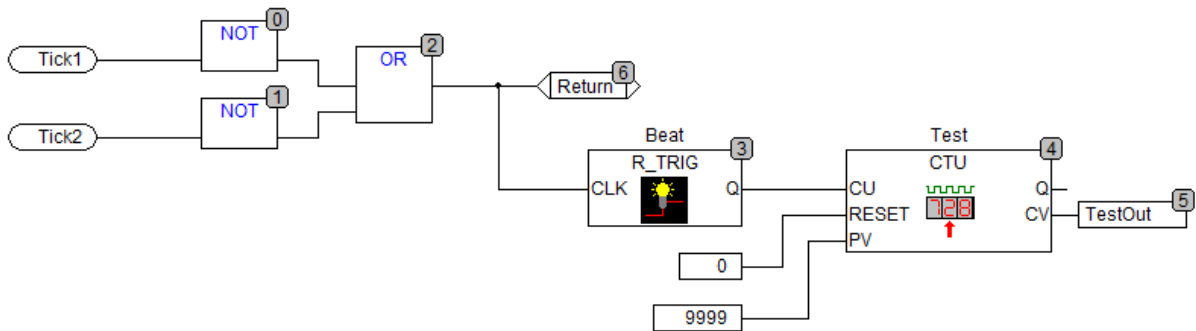
Figure F.11 Heart beat logic monitor the health of the scheme.

F.9 One Message Delay Function Block

The buffer test function block ages the incoming real value by one message delay. Figure F.12 shows the structured text for the block. This block is used to calculate the angle difference, slip, and acceleration.
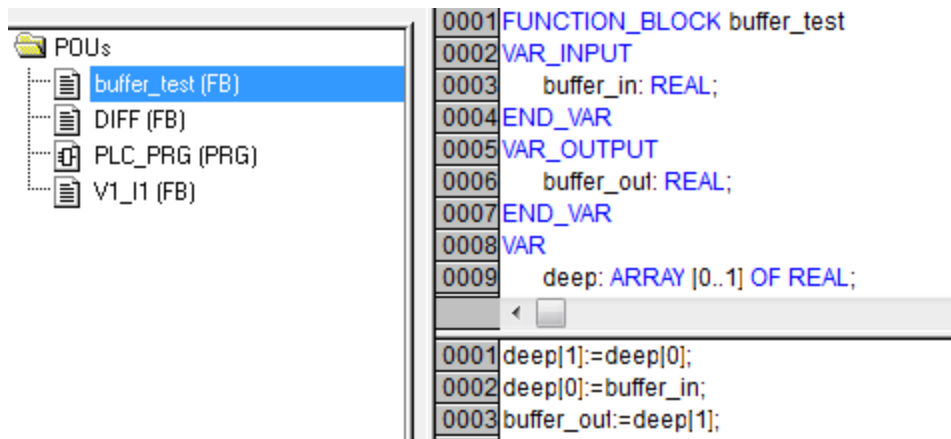
Figure F.12 One message delay function block.

F.10 Conclusion

This appendix has demonstrated use of the synchrophasor processing unit to allow the engineer to program elaborated logic and algorithms for real-time applications using industry standard programming language. This capability makes it ideal for implementing real-time wide-area monitoring and protection schemes that require rapid response such as power system dynamics monitoring.

Appendix G Prony Modal Analysis

MA is performed using the well-known Prony analysis method [66, 86, 87]. Prony analysis fits a linear model to a measured signal *y(t)* . Where *y(t)* is the output signal of a linear dynamic system. For example, bus voltage magnitude. The model is represented with the poles and residues of the corresponding transfer function. The modes of the output signal can be obtained using Prony analysis. The modes of the signal correspond to the modes of the linear system that generated the signal.

G.1   Linear Power System Model

As described earlier, a power system model linearized around its operating point is used for small signal stability analysis. The state-space representation of the linearized system has the following form:

$$\Delta \dot{x} = A \cdot \Delta x + B \cdot \Delta u \qquad \text{(G.1)}$$

$$\Delta y = C \cdot \Delta x + D \cdot \Delta u \qquad \text{(G.2)}$$

where:

Δx	is the state vector,
Δy	is the output vector (single output),
Δu	is the input vector (single input),
A	is the state matrix,
B	is the input matrix,
C	is the output matrix,
D	is the feed-forward matrix (it is zero in our application).

The corresponding transfer function is:

$$G(s) = \frac{\Delta y(s)}{\Delta u(s)} = \sum_{i=1}^{n} \frac{R_i}{s - \lambda_i} \qquad \text{(G.3)}$$

where:

$$R_i = C \cdot \Gamma_i \cdot \Pi_i \cdot B . \qquad \text{(G.4)}$$

Γ is the right eigenvector,

Π is the left eigenvector,

λ is the corresponding eigenvalue.

The system time response is:

$$y(t) = \sum_{i=1}^{n} R_i \cdot e^{\lambda_i \cdot t} \qquad \text{(G.5)}$$

G.2   Prony Analysis Method

The discrete representation of (G.5) for a signal sampled at Δt time intervals is [66]:

$$y(k) = \sum_{i=1}^{n} R_i \cdot z_i^k \qquad \text{(G.6)}$$

where:

$$z_i = e^{\lambda_i \cdot \Delta t} . \qquad \text{(G.7)}$$

Equation (G.6) is rewritten for an observation window of N samples as follows:

$$\begin{bmatrix} y(0) \\ y(1) \\ \vdots \\ y(N-1) \end{bmatrix} = \begin{bmatrix} z_1^0 & z_2^0 & \cdots & z_n^0 \\ z_1^1 & z_2^1 & \cdots & z_n^1 \\ \vdots & \vdots & \vdots & \vdots \\ z_1^{N-1} & z_2^{N-1} & \cdots & z_n^{N-1} \end{bmatrix} \begin{bmatrix} R_1 \\ R_2 \\ \vdots \\ R_n \end{bmatrix} \qquad \text{(G.8)}$$

The system eigenvalues, λ_i, can be found from z_i, z_i are the necessary roots of an nth order polynomial with q_i coefficients that satisfy (G.9):

$$z^n - \left(q_1 \cdot z^{n-1} + q_2 \cdot z^{n-2} + \cdots + q_n \cdot z^0 \right) = 0 \tag{G.9}$$

The Prony method uses the measured samples and arranges them according (G.10) to obtain the q_i vector [66]. This model constitutes the linear predictor model (LPM) that fits the measured signal.

$$\begin{bmatrix} y(n-1) & y(n-2) & \cdots & y(0) \\ y(n-0) & y(n-1) & \cdots & y(1) \\ \cdots & \cdots & \cdots & \cdots \\ y(N-2) & y(N-3) & \cdots & y(N-n-1) \end{bmatrix} \begin{bmatrix} q_1 \\ q_2 \\ \vdots \\ q_n \end{bmatrix} = \begin{bmatrix} y(n+0) \\ y(n+1) \\ \vdots \\ y(N-1) \end{bmatrix} \tag{G.10}$$

G.2.1   Eigenvalues

Given the roots (z_i) of the polynomial equation, the ith eigenvalue for each mode is calculated as follows:

$$\lambda_i = \log(Z_i) \cdot Message\_Rate \tag{G.11}$$

G.2.2   Mode Frequency

The mode frequency is calculated as follows:

$$f_{mode\_i} = \frac{imag(\lambda_i)}{2\pi} \tag{G.12}$$

G.2.3   Mode Damping

The mode damping is calculated as follows:

$$Damp_i = real(\lambda_i) \tag{G.13}$$

G.2.4 Mode Damping Ratio

The mode damping ratio is calculated as follows:

$$DampRatio_i = -\frac{real(\lambda_i)}{abs(\lambda_i)}$$

(G.14)

G.2.5 Mode Amplitude

Given the ith residue value calculated from Prony analysis, the amplitude of the ith mode is the absolute value of the ith residue:

$$Amp_i = abs(Residue_i)$$

(G.15)

G.2.6 Mode Phase

The phase angle of the ith mode is calculated as follows:

$$phase_i = atan\left[\frac{imag(Residue_i)}{real(Residue_i)}\right] \cdot \frac{180}{\pi}$$

(G.16)

G.2.7 Signal-to-Noise Ratio

Additionally, the estimated signal is compared against the original signal. To quantify the quality of the fit, the signal-to-noise ratio (*SNR*) is calculated in dBs, as follows:

$$SNR = 10 \cdot \log\left(\frac{\|y(n)\|}{\|\hat{y}(n) - y(n)\|}\right)$$

(G.17)

where:

$y[n]$ is the original signal,

$\hat{y}[n]$ is the estimated signal.

G.2.8   Prony Solution Steps

The Prony solution steps to fit the measured signal are summarized as follows:

1. Construct the LPM that fits the measured signal according to (G.10) and find the q_i vector.

2. Find the roots using (G.9) of the characteristic polynomial associated with the LPM in Step 1 to obtain z_i.

3. Determine eigenvalues, damping, and oscillation frequency for each mode.

4. Using the roots obtained in Step 2 calculate R_i from (G.8) and determine amplitude and phase for each mode.

The flow diagram in Figure G.1 shows the MA calculation process.
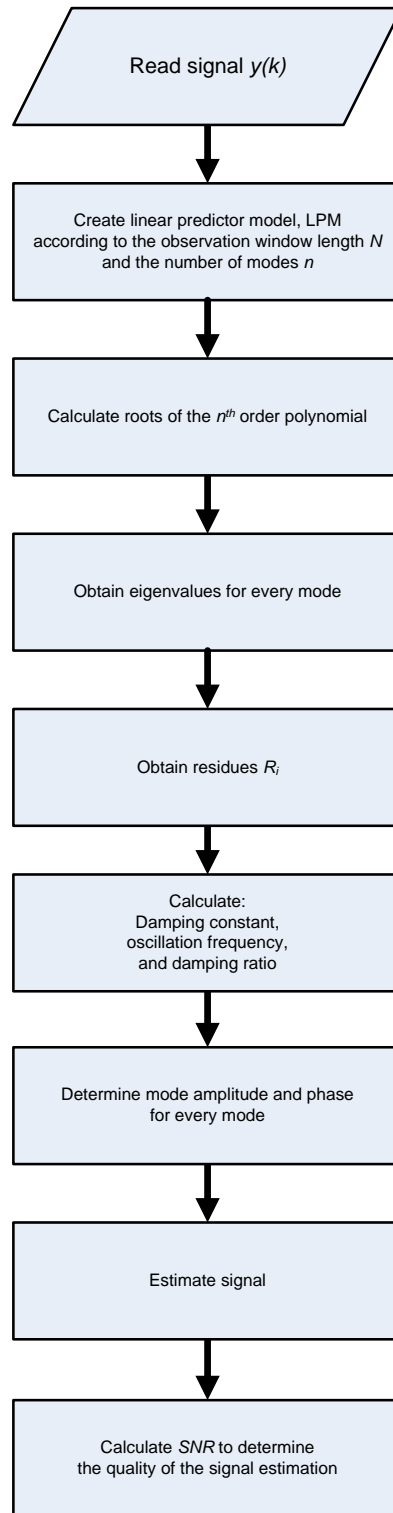
Figure G.1   Modal analysis and signal estimation using the Prony method.

Prony modal analysis Matlab® file for signal estimation:

```matlab
%%%%%%%%%%%%%%%%%%%%%%%%%%%%%%%%%%%%%%%%
load deltacase1
t=delta2(1,:);
signal=delta2(2,:); % 960 Hz
%%%%%Decimation by 16%%%%%%
t=t(1:16:length(t));
signal=signal(1:16:length(signal));
dt=1/60;
%%%%%%%%%%%%%%%%%%%%%%%%%%%%%%%
N=length(signal);%Data window
n= 2;%Number of modes
%%STEP1%%%%Create Linear Predictor Model
for col=1:n
     LPMM(:,col)=signal(n+1-col:N-col);
end
LPMV=signal(n+1:length(signal))';
%%%%%%Obtain the qi vector
q=pinv(LPMM)*LPMV;
%%STEP2%%%%Calculate the roots of the nth order polynomial
z=roots([1,-q']);
%%STEP3%%%%Obtain eigenvalues
lamda=log(z)/dt;%Eigenvalues
damping=real(lamda);%Damping
fosc=imag(lamda)/2/pi;%Oscillation Frequency
     dampratio=-real(lamda)./abs(lamda);%Damping Ratio
%%STEP4%%%%%%%Obtain Residues Ri
for row=1:N
    Z(row,:)=(z.').^(row-1);
end
R=pinv(Z)*signal';
outputamp=abs(R);%Amplitude
outputpha=angle(R)*180/pi;%Phase

%%%%%%%%%%%%%%%%%%%%%%%%%%%%%%%%%%%%%%%%%%
```

Prony modal analysis Matlab® file for mode identification:

```matlab
%%%%%%%%%%%%%%%%%%%%%%%%%%%%%%%%%%%%%%%%%%%%%%%%%%
%Field event
InputFile='Inter-Area Power Oscillation';
[Oscnum,Osctxt,Oscraw] = xlsread('Oscdata.xlsx');
PWR_Osc=Oscnum([4:length(Oscnum)],2)/1000;%Power in MW
%%%%%%%%%%%%%%%%%%%%%%%%%%%%%%%%%%%%%%%%%%%%%
Window=20;%Observation window in seconds
Rate=30;%Message rate
dt=1/Rate;
n=5;%Number of modes
last_sample=5377;
TotalData=PWR_Osc';
t=(0:(length(TotalData)-1))*dt;
%Initialize variables
time=[];
freq=[];
ampl=[];
dampr=[];
Start=1;
k=1;
tini=t(Window*Rate+1);
for WindowStart=Start:Window*Rate/2:Window*Rate*8
WindowEnd=WindowStart+Window*Rate-1;
WindowData=TotalData([WindowStart:WindowEnd]);
WindowTime=t([WindowStart:WindowEnd]);
signal=WindowData;
N=length(signal);%Data window
%%Prony  Modal Analysis
%%STEP1%%%%%Create Linear Predictor Model
for col=1:n
     LPMM(:,col)=signal(n+1-col:N-col);
end
LPMV=signal(n+1:length(signal))';
%%%%%%%Obtain the qi vector
q=pinv(LPMM)*LPMV;
%%STEP2%%%%%Calculate the roots of the nth order polynomial
z=roots([1,-q']);
%%STEP3%%%%%Obtain eigenvalues
lamda=log(z)/dt;%Eigenvalues
Frequency=imag(lamda)/2/pi;%Oscillation Frequency
DampingRatio=-real(lamda)./abs(lamda);%Damping Ratio
%%STEP4%%%%%%%%Obtain Residues Ri
for row=1:N
    Z(row,:)=(z.').^(row-1);
end
R=pinv(Z)*signal';
Amplitude=abs(R);%Amplitude
```

```matlab
%%%Sorting modes
[Frequency,IX]=sort(Frequency,'descend');
Amplitude=Amplitude(IX);
DampingRatio=DampingRatio(IX);
time=[time ones(n,1)*WindowTime(1)];
ampl=[ampl Amplitude];
freq=[freq Frequency];
dampr=[dampr DampingRatio];
k=k+1;
end
%%%%%%%%%%%%%%%%%%%%%%%%%%%%%%%%%%%%%%%%%%%%%%%%%%%%%%
```